

New Methods for Separating and Measuring Anisotropies in Solid
State NMR

DISSERTATION

Presented in Partial Fulfillment of the Requirements for the Degree Doctor of
Philosophy in the Graduate School of the Ohio State University

By

Krishna Kishor Dey, BS, MS
Graduate Program in Chemistry

The Ohio State University

2010

Dissertation Committee:

Professor Philip J. Grandinetti, Advisor

Professor Christopher P. Jaroniec

Professor Heather C. Allen

© Copyright by
Krishna Kishor Dey
2010

ABSTRACT

The cubic mesophase formed by monoacylglycerols and water is an important medium for the *in meso* crystallogenesis of membrane proteins. To investigate molecular level lipid and additive interactions within the cubic phase, a method was developed for improving the resolution of ^1H NMR spectra when using a conventional solution state NMR probe. Using this approach we obtained well-resolved J -coupling multiplets in the one-dimensional NMR spectrum of the cubic-Ia3d phase prepared with hydrated monoolein. The Carr-Purcell-Meiboom-Gill (CPMG) experiment has gained popularity in solid-state NMR as a method for enhancing sensitivity for anisotropically broadened spectra of both spin 1/2 and half integer quadrupolar nuclei. Larger sensitivity enhancements are observed as the delay between the π pulses is shortened. However, as the duration between the π pulses is shortened, the echoes become truncated and information about the nuclear spin interactions is lost. We explored the relationship between enhanced sensitivity and loss of information as a function of the product $\Omega 2\tau$, where Ω is the span of the anisotropic lineshape and 2τ is the π pulse spacing and additionally TOP data processing approach is presented. The anisotropic components of chemical shift contain information on the local structure around a particular nuclei of interest that is typically averaged away during magic angle spinning (MAS). While information of the full tensor can be obtained through acquisition of a static powder pattern or analysis of characteristic

spinning sideband patterns during MAS, each of these one dimensional spectra are complex when multiple chemical sites are present. To better determine the relative contributions from multiple chemical sites it is, therefore, advantageous to utilize 2D techniques such as Magic Angle Flipping (MAF), Magic Angle Hopping (MAH), Magic Angle Turning (MAT), or 2D Phase Adjusted Spinning Sideband. However, each of these techniques suffers from low sensitivity making applications to samples with low natural abundance, such as ^{29}Si (4.6 %), limited. Here, we couple 2D PASS with CPMG acquisition for added sensitivity enhancement. It is shown that echoes following odd π pulses satisfy the conditions described by Dixon (1982) while echoes following the even π pulses do not and in this manner a significant sensitivity gain is observed. The analysis of compounds with paramagnetic atoms incorporated in the structure is a growing field in solid state nuclear magnetic resonance. In typical ^2H NMR studies of diamagnetic materials, analysis of the observed first order quadrupolar powder pattern or Pake pattern is able to provide insight into molecular structure and dynamics. However, for paramagnetic materials the magnitude of the paramagnetic/chemical shift anisotropy becomes significant. In this study, we present a shifted Hahn echo sequence to separate components of the chemical shift and quadrupolar interactions, for nuclei where $I = 1$. A two times sensitivity is observed in shifted Hahn echo sequence compared to shifted solid echo sequence presented by Antonijevic et al. [1]. A formalism is also discussed to visualize how echoes will be refocused during a NMR experiment.

This thesis is dedicated to my parents, Basudev Dey and Minoty Dey

ACKNOWLEDGMENTS

I would like to give my special thanks to my advisor Prof. Philip J. Grandinetti, who is not only my thesis advisor, but also the mentor of my life. I enjoyed my Ph.D period very much in his lab. I would like to give my special thanks to Mike Davis. He is a great friend and a great co-worker. I would like to thank Kevin, and Derrick. I would like to thank all past group members, Prasad, Jason, Sam, and Nicole.

VITA

1980	Born - Calcutta, WB, India
2001	B.S Burdwan University, West Bengal, India
2004	M.S Indian Institute of Science, Bangalore
2004-Present	Graduate Teaching and Research Associate, The Ohio State University, Columbus, Ohio

PUBLICATIONS

1. Krishna K Dey, Rangeet Bhattacharrya, Anil Kumar Use of Spatial Encoding in NMR Photography *Journal of Magnetic resonance*, **171**, 359-363 (2004)
2. Krishna K Dey, S. Prasad, J. T. Ash, M. Deshamps, and P. J. Grandinetti “Spectral Editing in Solid-State MAS NMR of Quadrupolar Nuclei using Selective Satellite Inversion”, *Journal of Magnetic Resonance*, **185**, 326-330 (2007)
3. E. Boyle-Roden, N. Hofer, K. K .Dey and P. J. Grandinetti, and M . Caffrey “High-Resolution H-1 NMR of a Lipid Cubic phase Using a solution NMR Probe”, *Journal of Magnetic Resonance*, **189** , 13-19 (2007)
4. Nicole M. Trease, Krishna K. Dey and P. J. Grandinetti. “RF Field Dependence of the Central Transition Pulse on Sensitivity Enhancement of Half-Integer Quadrupolar Nuclei NMR.”, *Journal of Magnetic Resonance*, **200** , 334-339 (2009)

FIELDS OF STUDY

Major Field: Chemistry

Specialization: Nuclear Magnetic Resonance

TABLE OF CONTENTS

Abstract	ii
Dedication	iii
Acknowledgments	v
Vita	vi
List of Figures	xi
CHAPTER	PAGE
1 Introduction	1
1.1 Introduction	1
1.2 General form of NMR Hamiltonian	2
1.2.1 Zeeman	7
1.2.2 Nuclear Shielding	8
1.2.3 Magnetic Dipole Coupling	10
1.2.4 Electric Quadrupole Coupling	12
1.2.5 Single Crystal and Powder Pattern	16
1.2.6 Magic Angle Spinning	17
1.3 Overview of Thesis	18
2 High-Resolution ^1H NMR of a Lipid Cubic Phase Using a Solution NMR Probe	22
2.1 Introduction	22
2.2 Materials and Methods	26
2.2.1 Materials	26
2.2.2 Sample Preparation	26
2.2.3 X-ray Diffraction	27
2.2.4 NMR	28
2.3 Results and Discussion	28
2.3.0.1 Incorporation of L-Tryptophan and Rubipy	30
2.4 Conclusion	37

3	Trading Information for sensitivity: CPMG acquisition in solids	41
	3.1 Introduction	41
	3.2 Experimental	43
	3.2.1 Span	44
	3.3 TOP processing for CPMG data	45
	3.4 Results and Discussion	51
	3.4.1 First-order Chemical Shift	51
	3.4.2 Second-Order Quadrupolar Coupling	58
	3.5 Summary	64
4	Enhancing Sensitivity in 2D PASS NMR with CPMG Acquisition	69
	4.1 Introduction	69
	4.2 Experimental	72
	4.2.1 Sample Preparation	72
	4.2.2 Nuclear Magnetic Resonance Spectroscopy	73
	4.3 Results and Discussion	74
	4.3.1 2D PASS	74
	4.3.2 2D PASS CPMG	77
	4.3.3 2D PASS CPMG Phase Cycling	78
	4.3.3.1 Cogwheel Phase Cycling for CPMG pulses	78
	4.3.4 2D PASS CPMG Processing	81
	4.3.5 Application of 2D ²⁹ Si PASS and PASS CPMG NMR to Silicate Glasses	82
	4.4 Summary	91
5	Correlation of Anisotropic Interactions for Integer Spin Nuclei	92
	5.1 Introduction	92
	5.2 Experimental	94
	5.2.1 ² H NMR	94
	5.2.2 Sample Preparation	96
	5.3 Results and Discussion	96
	5.3.1 Double Quantum	98
	5.3.2 3-pulse d Echo Experiment	101
	5.3.3 3-pulse p echo sequence	104
	5.4 Conclusion	107
	CHAPTER	PAGE
A	110
	A.1 Chapter 3	110
	A.1.1 Periodic Signals and Sidebands	110
	A.1.2 CPMG Signal	111

A.2 Chapter 4	112
A.2.1 Mapping and Coordination (Affine) Transformation	112
A.3 Derivations	114
A.3.1 Time Domain Signal	114
A.3.2 Sideband Amplitudes in Polycrystalline Samples	115
A.4 Phase Adjusted Spinning Sideband Experiment (PASS)	117
Bibliography	119

LIST OF FIGURES

FIGURE	PAGE
1.1	Typical NMR spectrum of a single crystal with single site (left). Typical NMR spectrum of a powder sample (right). (Adapted from Philip Grandinetti's NMR course note with permission.) 16
1.2	Simulated solid-state NMR lineshapes for a spin-1/2 nucleus with a given chemical shift anisotropy as a function of rotor angle. On the left all spectra are normalized to have the same maximum intensity. On the right all spectra are normalized to have the same area. (Adapted from Philip Grandinetti's NMR course note with permission.) 19
1.3	Simulated solid-state magic angle spinning NMR spectrum for a spin-1/2 nucleus with a given chemical shift anisotropy as function of MAS spinning speed. On the left hand all spectra are normalized to have the same maximum intensity. On the right all spectra are normalized to have the same area. (Adapted from Philip Grandinetti's NMR course note with permission.) 20
1.4	(A) Static spectra of different Q^n species. (B) MAS spectra of different Q^n species with spinning speed of 1 kHz. (Adapted from Samantha Vicker thesis and P.Zhang, C. Dunlap, P. Florian, P. J. Grandinetti, I. Farnan, and J. F. Stebbins, <i>J. Non. Cryst., Solids.</i> 204, 294, 1996) 21
2.1	Cartoon representation of the various mesophases formed by monoolein and water. Individual lipids are shown as lollipop figures with the pop and stick parts representing the polar head groups and the apolar acyl chain, respectively. The colored regions represent water. 23

2.2	Small-angle X-ray diffraction patterns of monoolein/water samples in the cubic-Ia3d phase recorded at 20 °C. Sample were prepared at 37 %(w/w) hydration without additive (A, B, C), and with tryptophan (D) and rubipy (E) as described under Methods. Measurements were made on fresh samples (A, B, D, E) and on a sample that was 2 months old (C). The lattice parameters for the different samples are 149 Å (A, B), 127 Å (C), 148 Å (D) and 146 Å (E).	24
2.3	¹ H NMR spectrum of the cubic-Ia3d phase formed by monoolein at 37 %(w/w) water in a glass X-ray capillary. Data were collected on a 600 MHz spectrometer (8 KHz spectral width, 32k points, 128 acquisitions) at 20 °C without spinning. The spectrum was processed without apodization. The X-ray diffraction pattern of this sample is shown in Fig. 2.2C. The molecular structure of monoolein and the labeling used to identify resonances are shown at the top of the figure. A small amount of 2-monoolein is also present due to isomerization of 1-monoolein (see text). It gives rise to the additional resonances near 3.7 ppm.	31
2.4	Expanded view of the ¹ H- ¹ H t-ROESY spectrum of the cubic-Ia3d phase recorded using monoolein at 37 %(w/w) hydration in a glass capillary. Data were recorded on a 600 MHz spectrometer under the following conditions: pulse sequence, roesyph; sweep width, 1k × 512 points; 16 dummy scans; 8 acquisitions; 400 msec mixing time; 2500 Hz spin-lock field; 100 μsec π/2 pulse. The spectrum reveals NOE crosspeaks between the vicinal hydrogens of the glycerol 1 and 3 -CH ₂ groups, V ₁ and V ₃ , respectively, and chemical exchange crosspeaks between the hydroxyl groups of glycerol, G _G , and between glycerol's hydroxyls and water, G _W	33
2.5	¹ H NMR spectra of rubipy in bulk aqueous solution (upper panel) and incorporated into the cubic-Ia3d phase of monoolein at 37 %(w/w) hydration (lower panel). Spectra were processed without apodization and were externally referenced to DSS. The concentration of rubipy in the aqueous solution was 10 mg/mL. The molecular structure of and proton identities in rubipy are shown in the upper panel. Individual resonances in the two spectra are labeled according to the molecular structure.	35
2.6	Downfield region of the ¹ H NMR spectra of L-tryptophan in bulk aqueous solution (upper panel) and in the cubic-Ia3d phase of monoolein at 37 %(w/w) water (lower panel). Spectra were processed without apodization and externally referenced to DSS. The concentration of tryptophan in the aqueous solution was 8 mg/mL.	36

3.1	CPMG pulse sequence and coherence transfer pathway used in this study.	43
3.2	(A) CPMG echoes with coordinate definitions and timings. (B) Sampling trajectory (blue lines) of the CPMG data in the 2D $t_1 - t_2$ and $k - t'_2$ coordinate systems. Identical data sets run parallel in the 2D plane and are separated by 2τ in $t_1 - t_2$ coordinate system. (C) Affine transformed 2D data set that correlates t_1 and t_2	47
3.3	(A) ^{87}Rb TOP-CPMG MAS spectrum of RbClO_4 . The ω_1 dimension contains all the unrefocused frequencies and the ω_2 dimension contains all frequencies. The contour level for the 2D contour plot is 20% to 100% with a linear increment of 4.2%, of the the maximum amplitude. (B) The CPMG-enhanced 1D spectrum obtained from the $\omega_1 = 0$ cross-section.	49
3.4	The static CPMG experimental spectra of ^{207}Pb resonance in $\text{Pb}(\text{NO}_3)_2$ powder sample as function of π pulse spacing. (A) Processed using “spikelet” approach of Larsen et.al [2] . (B) Processed using modified TOP [3] data processing method. Also shown are the “best-fit” model lineshapes which take signal truncation inside 2τ acquisition window into account.	50
3.5	Standard deviation of ^{207}Pb chemical shift tensor principal components (δ_{11} , δ_{22} , δ_{33}) extracted from simulated ^{207}Pb resonance CPMG spectra as a function of $\Omega 2\tau$ for different η while keeping span ($\Omega = 4.58$ kHz) and pre-CPMG signal to noise ratio ($\text{S/N}=2.30$) constant.	54
3.6	Standard deviation of ^{207}Pb chemical shift tensor principal components (δ_{11} , δ_{22} , δ_{33}) extracted from simulated ^{207}Pb resonance CPMG spectra as a function of $\Omega 2\tau$ for different pre-CPMG signal to noise ratios while keeping span ($\Omega = 4.58$ kHz) and asymmetry parameter ($\eta = 1$) constant.	55
3.7	The CPMG-MAS experimental spectra of ^{87}Rb resonance in RbClO_4 powder sample as a function of π pulse spacing, which was synchronized to the rotor period of $80 \mu\text{s}$ ($\nu_R = 12.5$ kHz). (A) CPMG data processed by “spikelet” approach of Larsen et.al [2]. (B) CPMG data processed by TOP [3] approach. Also shown are the “best-fit” model lineshapes which take signal truncation inside 2τ acquisition window into account.	56

3.8	The standard deviation of the ^{87}Rb quadrupolar coupling constant and asymmetry parameter extracted from simulated ^{207}Pb resonance CPMG-MAS spectra as a function of $\Omega 2\tau$ for $\eta_q = 0.21$ and $\eta_q = 1$, while keeping span ($\Omega_{q,MAS}=4.48$ kHz) and pre-CPMG signal-to-noise ratio ($S/N= 6.93$) constant. A spinning speed of 12.5 kHz was used for simulation.	60
3.9	The static CPMG experimental spectra of ^{87}Rb resonance in RbClO_4 powder sample as function of π pulse spacing. Top row is processed using “spikelet” approach of Larsen et.al [2]. The bottom row is processed using our modified TOP [3] processing method. Also shown are the “best-fit” model lineshapes which take signal truncation inside 2τ acquisition window into account.	61
4.1	2D PASS pulse sequence from Antzutkin et al. [4] where Θ represents the rotor pitch and Ω_R is the rotor spinning frequency.	72
4.2	2D PASS-CPMG pulse sequence where τ_r is the rotor period, n is an integer corresponding to the number of rotor periods, $\phi_o = \phi_2 = 0$, ϕ_1 is given in equation 4.3.20, and ϕ_{dig} is given in equation 4.3.21.	73
4.3	^{29}Si 2D PASS CPMG NMR time domain data for a sequence a) where the CPMG pulses are not phase cycled, demonstrating that even echoes do not evolve in the rotor pitch dimension and b) where a Cogwheel phase cycle is used for all CPMG pulses, demonstrating that even echoes are removed. Also, for a) the 7^{th} , 8^{th} and 9^{th} echoes have contributions from unwanted coherence pathways while those in b) are unaffected.	76
4.4	Schematic of the TOP approach to CPMG processing and subsequent reorganization into a 2D PASS dataset.	83
4.5	Comparison between the a) ^{29}Si 2D PASS CPMG NMR spectrum ($S/N = 137$) and the b) ^{29}Si 2D PASS NMR spectrum ($S/N = 72$) of a $\text{K}_2\text{O} \cdot 2.2\text{SiO}_2$ glass.	84
4.6	The ^{29}Si a) 2D PASS NMR spectrum of the ^{29}Si -enriched potassium disilicate glass, b) 2D PASS CPMG NMR spectrum of the ^{29}Si -enriched potassium disilicate glass, and c) 2D PASS CPMG NMR spectrum of the potassium disilicate glass with silicon in natural abundance. Representative cross sections along the sideband dimension are provided where solid lines represent experimental spectra and dashed lines represent the least-squares fit simulation.	88

4.7	Reconstructed 1D lineshape from the deconstruction of the a) 2D PASS NMR spectrum of the ^{29}Si -enriched potassium disilicate glass, b) 2D PASS CPMG NMR spectrum of the ^{29}Si -enriched potassium disilicate glass, and c) 2D PASS CPMG NMR spectrum of the potassium disilicate glass with silicon in natural abundance. Each of the three Gaussians represent the relative contributions from $\text{Q}^{(2)}$, $\text{Q}^{(3)}$, and $\text{Q}^{(4)}$, circles represent the 1D projection along the MAS dimension, and dashed lines are the total least squares best fit.	89
5.1	a) Double quantum pulse sequence. (b) d -echo experiment proposed by Wimperis. (c) p -echo experiment proposed in this study. (Here, we define $\mathbf{p} = m_j - m_i$ and $\mathbf{d} = m_j^2 - m_i^2$)	95
5.2	(a) Unsheared time domain ^2H DQ signal of DHMB. (b) Sheared time domain data (c) 2DFT of (a). (d) 2DFT of (b).	100
5.3	2D Double quantum experimental spectrum of ^2D in $\text{CuCl}_2 \cdot 2\text{D}_2\text{O}$. . .	101
5.4	^2H NMR time domain spectrum from the experiment proposed in a) Antonijevic and Wimperis [1] (left) and the sequence from this study (right), b) the sheared time domain data, and c) the 2D frequency domain spectrum.	102
5.5	A) Two dimensional sheared spectrum of ^2D NMR from three pulse d -echo experiment with separated quadrupolar and CSA dimensions. The pulse imperfection causes unwanted line in 2D spectrum marked by *. B) Two dimensional sheared spectrum of ^2D NMR using three pulse p -echo experiment with separated quadrupolar and CSA dimensions. Both spectra are taken under using same number of scan and same pulse calibrations.	103
5.6	Projections taken along the F1 and F2 axis illustrating the opposite refocusing of the <i>d</i> -echo and <i>p</i> -echo sequences.	108
A.1	(A) Time dependent frequency and (B) time dependent phase for the two pathway signals in the CPMG experiment. (C) The time dependent phase of the detected CPMG signal.	111

CHAPTER 1

INTRODUCTION

1.1 Introduction

Nuclear Magnetic Resonance (NMR) spectroscopy is one of the most important characterization techniques in chemistry today. The use of liquid-state NMR not only allows us to identify organic compounds, but also has gained significant popularity for finding the complex structure of biologically active peptides, proteins, and nucleic acids. Beyond chemistry, Magnetic Resonance Imaging (MRI) allows us to get a detailed noninvasive image of the human body without the use of harmful radiation like X-rays. While solid state NMR has within it all the power (and more) of liquid-state NMR and MRI, unfortunately, it has not become a routine characterization technique. Part of the challenge is that solid-state NMR is still at a level of complexity that requires the expertise of solid-state NMR spectroscopist to setup, to process and interpret the data, even when commercial instruments are available.

The solid-state NMR lines are broad due to un-averaged frequency anisotropy. Frequency anisotropy in nuclear magnetic resonance spectroscopy is a rich source of detail concerning structure and dynamics at the macroscopic level down to the molecular level. At the macroscopic level these anisotropies can occur as a result of inhomogeneities in the external magnetic field, variations in magnetic susceptibilities, or through the intentional use of magnetic field gradients as in magnetic resonance

imaging. At the molecular level frequency anisotropy arises through magnetic dipolar couplings amongst nuclei and through interactions of the nuclear multipole moments with surrounding electrons. While the manifestation of these molecular level anisotropies in solution state NMR is primarily through relaxation, its effects are seen directly in solid-state NMR spectra as the powder pattern lineshape.

Early in the history of NMR it was realized that inhomogeneous anisotropic broadenings can be removed through sample rotation [5–7]. In solution-state NMR, it is a standard approach to average away broadenings from magnetic field inhomogeneities [5], and a popular and routine method for eliminating second-rank anisotropic broadenings in solid-state NMR is magic-angle spinning (MAS) [6, 7], particularly when combined with the sensitivity enhancement of cross-polarization (CP/MAS) [8, 9]. Recent advances of multiple pulse, and multiple quantum spectroscopy (MQ) in the last twenty years has significantly simplified the complex solid spectra.

In the next section I will discuss about the theoretical background behind NMR.

1.2 General form of NMR Hamiltonian

There are many ways a nuclear spin can communicate with its surroundings. The interaction energy of different communications with its surroundings is represented by different Hamiltonians. The total Hamiltonian of a spin system can be separated into two different categories [10–13], external (\hat{H}_{ext}) and internal (\hat{H}_{int}) Hamiltonians.

$$\hat{H}_{tot} = \hat{H}_{ext} + \hat{H}_{int} \tag{1.2.1}$$

The external Hamiltonian consists of interactions with the external static magnetic field and the applied radio frequency (RF) field. The internal Hamiltonian consists of different kinds of spin interactions (dipolar couplings, quadrupolar couplings, nuclear shielding and spin lattice).

Assuming that the symmetry of a solid sample is such that all spin interactions can be represented by second rank Cartesian tensors, we can write any nuclear Hamiltonian in a general form [10]

$$\begin{aligned} \hat{H}_\lambda &= \hbar \Lambda^{\{\lambda\}} \hat{\mathbf{U}} \cdot [\mathbf{R}^{\{\lambda\}}] \cdot \mathbf{V} \\ &= \hbar \Lambda^{\{\lambda\}} \begin{pmatrix} \hat{U}_x & \hat{U}_y & \hat{U}_z \end{pmatrix} \begin{pmatrix} R_{xx}^{\{\lambda\}} & R_{xy}^{\{\lambda\}} & R_{xz}^{\{\lambda\}} \\ R_{yx}^{\{\lambda\}} & R_{yy}^{\{\lambda\}} & R_{yz}^{\{\lambda\}} \\ R_{zx}^{\{\lambda\}} & R_{zy}^{\{\lambda\}} & R_{zz}^{\{\lambda\}} \end{pmatrix} \begin{pmatrix} V_x \\ V_y \\ V_z \end{pmatrix}. \end{aligned} \quad (1.2.2)$$

Here, the $\Lambda^{\{\lambda\}}$ consists of fundamental constants. The vector $\hat{\mathbf{U}}$ and the vector \mathbf{V} are nuclear spin vectors. The $R_{ik}^{\{\lambda\}}$ ($i, k = x, y, z$) are spin state independent second rank tensor elements given by

$$R_{ik}^{\{\lambda\}} = \frac{1}{\Lambda^{\{\lambda\}}} \frac{\partial^2 E^{\{\lambda\}}}{\partial U_i \partial V_k}, \quad (1.2.3)$$

where $E^{\{\lambda\}}$ is the energy of the nuclear spin's λ interaction.

Using spherical tensor, the general Hamiltonian can also be written

$$\hat{H}_\lambda = \hbar \Lambda^{\{\lambda\}} \sum_{ik=xyz} R_{ik}^{\{\lambda\}} T_{ik}(\hat{\mathbf{U}}, \mathbf{V}), \quad (1.2.4)$$

where $\hat{T}_{ik}^{\{\lambda\}}$ are cartesian tensor elements constructed from the two vectors, $\hat{\mathbf{U}}$ and \mathbf{V} :

$$\hat{T}_{ik}(\mathbf{U}, \mathbf{V}) = \hat{U}_i V_k. \quad (1.2.5)$$

A real second-rank cartesian tensor $X_{ik}^{\{\lambda\}}$ can be decomposed into irreducible representations as

$$\begin{aligned} X_{ik} &= E\delta_{ik} + A_{ik} + S_{ik}, \\ E &= \frac{1}{3}\text{Tr}\{\mathbf{X}\}, \\ A_{ik} &= \frac{1}{2}(X_{ik} - X_{ki}), \\ S_{ik} &= \frac{1}{2}(X_{ik} + X_{ki}) - \frac{1}{3}\text{Tr}\{\mathbf{X}\}\delta_{ik}, \end{aligned} \quad (1.2.6)$$

where E is invariant under rotations of the system, A_{ik} is the traceless anti-symmetric part, and S_{ik} is the traceless symmetric part of the tensor.

An irreducible tensor of rank one can be formed from the antisymmetric components, and the principal axis system of this tensor is defined as the coordinate system where

$$\lambda_x^{(a)} = \lambda_y^{(a)} = 0, \quad \lambda_z^{(a)} = \zeta^{(a)} = \sqrt{A_{yz}^2 + A_{zx}^2 + A_{xy}^2}. \quad (1.2.7)$$

where $\zeta^{(a)}$ is the antisymmetric first-rank tensor anisotropy.

The principal axis system of the second-rank symmetric tensor is defined as the coordinate system where \mathbf{S} is diagonal with principal components $\lambda_{zz}^{(s)}$, $\lambda_{yy}^{(s)}$, and $\lambda_{xx}^{(s)}$ ordered [14] such that

$$|\lambda_{zz}^{(s)}| > |\lambda_{yy}^{(s)}| > |\lambda_{xx}^{(s)}|, \quad (1.2.8)$$

and since \mathbf{S} is traceless we have

$$\lambda_{zz}^{(s)} + \lambda_{yy}^{(s)} + \lambda_{xx}^{(s)} = 0. \quad (1.2.9)$$

Additionally, we define the second-rank symmetric tensor anisotropy, ζ , and asymmetry parameter, η , according to

$$\zeta = \lambda_{zz}^{(s)}, \quad \text{and} \quad \eta = \frac{\lambda_{xx}^{(s)} - \lambda_{yy}^{(s)}}{\zeta}. \quad (1.2.10)$$

The second-rank cartesian tensor $X_{ik}^{\{\lambda\}}$ can be decomposed into irreducible spherical tensor components given by [15]

$$\begin{aligned} X_{0,0} &= -\frac{1}{\sqrt{3}}[X_{xx} + X_{yy} + X_{zz}], \\ X_{1,0} &= -\frac{i}{\sqrt{2}}[X_{xy} - X_{yx}], \\ X_{1,\pm 1} &= -\frac{1}{2}[X_{zx} - X_{xz} \pm i(X_{zy} - X_{yz})], \\ X_{2,0} &= \frac{1}{\sqrt{6}}[3X_{zz} - (X_{xx} + X_{yy} + X_{zz})], \\ X_{2,\pm 1} &= \mp \frac{1}{2}[X_{xz} + X_{zx} \pm i(X_{yz} + X_{zy})], \\ X_{2,\pm 2} &= \frac{1}{2}[X_{xx} - X_{yy} \pm i(X_{xy} + X_{yx})]. \end{aligned} \quad (1.2.11)$$

Calculated in terms of E , A_{ik} , and S_{ik} the irreducible spherical tensor components are given by

$$\begin{aligned}
X_{0,0} &= -\sqrt{3} E, \\
X_{1,0} &= -i\sqrt{2} A_{xy}, \\
X_{1,\pm 1} &= -(A_{zx} \mp iA_{yz}), \\
X_{2,0} &= \sqrt{\frac{3}{2}} S_{zz}, \\
X_{2,\pm 1} &= \mp(S_{zx} \pm iS_{zy}), \\
X_{2,\pm 2} &= \frac{1}{2}(S_{xx} - S_{yy} \pm i2S_{xy}).
\end{aligned} \tag{1.2.12}$$

The inverse relation between second rank spherical tensor and second rank symmetric cartesian tensor elements are

$$\begin{aligned}
E &= -\frac{1}{\sqrt{3}} X_{0,0} \\
A_{xy} &= \frac{i}{\sqrt{2}} X_{1,0}, \quad A_{zx} = -\frac{1}{2}(X_{1,1} + X_{1,-1}), \quad A_{yz} = -\frac{i}{2}(X_{1,1} - X_{1,-1}), \\
S_{xx} &= \frac{1}{2}(X_{2,2} + X_{2,-2}) - \frac{1}{\sqrt{6}} X_{2,0}, \quad S_{xy} = S_{yx} = \frac{i}{2}(X_{2,-2} - X_{2,2}), \\
S_{yy} &= -\frac{1}{2}(X_{2,2} + X_{2,-2}) - \frac{1}{\sqrt{6}} X_{2,0}, \quad S_{xz} = S_{zx} = \frac{1}{2}(X_{2,-1} - X_{2,1}), \\
S_{zz} &= \sqrt{\frac{2}{3}} X_{2,0}, \quad S_{yz} = S_{zy} = \frac{i}{2}(X_{2,-1} + X_{2,1}).
\end{aligned}$$

In the principal axis system of \mathbf{A} we can show

$$\rho_{1,0} = -i\sqrt{2} \zeta^{(a)}, \quad \rho_{1,\pm 1} = 0. \tag{1.2.13}$$

In the principal axis system of \mathbf{S} we can show

$$\rho_{2,0} = \sqrt{\frac{3}{2}} \zeta, \quad \rho_{2,\pm 1} = 0, \quad \rho_{2,\pm 2} = \frac{1}{2} \zeta \eta. \tag{1.2.14}$$

We also find

$$\rho_{2,0} = \sqrt{\frac{3}{2}} \lambda_{zz}^{(s)}, \quad \rho_{2,\pm 1} = 0, \quad \rho_{2,\pm 2} = \frac{1}{2}(\lambda_{xx}^{(s)} - \lambda_{yy}^{(s)}), \tag{1.2.15}$$

and conversely,

$$\lambda_{zz}^{(s)} = \sqrt{\frac{2}{3}} \rho_{2,0}, \quad \lambda_{xx}^{(s)} = \rho_{2,\pm 2} - \frac{1}{\sqrt{6}} \rho_{2,0}, \quad \lambda_{yy}^{(s)} = -\rho_{2,\pm 2} - \frac{1}{\sqrt{6}} \rho_{2,0}. \tag{1.2.16}$$

	quadrupolar	nuclear shielding	dipolar	J
λ	q	σ	d	J
$\hat{\mathbf{U}}$	$\hat{\mathbf{I}}$	$\hat{\mathbf{I}}$	$\hat{\mathbf{I}}_1$	$\hat{\mathbf{I}}_1$
\mathbf{V}	$\hat{\mathbf{I}}$	\mathbf{B}	$\hat{\mathbf{I}}_2$	$\hat{\mathbf{I}}_2$
$\Lambda^{\{\lambda\}}$	$\frac{eQ_I}{2I(2I-1)}$	γ_I	$-(\mu_0/4\pi)\gamma_1\gamma_2\hbar$	2π
$\rho_{0,0}^{\{\lambda\}}$	0	$-\sqrt{3} \sigma_{iso}$	0	$-\sqrt{3} J_{iso}$
$\rho_{1,0}^{\{\lambda\}}$	0	$-i\sqrt{2} \zeta_\sigma^{(a)}$	0	$-i\sqrt{2} \zeta_J^{(a)}$
$\rho_{1,\pm 1}^{\{\lambda\}}$	0	0	0	0
$\rho_{2,0}^{\{\lambda\}}$	$\sqrt{\frac{3}{2}} \zeta_q$	$\sqrt{\frac{3}{2}} \zeta_\sigma$	$\sqrt{\frac{3}{2}} \zeta_d$	$\sqrt{\frac{3}{2}} \zeta_J$
$\rho_{2,\pm 1}^{\{\lambda\}}$	0	0	0	0
$\rho_{2,\pm 2}^{\{\lambda\}}$	$\eta_q \zeta_q/2$	$\eta_\sigma \zeta_\sigma/2$	0	$\eta_J \zeta_J/2$

Table 1.1: Definitions for the irreducible spherical tensor elements for the quadrupolar, nuclear shielding, and dipolar coupling tensors in the principal axis system (PAS) for a Hamiltonian in the form of Eq. (1.2.17). Here we define the first rank nuclear shielding or J antisymmetric tensor in its PAS as $\rho_{1,0}$, which is related to its value, $r_{1,m}$, in the PAS of the second rank symmetric tensor by $r_{1,m} = \sum_m D_{0,m}^{(2)}(0, \beta, \gamma) \rho_{1,0}$.

Finally, using the definitions of this section, including Tables 1.1 and 1.2, we can re-express Eq. (1.2.4) in terms of irreducible tensor elements of ranks $L = 0, 1$, and 2 as

$$\hat{H}_\lambda = \Lambda^{\{\lambda\}} \sum_{L=0}^2 \sum_{m=-L}^L (-1)^m R_{L,-m}^{\{\lambda\}} \hat{T}_{L,m}^{\{\lambda\}}(\mathbf{U}, \mathbf{V}). \quad (1.2.17)$$

k	$T_{0,k}(\mathbf{U}, \mathbf{V})$	$T_{1,k}(\mathbf{U}, \mathbf{V})$	$T_{2,k}(\mathbf{U}, \mathbf{V})$
0	$-\frac{1}{\sqrt{3}}\mathbf{U} \cdot \mathbf{V}$	$-\frac{1}{2\sqrt{2}}[U_+V_- - U_-V_+]$	$\frac{1}{\sqrt{6}}[3U_zV_z - \mathbf{U} \cdot \mathbf{V}]$
± 1	-	$\frac{1}{2}[U_zV_{\pm} - U_{\pm}V_z]$	$\mp \frac{1}{2}[U_zV_{\pm} + U_{\pm}V_z]$
± 2	-	-	$\frac{1}{2}U_{\pm}V_{\pm}$

Table 1.2: Irreducible spherical tensors, $T_{J,k}(\mathbf{U}, \mathbf{V})$, formed from the tensor product of two vectors \mathbf{U} and \mathbf{V} , and expressed in terms of their cartesian components for $J \leq 2$.

1.2.1 Zeeman

The application of a magnetic field \mathbf{B} produces an interaction energy for nuclei with nonzero spin angular momentum. The Hamiltonian describing the interaction energy between nuclear dipole moments and the static external magnetic field is the called Zeeman Hamiltonian. In most of cases, the Zeeman interaction is the strongest interaction compared to other spin interactions. Hence, the eigenvalues and eigenstates of the Zeeman Hamiltonian are considered as a basis set [10–13] for the perturbation expansion of the other important interactions like Chemical shift Anisotropy, Dipolar coupling, and J-coupling. The Zeeman Hamiltonian is given as,

$$\hat{H}_z = -\hat{\boldsymbol{\mu}} \cdot \mathbf{B} = -\hbar\gamma\hat{\mathbf{I}} \cdot \mathbf{B}, \quad (1.2.18)$$

where

$$\boldsymbol{\mu} = \gamma\hbar\mathbf{I}. \quad (1.2.19)$$

In the above equation, \mathbf{B} is the static external magnetic field, γ is the nuclear gyromagnetic ratio, and \mathbf{I} is the nuclear spin angular momentum vector.

1.2.2 Nuclear Shielding

The nucleus in an atom is partially shielded from the external applied magnetic field due to the presence of the electron cloud. When an external magnetic field B_0 is applied, it induces currents in the electron cloud and the circulating currents generate a magnetic field. Thus, the local magnetic field experienced by the nucleus is the sum of the external magnetic field and the induced magnetic field due to the electron cloud. For example, two protons in different electronic environments under the same external magnetic field experience different local magnetic fields due to the induced magnetic field of the electron cloud. The induced magnetic field is generally very small compared to the external static magnetic field B_0 . However, this slight change in local magnetic field is enough to give a measurable difference in the spin precession frequencies and causes chemically or crystallographically inequivalent nuclei to have different resonance frequencies. This interaction is called nuclear shielding. The induced magnetic field is not necessarily parallel to the external magnetic field, but depends on the orientation of the molecule with respect to the external magnetic field. Hence, the nuclear shielding is an anisotropic interaction. The nuclear shielding Hamiltonian is given as [10],

$$\hat{H}_\sigma = \hat{\boldsymbol{\mu}} \cdot \boldsymbol{\sigma} \cdot \mathbf{B} = \hbar\gamma_I \hat{\mathbf{I}} \cdot \boldsymbol{\sigma} \cdot \mathbf{B}, \quad (1.2.20)$$

and written in terms of irreducible spherical tensors as

$$\hat{H}_\sigma = \hbar\gamma_I \sum_{L=0}^2 \sum_{m=-L}^L (-1)^m R_{L,-m}^{\{\sigma\}} \hat{T}_{L,m}(\mathbf{I}, \mathbf{B}). \quad (1.2.21)$$

Here $\hat{T}_{L,m}(\mathbf{I}, \mathbf{B})$ is formed from the spin angular momentum vector \mathbf{I} and the magnetic field vector \mathbf{B} . Using the Clebsch-Gordon coefficients we expand $\hat{T}_{L,m}(\mathbf{I}, \mathbf{B})$ in Eq. (1.2.21) to obtain

$$\hat{T}_{L,m}(\mathbf{I}, \mathbf{B}) = \sum_n \langle L \ m | 1 \ 1 \ n+m \ -n \rangle \hat{T}_{1,n+m}(\mathbf{I}) B_{1,-n}, \quad (1.2.22)$$

and since we normally define $B_{1,0} = B_0$ and $B_{1,\pm 1} = 0$, this becomes

$$\hat{T}_{L,m}(\mathbf{I}, \mathbf{B}) = \langle L m | 1 1 m 0 \rangle \hat{T}_{1,m}(\mathbf{I}) B_{1,0}, \quad (1.2.23)$$

giving us

$$\hat{H}_\sigma = -\hbar\omega_0 \sum_{L=0}^2 \sum_{m=-1}^1 (-1)^m R_{L,-m}^{\{\sigma\}} \langle L m | 1 1 m 0 \rangle \hat{T}_{1,m}(\mathbf{I}), \quad (1.2.24)$$

where

$$\begin{aligned} R_{0,0}^{\{\sigma\}} &= -\sqrt{3} \sigma_{iso}, \\ R_{1,0}^{\{\sigma\}} &= -(i/\sqrt{2})[\sigma_{xy} - \sigma_{yx}], \\ R_{1,\pm 1}^{\{\sigma\}} &= -\frac{1}{2}[\sigma_{zx} - \sigma_{xz} \pm i(\sigma_{zy} - \sigma_{yz})], \\ R_{2,0}^{\{\sigma\}} &= \sqrt{\frac{1}{2}}[\sigma_{zz} - \sigma_{iso}], \\ R_{2,\pm 1}^{\{\sigma\}} &= \mp \frac{1}{2}[\sigma_{xz} + \sigma_{zx} \pm i(\sigma_{yz} + \sigma_{zy})], \\ R_{2,\pm 2}^{\{\sigma\}} &= \frac{1}{2}[\sigma_{xx} - \sigma_{yy} \pm i(\sigma_{xy} + \sigma_{yx})]. \end{aligned} \quad (1.2.25)$$

Following the IUPAC definitions for the nuclear shielding or nuclear shielding interaction [14]. The isotropic nuclear shielding, σ_{iso} , is derived from the trace of the shielding tensor,

$$\sigma_{iso} = \frac{1}{3}(\sigma_{xx} + \sigma_{yy} + \sigma_{zz}). \quad (1.2.26)$$

In the principal axis system of the antisymmetric shielding tensor we define

$$\rho_{1,0}^{\{\sigma\}} = -i\sqrt{2} \zeta_\sigma^{(a)}, \quad \rho_{1,\pm 1}^{\{\sigma\}} = 0, \quad (1.2.27)$$

where

$$\zeta_\sigma^{(a)} = \frac{1}{2} \sqrt{(\sigma_{xy} - \sigma_{yx})^2 + (\sigma_{yz} - \sigma_{zy})^2 + (\sigma_{zx} - \sigma_{xz})^2}. \quad (1.2.28)$$

In the principal axis system of the second-rank symmetric cartesian shielding tensor, where $\lambda_{xx}^{\{\sigma\}}$, $\lambda_{yy}^{\{\sigma\}}$, and $\lambda_{zz}^{\{\sigma\}}$ are the principal components of the symmetric part of the shielding tensor, we define

$$\rho_{2,0}^{\{\sigma\}} = \zeta_\sigma / \sqrt{2}, \quad \rho_{2,\pm 1}^{\{\sigma\}} = 0, \quad \rho_{2,\pm 2}^{\{\sigma\}} = \eta_\sigma \zeta_\sigma / 2. \quad (1.2.29)$$

where the second-rank symmetric nuclear shielding tensor anisotropy, ζ_σ , is defined as

$$\zeta_\sigma = \lambda_{zz}^{\{\sigma\}}, \quad (1.2.30)$$

the second-rank symmetric nuclear shielding tensor asymmetry parameter is defined as

$$\eta_\sigma = \frac{\lambda_{xx}^{\{\sigma\}} - \lambda_{yy}^{\{\sigma\}}}{\zeta_\sigma}. \quad (1.2.31)$$

Using the first order perturbation correction of the nuclear shielding Hamiltonian, we can write the first-order nuclear shielding contribution to the $|i\rangle \rightarrow |j\rangle$ transition frequency as

$$\boxed{\Omega_\sigma^{(1)} = -\omega_0 \sigma_{iso} [\mathbf{S}^{\{\sigma\}} \cdot \mathbb{P}_I] - \omega_0 \zeta_\sigma [\mathbf{D}^{\{\sigma\}} \cdot \mathbb{P}_I]}. \quad (1.2.32)$$

where

$$\mathbf{S}^{\{\sigma\}} = -\frac{1}{\sigma_{iso}} \sqrt{\frac{1}{3}} R_{0,0}^{\{\sigma\}}, \quad \mathbf{D}^{\{\sigma\}} = \frac{1}{\zeta_\sigma} \sqrt{\frac{2}{3}} R_{2,0}^{\{\sigma\}}, \quad (1.2.33)$$

and

$$\mathbb{P}_I = \langle I, m_j | \hat{T}_{1,0}^{\circ}(\mathbf{I}) | I, m_j \rangle - \langle I, m_i | \hat{T}_{1,0}^{\circ}(\mathbf{I}) | I, m_i \rangle = m_j - m_i. \quad (1.2.34)$$

1.2.3 Magnetic Dipole Coupling

It is well known that magnetic dipole moments interact with external magnetic fields, which is the sole reason NMR exists. In similar way, a magnetic dipole moment generates a magnetic field. For example, in the presence of two spins, the first spins magnetic moment interacts with the magnetic field produced by the second spin and similarly, the second spin interacts with the magnetic field produced by the first spin. This interaction is called the through space dipolar interaction because the magnetic fields between the the nuclear spins propagate through space without

interfering with the electron cloud. Strength of the dipolar couplings depends on intermolecular distance. Thus, measurements of the dipolar couplings reveal detailed molecular structure and conformation. The through space magnetic dipole coupling Hamiltonian can be written [10–13] as

$$\hat{H}_d = -\frac{\mu_0}{4\pi} \hat{\boldsymbol{\mu}}_1 \cdot \mathbf{D} \cdot \hat{\boldsymbol{\mu}}_2 = -\frac{\mu_0}{4\pi} \hbar^2 \gamma_1 \gamma_2 \hat{\mathbf{I}}_1 \cdot \mathbf{D} \cdot \hat{\mathbf{I}}_2, \quad (1.2.35)$$

where μ_0 is the permeability constant ($4\pi \times 10^{-7}$ kg m s⁻² A⁻²) and \mathbf{D} is defined in a coordinate system with $\boldsymbol{\mu}_1$ at the origin and $\boldsymbol{\mu}_2$ at (x, y, z) and r as the distance between $\boldsymbol{\mu}_1$ and $\boldsymbol{\mu}_2$ and given by

$$D_{ik} = \frac{1}{r^3} \left(\frac{3r_i r_k}{r^2} - \delta_{ik} \right). \quad (r_i, r_k = x, y, z) \quad (1.2.36)$$

The dipolar coupling tensor, \mathbf{D} , is a traceless and axially symmetric tensor. The principal components of the \mathbf{D} tensor are

$$\lambda_{xx}^{\{d\}} = -\frac{1}{r^3}, \quad \lambda_{yy}^{\{d\}} = -\frac{1}{r^3}, \quad \lambda_{zz}^{\{d\}} = \frac{2}{r^3}. \quad (1.2.37)$$

Writing the dipole coupling Hamiltonian in terms of irreducible spherical tensors we have

$$\hat{H}_d = -\frac{\mu_0}{4\pi} \hbar^2 \gamma_1 \gamma_2 \sum_{m=-2}^2 (-1)^m R_{2,-m}^{\{d\}} \hat{T}_{2,m}(\mathbf{I}_1, \mathbf{I}_2), \quad (1.2.38)$$

where

$$\begin{aligned} R_{2,0}^{\{J\}} &= \sqrt{\frac{3}{2}} D_{zz}, \\ R_{2,\pm 1}^{\{J\}} &= \mp (D_{zx} \pm i(D_{zy})), \\ R_{2,\pm 2}^{\{J\}} &= \frac{1}{2} [D_{xx} - D_{yy} \pm i2D_{xy}]. \end{aligned} \quad (1.2.39)$$

In the principal axis system of the dipolar coupling tensor we define

$$\rho_{2,0}^{\{d\}} = \sqrt{\frac{3}{2}} \zeta_d, \quad \rho_{2,\pm 1}^{\{d\}} = 0, \quad \rho_{2,\pm 2}^{\{d\}} = 0. \quad (1.2.40)$$

where the second-rank symmetric dipolar coupling tensor anisotropy, ζ_d , is defined as

$$\zeta_d = \lambda_{zz}^{\{d\}} = \frac{2}{r^3}, \quad (1.2.41)$$

The dipolar splitting is given by

$$\omega_d = -\frac{\mu_0}{4\pi} \frac{\gamma_1 \gamma_2 \hbar}{r^3} = -\frac{2}{\zeta_d} \frac{\mu_0}{4\pi} \gamma_1 \gamma_2 \hbar. \quad (1.2.42)$$

For convenience in the derivations to follow we express the dipole coupling Hamiltonian as

$$\hat{H}_d = \hbar \omega_d \frac{2}{\zeta_d} \sum_m (-1)^m R_{2,-m}^{\{d\}} \hat{T}_{2,m}(\mathbf{I}). \quad (1.2.43)$$

The first-order weak dipolar coupling correction to the transition frequency is,

$$\boxed{\Omega_{d_{IS}}^{(1)} = \omega_d [\mathbf{D}^{\{d_{IS}\}} \cdot \mathbb{P}_I \mathbb{P}_S]}, \quad (1.2.44)$$

where

$$\mathbf{D}^{\{d_{IS}\}} = \frac{2}{\zeta_d} \sqrt{\frac{2}{3}} R_{2,0}^{\{d\}}, \quad (1.2.45)$$

and the $\mathbb{P}_I \mathbb{P}_S$ are calculated in the weakly coupled basis set, $|m_I m_S\rangle$.

Because of the motional averaging in an isotropic liquid, the secular part (commutes with Zeeman Hamiltonian) of the dipolar Hamiltonian becomes zero, but the non secular part does not and contributes to the relaxation effects. For a spin half system, the most important relaxation mechanism is dipole-dipole relaxation.

1.2.4 Electric Quadrupole Coupling

In addition to the nuclear spin, nuclei also have an electric charge. The multipole moment expansion of the nuclear charge can be written as a superposition of electric multipoles.

$$M(r) = M^{(0)}(r) + M^{(1)}(r) + M^{(2)} + \dots, \quad (1.2.46)$$

where, $M^{(0)}(r)$ is the monopole moment, $M^{(1)}(r)$ is the dipole moment, and $M^{(2)}(r)$ is the quadrupole moment. The monopole moment interacts with electric field, but it has no direct importance in NMR. Also, nuclear physicists have shown that nuclei do not possess an electric dipole moment. The electric quadrupole moment has direct importance in NMR, because, it interacts with surrounding electric field gradient generated by electron and other nucleus.

Fortunately, all the electric multipole moments except $M^{(0)}(r)$ vanish due to the spherical symmetric charge distribution for a spin-1/2 nuclei, but, for any nuclei with spin greater than 1/2, the electric charge distribution is not spherically symmetric and produces a non zero electrical quadrupole moment.

The Hamiltonian describing the interaction of the electric quadrupole moment of a nucleus of spin I with its surrounding electric field gradient (efg) is given by [10,11]

$$\hat{H}_q = \sum_{m=-2}^2 (-1)^m \mathcal{E}_{2,m} \hat{Q}_{2,-m}, \quad (1.2.47)$$

where the $\hat{Q}_{2,m}$ is the nuclear electric quadrupole moment operator. The energy states of the nucleus are described by the quantum numbers of the total nuclear angular momentum operator I and its projection m_I along the z axis, as well as others which we will denote by a general index γ . For a given nuclear eigenstate, the charge density, which depends on the quantum numbers I , m_I , and γ , is axially symmetric about the z -axis. Thus, in the principal axis system the only nonvanishing nuclear quadrupole moment is $\hat{Q}_{2,0}$, and a single constant called the nuclear quadrupole moment, $Q_{\gamma I}$, is defined as

$$\frac{1}{2}eQ_{\gamma I} = \langle \gamma I m_I = I | \hat{Q}_{2,0} | \gamma I m_I = I \rangle, \quad (1.2.48)$$

where e is the charge on the proton. Using the Wigner-Eckart theorem one can show that

$$\hat{Q}_{2,m} = \sqrt{\frac{3}{2}} \frac{eQ_{\gamma I}}{I(2I-1)} \hat{T}_{2,m}(\mathbf{I}), \quad (1.2.49)$$

obtaining

$$\hat{H}_q = \sqrt{\frac{3}{2}} \frac{eQ_{\gamma I}}{I(2I-1)} \sum_m (-1)^m \mathcal{E}_{2,-m} \hat{T}_{2,m}(\mathbf{I}). \quad (1.2.50)$$

The $\mathcal{E}_{2,m}$ are the expectation values of the electric field gradient, calculated from the ground state wavefunction of the system, and are given by

$$\mathcal{E}_{2,0} = \frac{1}{2} V_{zz}, \quad \mathcal{E}_{2,\pm 1} = \mp \frac{1}{\sqrt{6}} (V_{zx} \pm iV_{zy}), \quad \mathcal{E}_{2,\pm 2} = \frac{1}{2\sqrt{6}} (V_{xx} - V_{yy} \pm 2iV_{xy}),$$

where

$$V_{ik} = \frac{\partial^2 V(0)}{\partial \mathbf{r}_i \partial \mathbf{r}_k}. \quad (1.2.51)$$

Here $V(\mathbf{r})$ is the potential produced at the position \mathbf{r} by surrounding charges. Using the normalization [15]

$$R_{2,m}^{\{q\}} = \sqrt{6} \mathcal{E}_{2,m}, \quad (1.2.52)$$

we write the electric quadrupole coupling Hamiltonian in terms of spherical tensor elements as

$$\hat{H}_q = \frac{eQ_{\gamma I}}{2I(2I-1)} \sum_m (-1)^m R_{2,-m}^{\{q\}} \hat{T}_{2,m}(\mathbf{I}), \quad (1.2.53)$$

and in terms of the cartesian efg tensor as

$$\hat{H}_q = \frac{eQ_{\gamma I}}{2I(2I-1)} \hat{\mathbf{I}} \cdot \mathbf{V} \cdot \hat{\mathbf{I}}. \quad (1.2.54)$$

In this form the relationship between the spherical tensor and second-rank symmetric cartesian efg tensor is

$$\begin{aligned} R_{2,0}^{\{q\}} &= \sqrt{\frac{3}{2}} V_{zz}, \\ R_{2,\pm 1}^{\{q\}} &= \mp [V_{zx} \pm iV_{zy}], \\ R_{2,\pm 2}^{\{q\}} &= \frac{1}{2} [V_{xx} - V_{yy} \pm 2iV_{xy}]. \end{aligned} \quad (1.2.55)$$

In the principal axis system of the efg tensor, where the principal components of the second-rank symmetric cartesian efg tensor are $\lambda_{xx}^{\{q\}}$, $\lambda_{yy}^{\{q\}}$, and $\lambda_{zz}^{\{q\}}$, we define

$$\rho_{2,0}^{\{q\}} = \sqrt{\frac{3}{2}} \zeta_q, \quad \rho_{2,\pm 1}^{\{q\}} = 0, \quad \rho_{2,\pm 2}^{\{q\}} = \eta_q \zeta_q / 2, \quad (1.2.56)$$

where the second-rank symmetric efg tensor anisotropy, ζ_q , is defined as

$$\zeta_q = \lambda_{zz}^{\{q\}}, \quad (1.2.57)$$

and the second-rank symmetric efg tensor asymmetry parameter is defined as

$$\eta_q = \frac{\lambda_{xx}^{\{q\}} - \lambda_{yy}^{\{q\}}}{\zeta_q}. \quad (1.2.58)$$

The quadrupolar coupling constant is given by $C_q = eQ_{\gamma I} \zeta_q / h$ (or $eQ_{\gamma I} \zeta_q / (4\pi\epsilon_0 h)$ in S.I. units), and the quadrupolar splitting given by

$$\omega_q = \frac{6\pi C_q}{2I(2I-1)} = \frac{eQ_{\gamma I}}{2I(2I-1)} \cdot \frac{3\zeta_q}{\hbar}. \quad (1.2.59)$$

we can express the quadrupole Hamiltonian as

$$\hat{H}_q = \frac{\hbar\omega_q}{3\zeta_q} \sum_m (-1)^m R_{2,-m}^{\{q\}} \hat{T}_{2,m}(\mathbf{I}). \quad (1.2.60)$$

The first-order contribution to the transition frequency between levels j and i is given by

$$\boxed{\Omega_q^{(1)} = \omega_q [\mathbf{D}^{\{q\}} \cdot \mathfrak{d}_I]}, \quad (1.2.61)$$

where

$$\mathbf{D}^{\{q\}} = \frac{1}{3\zeta_q} R_{2,0}^{\{q\}}, \quad (1.2.62)$$

and

$$\mathfrak{d}_I = \langle I, m_j | \hat{T}_{2,0}^\circ(\mathbf{I}) | I, m_j \rangle - \langle I, m_i | \hat{T}_{2,0}^\circ(\mathbf{I}) | I, m_i \rangle = \sqrt{\frac{2}{3}} (m_j^2 - m_i^2). \quad (1.2.63)$$

1.2.5 Single Crystal and Powder Pattern

In a single crystal all the molecules are oriented with respect to each other and are periodically distributed on the lattice. For example, a single site ^{13}C NMR spectrum in a single crystal will be a single line, which will resonate at different frequency as the sample is reoriented. If we do a systematic study of the NMR frequency as a function of angle θ and ϕ (angles in the spherical polar coordinate), we can extract the chemical shift tensor parameters and orientation of its PAS with respect to the crystal axis system.

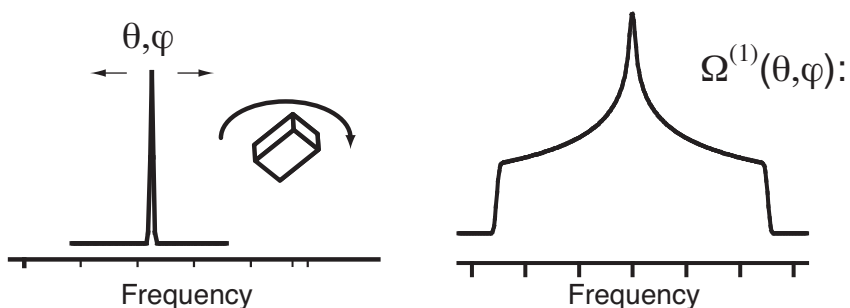


Figure 1.1: Typical NMR spectrum of a single crystal with single site (left). Typical NMR spectrum of a powder sample (right). (Adapted from Philip Grandinetti's NMR course note with permission.)

If the single crystal is crushed up into fine powder, the NMR lineshape becomes a broad powder pattern because all possible crystalline orientations are present (all possible θ and ϕ value on a sphere). This broad powder pattern is an envelope of many narrow peaks observed for each possible crystallite orientation as shown in Figure 1.1.

1.2.6 Magic Angle Spinning

While the powder pattern lineshape can provide plenty of information, most samples of interest contain multiple sites each with their own powder patterns. More often the powder patterns of all sites are overlapping, so we typically get an NMR spectrum that is virtually impossible to analyze.

Anisotropic interactions need to be removed for obtaining high resolution site resolved isotropic spectrum. In an isotropic liquid sample, tumbling motion of molecules removes anisotropic interactions and we get isotropic spectrum. One way to remove anisotropic interactions is to mimic the tumbling motions of the molecules in liquid. However, this is still the hard way to solve this problem. Fortunately, there is a more efficient way of accomplishing the same result.

Lets look at the NMR transition frequencies. Total NMR transition frequency between $i \rightarrow j$ can be written as a sum of different first order contributions (assuming no second order corrections are present) as

$$\Omega^{(1)} = -\omega_0 \sigma_{iso} [\mathbf{S}^{\{\sigma\}} \cdot \mathbf{p}_I] - \omega_0 \zeta_\sigma [\mathbf{D}^{\{\sigma\}} \cdot \mathbf{p}_I] + \omega_q [\mathbf{D}^{\{q\}} \cdot \mathbf{d}_I] + [\mathbf{D}^{\{d_{IS}\}} \cdot \mathbf{p}_I \mathbf{p}_S], \quad (1.2.64)$$

where \mathbf{S} , and \mathbf{D} represent the spatial part of the transition frequencies, written as

$$\mathbf{S} \propto \mathcal{P}_0(\cos \theta) R''_{0,0}, \quad (1.2.65)$$

$$\mathbf{P} \propto \mathcal{P}_1(\cos \theta) R''_{1,0}, \quad (1.2.66)$$

$$\mathbf{D} \propto \mathcal{P}_2(\cos \theta) R''_{2,0}, \quad (1.2.67)$$

$$(1.2.68)$$

where θ is the angle between the rotor axis and static magnetic field. In typical NMR experiments, the spatial part is manipulated by sample spinning, or by reorienting the sample with respect to the magnetic field. If a sample is spun at angle

$\theta = 54.74^\circ$ (Magic Angle Spinning (MAS) [6, 7]) with respect to the external static magnetic field, we can show that $\mathcal{P}_2(\cos \theta) = 0$, which removes all \mathbf{D} terms in the Equation 1.2.64, leaving only isotropic frequencies. MAS removes all second rank orientation dependences.

Under sample rotation, the inhomogeneous lineshape breaks up into a set of spinning sidebands centered about a centerband lineshape and spaced at integer multiples of the spinning frequency. As the spinning frequency is increased the intensities of the spinning sidebands are reduced and transferred into the centerband. In the limit of infinite spinning speed only the centerband frequency remains. Figure 1.2 shows a simulation of the effect of varying the angle (θ) of the spinning axis with respect to the external magnetic field. The lineshape scales as a function of rotor angle θ by a scaling factor of $P_2(\cos \theta)$. Figure 1.3 shows the effect of finite spinning speed in a series of simulations at different spinning speeds.

1.3 Overview of Thesis

Throughout this thesis, I will discuss some advancements we made in the field of solid state NMR during my PhD period. The second chapter of my thesis describes a new way of obtaining high resolution spectra in a lipid cubic phase. The third chapter describes a data processing method and an optimization method for Carr-Purcell -Meiboom-Gill (CPMG) technique used for sensitivity enhancement in the solid state NMR. The fourth chapter describes a sensitive way to quantify $Q^{(n)}$ species distributions in natural abundance (natural abundance of ^{29}Si is 4.6 %) silicate glass by ^{29}Si NMR. The fifth chapter describes a new way of separating quadrupolar and chemical shift interactions using a two-dimensional NMR approach.

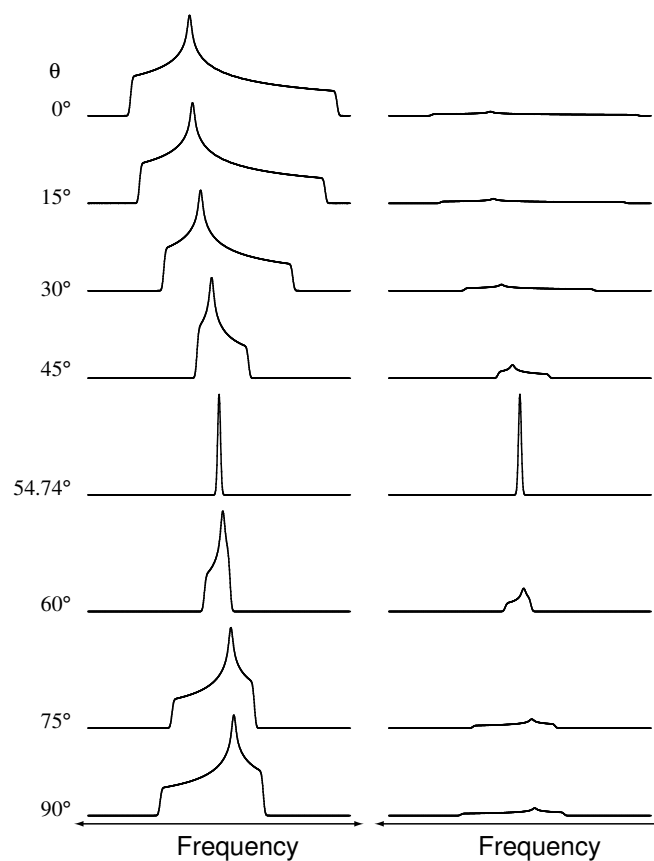


Figure 1.2: Simulated solid-state NMR lineshapes for a spin-1/2 nucleus with a given chemical shift anisotropy as a function of rotor angle. On the left all spectra are normalized to have the same maximum intensity. On the right all spectra are normalized to have the same area. (Adapted from Philip Grandinetti's NMR course note with permission.)

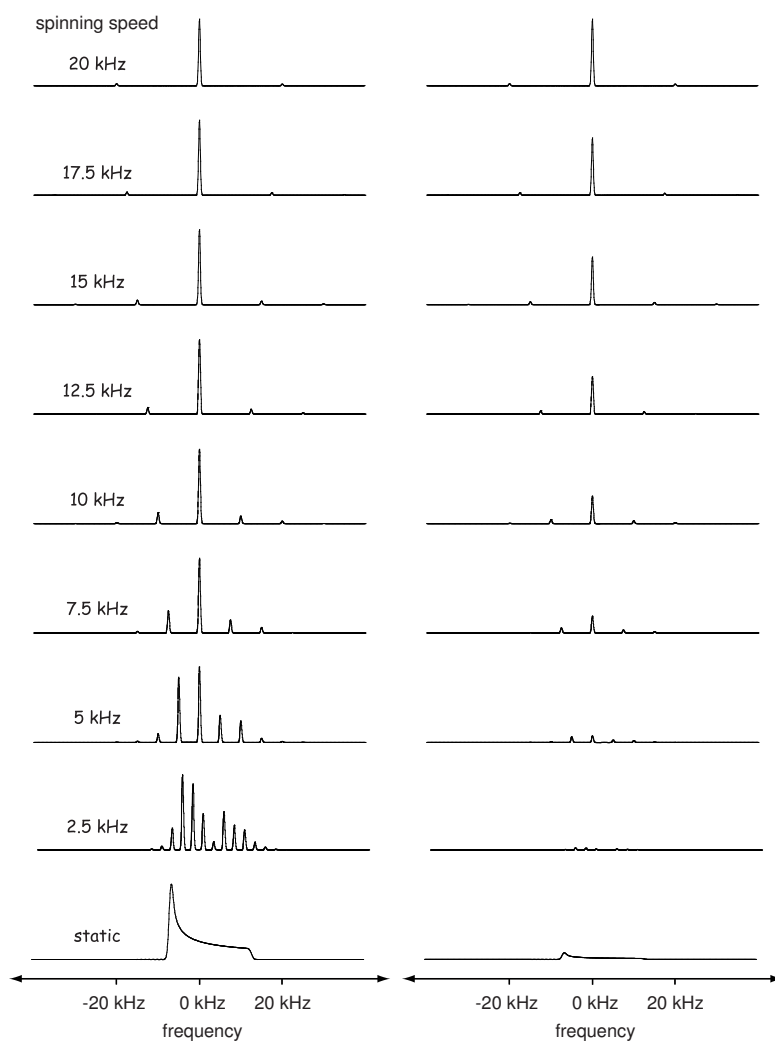


Figure 1.3: Simulated solid-state magic angle spinning NMR spectrum for a spin- $1/2$ nucleus with a given chemical shift anisotropy as function of MAS spinning speed. On the left hand all spectra are normalized to have the same maximum intensity. On the right all spectra are normalized to have the same area. (Adapted from Philip Grandinetti's NMR course note with permission.)

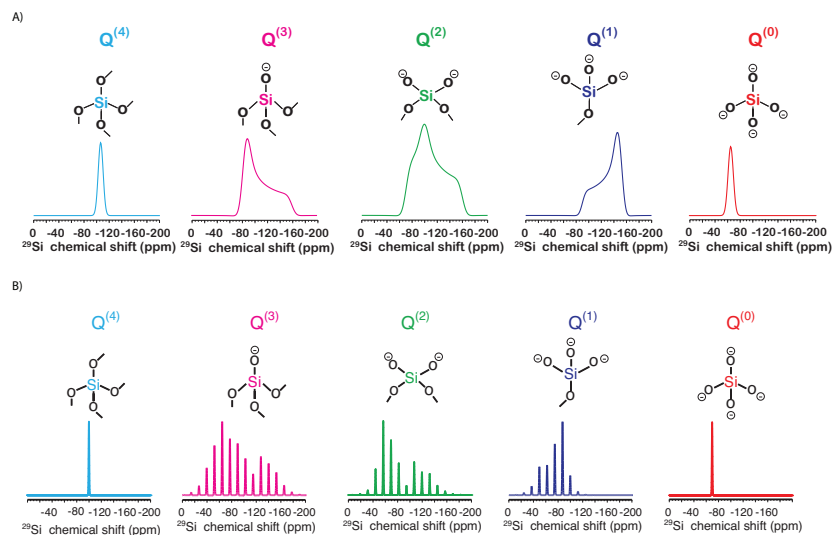


Figure 1.4: (A) Static spectra of different Q^n species. (B) MAS spectra of different Q^n species with spinning speed of 1 kHz. (Adapted from Samantha Vicker thesis and P.Zhang, C. Dunlap, P. Florian, P. J. Grandinetti, I. Farnan, and J. F. Stebbins, *J. Non. Cryst., Solids.* 204, 294, 1996)

CHAPTER 2

HIGH-RESOLUTION ^1H NMR OF A LIPID CUBIC PHASE USING A SOLUTION NMR PROBE

2.1 Introduction

Hydrated lipids can exist in a variety of liquid crystalline or mesophases depending on temperature and sample composition (Figure 2.1). One of these, the lamellar phase (Figure 2.1B), has long and successfully been used as a model for the lipid component of the biological membrane. A second liquid crystalline phase, the cubic phase, has gained notoriety as a host for membrane protein crystallization by the so-called *in meso* method [16, 17]. It has also been used in controlled release and uptake studies [18, 19] and is of interest as an intermediate in membrane fusion and fat digestion [20]. The lipid component of the bicontinuous cubic phase takes the form of a highly curved, continuous bilayer that permeates three-dimensional space as a set of connected saddle sections. The bilayer divides the aqueous component into two branched networks of channels. The channels interpenetrate but never contact one another because of the intervening bilayer (Fig. 2.1C and 2.1D). The midplane of the bilayered membrane describes a periodic minimal surface where mean curvature is everywhere zero [21, 22].

An intriguing aspect of the highly viscous cubic phase is its NMR spectrum, which, unlike the lamellar phase, does not exhibit anisotropic broadening. Molecules

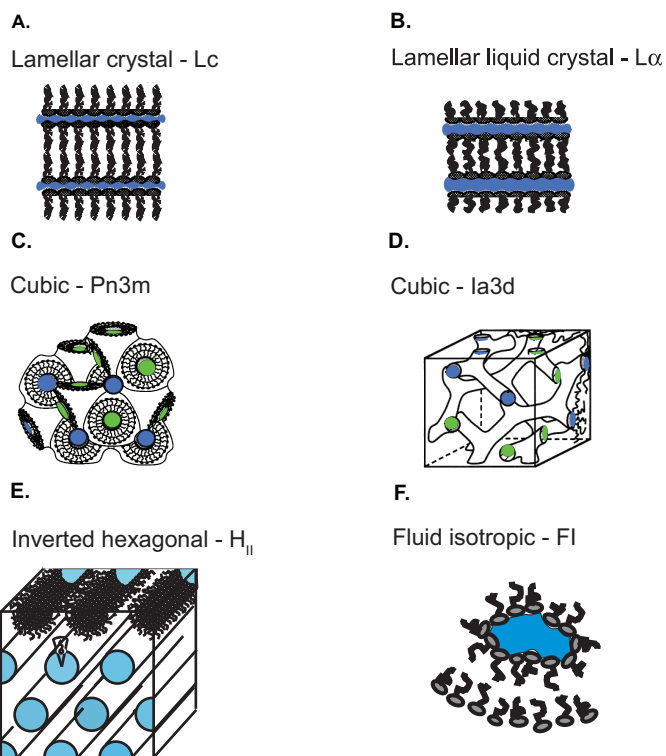


Figure 2.1: Cartoon representation of the various mesophases formed by monoolein and water. Individual lipids are shown as lollipop figures with the pop and stick parts representing the polar head groups and the apolar acyl chain, respectively. The colored regions represent water.

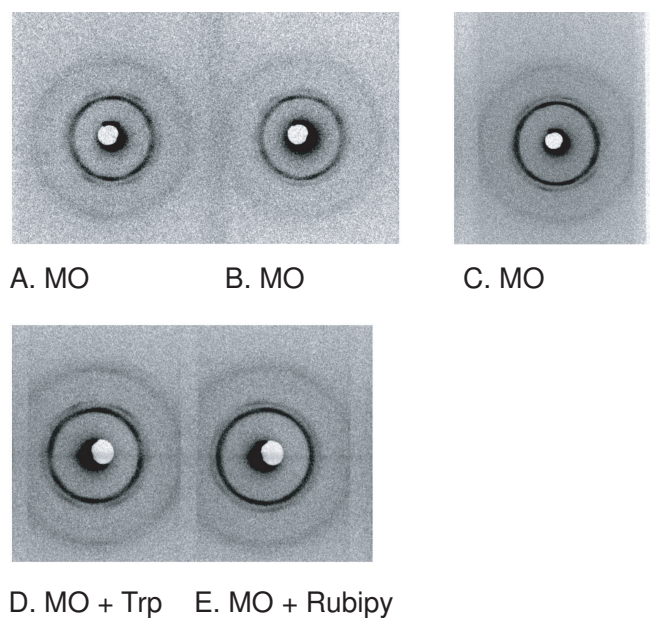


Figure 2.2: Small-angle X-ray diffraction patterns of monoolein/water samples in the cubic-Ia3d phase recorded at 20 °C. Samples were prepared at 37 % (w/w) hydration without additive (A, B, C), and with tryptophan (D) and rubipy (E) as described under Methods. Measurements were made on fresh samples (A, B, D, E) and on a sample that was 2 months old (C). The lattice parameters for the different samples are 149 Å (A, B), 127 Å (C), 148 Å (D) and 146 Å (E).

laterally diffusing parallel to its periodic minimal surface [22] reorient with a symmetry [23] that eliminates second rank NMR frequency anisotropies such as chemical shift anisotropy and hetero- and homonuclear dipolar couplings. It has long been known that ^{13}C and ^{31}P NMR spectra of the cubic phase exhibit narrow, resolved peaks [24–26]. More recently, it has been shown [27–30] that the cubic phase eliminates strong homonuclear proton dipolar couplings and that high resolution ^1H NMR spectra can be obtained with magic-angle spinning (HR-MAS) [27], which further removes the residual spectral broadening that arises from bulk magnetic susceptibility variations. These susceptibility variations arise because the highly viscous nature of the cubic phase makes it difficult to load sample containers, such as conventional solution-state NMR tubes, without introducing air bubbles and other inhomogeneities.

Here, we show that high resolution ^1H NMR spectra with resolved J-coupling multiplets can be obtained using a conventional liquid state NMR probe, without HR-MAS, by loading uniform and homogenous samples of the high viscosity cubic phase into thin-walled glass capillaries. Not only does this approach make high resolution NMR studies in the cubic phase more accessible it also avoids potential sample heating effects of MAS, permits more precise temperature control and enables both X-ray diffraction and NMR spectroscopic measurements to be performed on the same sample. Additionally, we examine the ^1H NMR spectra of two molecules, L-tryptophan and ruthenium-tris(2,2-bipyridyl) dichloride (rubipy), with varying diffusional release rates from the cubic phase to assess potential differences in the interaction of these molecules with the lipid component of the bilayer.

2.2 Materials and Methods

2.2.1 Materials

Monoolein was purchased from Nu Chek Prep. Inc. (Elysian, MN). 99.96% D₂O was obtained from Cambridge Isotope Labs (Andover, MA). Syringes were from Fisher Scientific (Hamilton 81030, 100 μ L gas-tight). Water, with a resistivity of > 18 M Ω -cm, was purified by a Milli-Q Reagent Water System, (Millipore Corporation, Bedford, MA) containing a carbon filter cartridge, two ion-exchange filter cartridges, an organic removal cartridge and a final 0.2 μ m filter (Sterile Millipore millipak 40, lot F2PN84024). Rubipy was kindly provided by Dr. Claudia Turro (The Ohio State University). 2,2-Dimethyl-2-silapentane-5-sulfonate sodium salt (DSS) was purchased from Aldrich (St. Louis, MO; lot#17216EB). L-tryptophan (lot#119HO3-LL) was from Sigma (St. Louis, MO).

2.2.2 Sample Preparation

Samples of fixed hydration were prepared by mechanical mixing of appropriate amounts of lipid and aqueous solution to achieve the desired overall sample composition of 63 %(w/w) lipid. Homogenization was accomplished at room temperature (20-22 $^{\circ}$ C) by cycling the lipid/aqueous mixture at least 60 times between two 100 μ L microsyringes (Hamilton Company, Reno, NV) through a short (6 mm) 22-gauge coupling needle, as described [31]. The homogenized material was loaded into 3 cm long, 1.0 mm diameter (0.01 mm wall thickness) glass capillaries (Charles Supper Natick, MA). Transfer with minimal water loss was accomplished by uncoupling the lipid mixer and attaching a standard 22-gauge needle to the syringe containing the sample. This was used to place the mesophase in the capillary. Particular care was

taken to withdraw the capillary from the tip of the syringe needle during the filling process to ensure uniform, bubble-free loading. This procedure avoids the need for prolonged high-speed centrifugation. Capillaries were flame sealed (Model 6, Microflame, Inc., Minnetonka, MN), glued with 5 min epoxy (Hardman Inc., Belleville, NJ) and stored for up to 7 days at room temperature prior to data collection. Incorporation of L-tryptophan or rubipy into the cubic phase was achieved by using a solution of the corresponding additive in water or D₂O to hydrate the lipid in the initial mixing process. The solution concentrations of additives were tryptophan, 8 mg/mL; and rubipy, 10 mg/mL. Final molar ratios of additive to lipid in the cubic phase samples were: tryptophan, 1:122; and rubipy, 1:166.

2.2.3 X-ray Diffraction

Phase identity and microstructure of the sample was determined by small-angle X-ray diffraction (SAXS) using point focused Cu-K_α X-rays (1.542 Å, nickel (0.025 mm-thick) filtered) produced using a two-beam port Rigaku RU-300 18 kW rotating anode generator (Rigaku USA, Inc., Danvers, MA) operated at 40 kV and 200 mA. Static diffraction patterns were collected at 20 °C. Exposure times were 30-60 min at a sample-to-detector distance of 24-34 cm. Samples were examined under cross-polarized light with a Nikon Eclipse E400 microscope at 10× and 40× magnification to confirm that the region of interest within the capillary was uniformly in the cubic phase.

The diffraction measurements show that the samples used in this study were in the cubic-Ia3d phase in agreement with the known phase behavior of monoolein at 20 °C (see Fig. 1 in reference [32]). The lattice parameter of the mesophase ranged from 127 to 150 Å over the course of the study. This variation is due primarily to slight differences in the water content of the samples, which have a nominal value of

37 % (w/w). When additives were included in the sample, SAXS was used to evaluate the phase state of the system and to monitor phase stability during the course of the investigation. In all cases, the cubic-Ia3d or cubic-Pn3m phase were obtained (see Figure 2.2).

2.2.4 NMR

High resolution ^1H NMR spectra were collected at 20 ± 0.2 °C on a Bruker DMX 600 MHz NMR spectrometer using a 5 mm triple resonance TXI probe with *xyz* gradients (Bruker). One or more X-ray capillaries containing the lipid sample were placed in a standard 5 mm thin-walled NMR tube (Wilmad Buena, NJ) containing D_2O (99.96%). Spectra were collected with and without spinning. Shimming typically took less than twenty minutes for the initial sample, and under 5 min for subsequent samples. ^1H spectra were collected with one pulse acquisition or WATERGATE solvent suppression [33, 34].

2.3 Results and Discussion

A critical first step in nearly all NMR studies is obtaining spectral resolution. With sufficient resolution resonances can be assigned, usually by exploiting isotropic chemical shifts and *J*-couplings. Once assignments are complete, dipolar couplings can be measured, often through cross-relaxation studies [35, 36], and used to determine the presence of secondary and higher order structures. As mentioned in the Introduction, the lateral diffusion of molecules within the lipid bilayer of the cubic phase averages away all second rank NMR frequency anisotropies, resulting in high resolution spectra. Pampel and coworkers [27] had further shown that higher resolution ^1H NMR spectra of the monoolein cubic phase can be obtained using HR-MAS to remove the residual line broadenings from magnetic susceptibility variations. In Fig. 2.3 we show

that the need for HR-MAS can be eliminated and that equivalent resolution can be obtained for the ^1H NMR spectrum of the cubic-Ia3d phase when the sample is carefully loaded in thin-walled glass capillaries. The 600 MHz ^1H NMR spectrum in Fig. 2.3 was obtained with 25 mg lipidic mesophase using a standard solution probe at 20 °C. Resonance assignments in this one-dimensional ^1H spectrum are given in Table 2.1. Because monoolein has a tendency to isomerize in aqueous dispersion producing an equilibrium mix of the 1- and 2-isomers (88% 1-monoolein and 12% 2-monoolein at 20 ° C [37]),

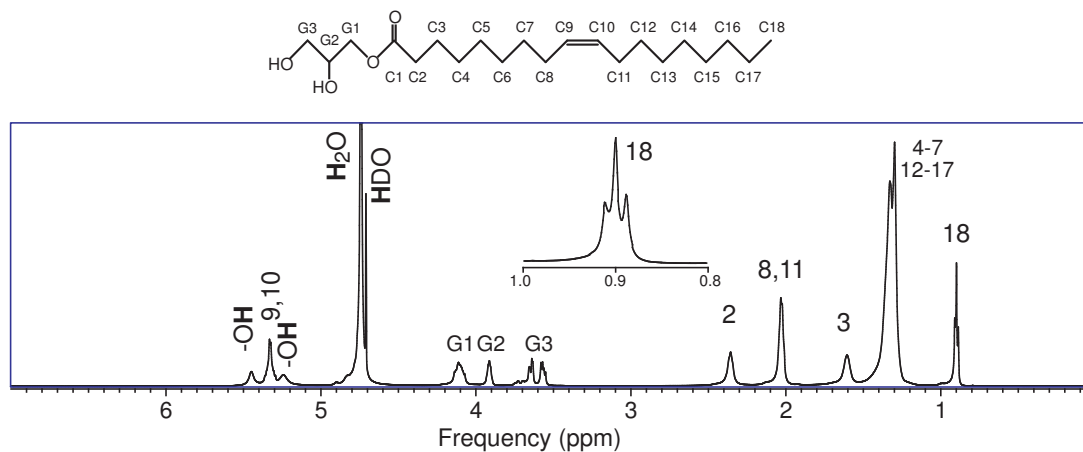


Figure 2.3: ^1H NMR spectrum of the cubic-Ia3d phase formed by monoolein at 37 % (w/w) water in a glass X-ray capillary. Data were collected on a 600 MHz spectrometer (8 KHz spectral width, 32k points, 128 acquisitions) at 20 °C without spinning. The spectrum was processed without apodization. The X-ray diffraction pattern of this sample is shown in Fig. 2.2C. The molecular structure of monoolein and the labeling used to identify resonances are shown at the top of the figure. A small amount of 2-monoolein is also present due to isomerization of 1-monoolein (see text). It gives rise to the additional resonances near 3.7 ppm.

Shown in Fig. 2.5 is a comparison of the ^1H NMR spectra of rubipy in aqueous solution and incorporated into the cubic phase at a 1:166 mol ratio. The ^1H NMR shift frequencies of rubipy are summarized in Table 2.2. Notice that there is a systematic average shift of $\sim 0.120 \pm 0.020$ ppm in all resonances. Additionally, there is a uniform 2-3 Hz increase in linewidth upon incorporation into the cubic mesophase, which likely arises from residual bulk magnetic susceptibility variations in the sample. Generally, there are two contributions to the observed NMR shift: (i) the bulk magnetic susceptibility of the phase, which causes a systematic average shift of all the protons on a molecule in that phase [11] and (ii) the local susceptibility, *i.e.*, the chemical shift, which is sensitive to changes in the local environment. While the absolute NMR shift of the rubipy resonances are different in bulk water and cubic phase, the NMR (chemical shift) difference between each proton resonance is essentially the same in water as it is in the cubic phase. This indicates that changes in the NMR shift arise primarily from bulk susceptibility changes and not as a result of differential specific molecular-level interactions. This is consistent with release studies [19] which show that rubipy remains in the aqueous channel of cubic phase and that it does not partition at or interact with the interface.

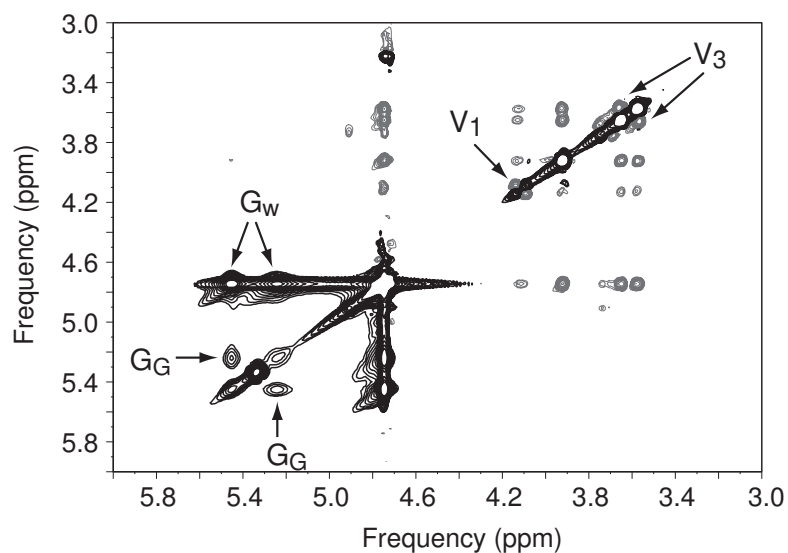


Figure 2.4: Expanded view of the ^1H - ^1H t-ROESY spectrum of the cubic-Ia3d phase recorded using monoolein at 37 % (w/w) hydration in a glass capillary. Data were recorded on a 600 MHz spectrometer under the following conditions: pulse sequence, roesyph; sweep width, $1\text{k} \times 512$ points; 16 dummy scans; 8 acquisitions; 400 msec mixing time; 2500 Hz spin-lock field; 100 μsec $\pi/2$ pulse. The spectrum reveals NOE crosspeaks between the vicinal hydrogens of the glycerol 1 and 3 -CH₂ groups, V₁ and V₃, respectively, and chemical exchange crosspeaks between the hydroxyl groups of glycerol, G_G, and between glycerol's hydroxyls and water, G_W.

In Fig. 2.6 is a comparison of the ^1H NMR spectra of the indole region of L-tryptophan in aqueous solution and incorporated into the cubic phase at a 1:122 mol ratio. The ^1H NMR shift frequencies are summarized in Table 2.3. As with rubipy, both a change in absolute NMR shift and linewidth of L-tryptophan resonances is observed. In contrast to rubipy, however, there are significant changes in the chemical shift differences amongst protons in L-tryptophan upon changing from bulk water to the cubic phase. That is, the differences in NMR shifts of L-tryptophan arise as a result of both bulk susceptibility changes and differential specific molecular-level interactions. Although we cannot cleanly separate the sources behind the shift differences of L-tryptophan, we can use rubipy as a control for the average shift difference due to bulk susceptibility differences of the two phases. Subtracting the average $\Delta\delta$ for rubipy of 0.12 ± 0.02 ppm, we obtain the adjusted $\Delta\delta'$ values for each L-tryptophan site also given in Table 2.3. Generally, an upfield, or positive chemical shift difference is associated with exposure to a more polar or solvated environment [39,40]. Conversely, a negative chemical shift change results from movement towards a less polar or less solvated environment. The large negative chemical shift changes observed at sites 4, 5, and 6 when L-tryptophan is incorporated into the cubic phase is consistent with L-tryptophan being partially inserted into the bilayer interface and shielded from water [40].

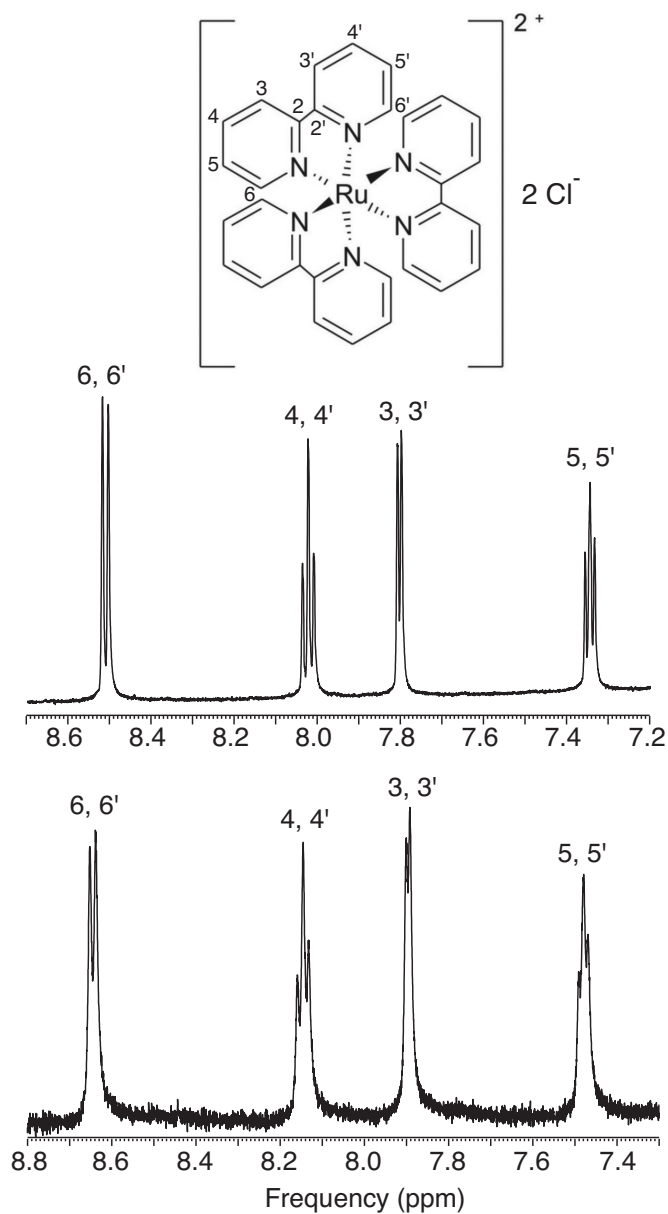


Figure 2.5: ^1H NMR spectra of rubipy in bulk aqueous solution (upper panel) and incorporated into the cubic-Ia3d phase of monoolein at 37 % (w/w) hydration (lower panel). Spectra were processed without apodization and were externally referenced to DSS. The concentration of rubipy in the aqueous solution was 10 mg/mL. The molecular structure of and proton identities in rubipy are shown in the upper panel. Individual resonances in the two spectra are labeled according to the molecular structure.

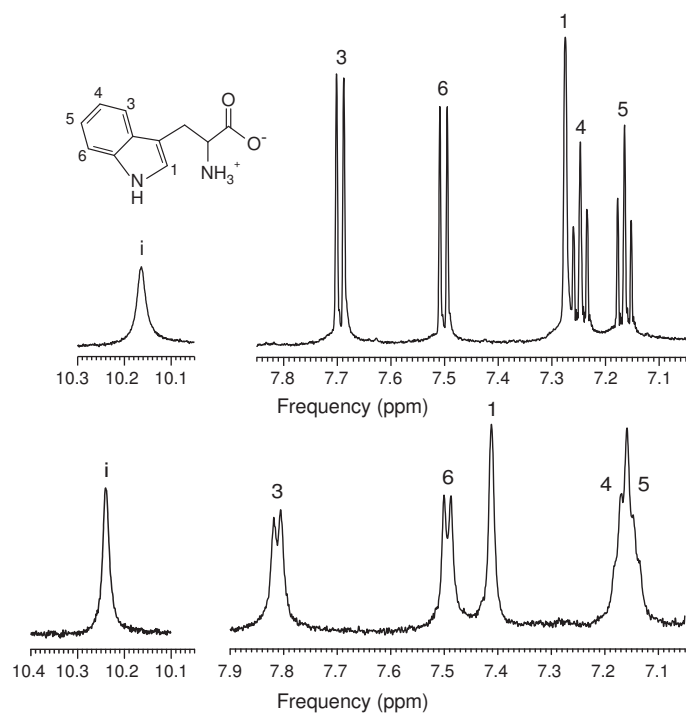


Figure 2.6: Downfield region of the ^1H NMR spectra of L-tryptophan in bulk aqueous solution (upper panel) and in the cubic-Ia3d phase of monoolein at 37 % (w/w) water (lower panel). Spectra were processed without apodization and externally referenced to DSS. The concentration of tryptophan in the aqueous solution was 8 mg/mL.

Additionally, we note that the linewidth of the indole ring resonances increased by 3-6 Hz in the cubic phase compared to bulk aqueous solution, except in the case of the -NH proton (peak *i* in Fig. 2.6), where the linewidth decreased by almost 5 Hz. Generally, the indole-NH proton linewidth in bulk water is broadened, compared to the other proton resonances in L-tryptophan, due to proton exchange with water [41]. The decrease in the indole-NH proton resonance in going from bulk to mesophase implies a decrease in this exchange rate. Such a decrease could arise from an increased micro-viscosity of water in the channels of the cubic phase, or from L-tryptophan having more specific interactions with the bilayer interface, or both. Further work is needed to distinguish between these possibilities. Overall, our results are in agreement with separate transport and spectroscopic studies performed on the cubic phase [18, 19, 42, 43]; and with current studies of L-tryptophan analogs in the interfacial region of phospholipid bilayers [44, 45].

2.4 Conclusion

We have shown that high resolution ^1H NMR spectra with resolved J-coupling multiplets of the cubic phase of monoolein can be obtained using a conventional liquid state NMR probe and without HR-MAS, by carefully loading uniform and homogeneous samples of the high viscosity cubic phase into thin-walled glass capillaries. Additionally, we have illustrated with L-tryptophan and rubipy that the kind of high resolution NMR spectra attainable in the cubic phase can be a useful tool to probe specific molecular interactions of additive molecules with lipid bilayers. Overall, the combination of the cubic phase and NMR could provide a valuable complement to other NMR approaches, such as oriented lipid bilayers on glass slides [46, 47], MAS applied to multilamellar vesicles [48–50], or bicelles [51], for investigating structure and dynamics in model membrane systems.

Hydrogen	ppm	splitting	J_{HH} (Hz)
-(CH ₃)	0.900	triplet	6.7
-(CH ₂) _{<i>n</i>} -	1.298 1.328		
- CH ₂ - CH ₂ COO-	1.605		
- CH ₂ CH=CH	2.012 2.023 2.033 2.043		
- CH ₂ COO-	2.356	triplet	6.8
- HC = CH -	5.329		
1-MO:G3 - HCH -	3.557 3.576	doublet doublet	6.2 6.5
1-MO:G3 - HCH -	3.678 3.698	doublet doublet	5.7 4.5
1-MO:G2 - CH -	3.914	quintet	4.7
1-MO:G1 - CH ₂ -	4.112		
1-MO:G1 and G2 - OH	5.243 5.449		
HDO in outer tube	4.710		
H ₂ O in cubic phase	4.742		

Table 2.1: Proton chemical shift assignments and scalar J (indirect dipolar) couplings for resonances from monoolein in the lipidic cubic-Ia3d phase referenced to the terminal methyl of the oleoyl chain at 0.900 ppm.

		aqueous phase		cubic phase		
site	splitting	δ_w/ppm	J/Hz	δ_{cp}/ppm	J/Hz	$\Delta\delta/\text{ppm}$
3,3'	doublet	7.805	5.81	7.897	5.57	0.092
4,4'	triplet	8.024	8.37	8.146	8.31	0.122
5,5'	triplet	7.346	7.06	7.479	6.86	0.133
6,6'	doublet	8.512	8.67	8.645	8.64	0.133

Table 2.2: NMR shift frequencies in ppm and scalar J (indirect dipolar) couplings of rubipy in aqueous solution and incorporated in the cubic phase. The shift difference is calculated according to $\Delta\delta = \delta_{cp} - \delta_w$. Site refers to proton location in rubipy as defined in the molecular structure shown in Figure 2.5.

site	splitting	aqueous phase		cubic phase		$\Delta\delta/\text{ppm}$	$\Delta\delta'/\text{ppm}$
		δ_w/ppm	J/Hz	δ_{cp}/ppm	J/Hz		
i	singlet	10.168	-	10.240	-	0.072	-0.048
1	singlet	7.278	-	7.412	-	0.134	0.014
3	doublet	7.698	8.16	7.812	8.21	0.114	-0.006
4	triplet	7.250	7.63	7.159	7.45	-0.091	-0.211
5	triplet	7.167	7.58	7.159	7.45	-0.008	-0.128
6	doublet	7.505	8.25	7.495	7.85	-0.010	-0.130

Table 2.3: NMR shift frequencies in ppm and scalar J (indirect dipolar) couplings of L-tryptophan in aqueous solution and incorporated in the cubic phase. The shift differences are calculated according to $\Delta\delta = \delta_{cp} - \delta_w$ and $\Delta\delta' = \Delta\delta - \langle\Delta\delta\rangle_{rubipy}$ where $\langle\Delta\delta\rangle_{rubipy} = 0.12 \pm 0.02$ ppm. Site refers to proton location in L-tryptophan as defined in the molecular structure shown in Figure 2.6.

CHAPTER 3

TRADING INFORMATION FOR SENSITIVITY: CPMG ACQUISITION IN SOLIDS

3.1 Introduction

In spite of modern hardware and improved methodologies, the lack of sensitivity in solid state NMR spectroscopy still remains an obstacle to greater widespread adoption. While anisotropic nuclear spin interactions provide a wealth of structural information in solid-state NMR, these same interactions are also responsible for inhomogeneously broadened resonances that cause notoriously low signal-to-noise ratios. Solid-state NMR experiments, such as MAS, manipulate the sample's spatial degrees of freedom to refocus the time domain evolution into a train of rotary echoes. The increase in signal area in the time domain from the multiple echoes leads to a corresponding increase in signal intensity in the frequency domain. A similar effect can be obtained using the CPMG experiment [52, 53] where a train of π pulses, which manipulate the spin degrees of freedom, create a train of Hahn spin echoes [54]. Although the CPMG experiment was originally developed for diffusion and relaxation studies in liquid-state NMR its ability to refocus spin degrees of freedom that are odd order in \hat{I}_z has made it a popular approach for enhancing solid-state NMR sensitivity of anisotropic spectra for both spin-1/2 and the central transition of half integer quadrupolar nuclei in polycrystalline samples [2, 55, 56].

While shorter delays between π pulses in the CPMG experiment can provide higher sensitivity for anisotropic spectra it also results a corresponding information loss about anisotropic interactions, such as the chemical shift anisotropy (CSA) and quadrupolar couplings. In contrast, longer delays between π pulses retain anisotropic coupling information, but the cost is a spectrum with a lower overall sensitivity. This issue has been examined by Lefort et al. [57] in the context of CPMG acquisition and the MQ-MAS experiment. In the Lefort study the optimum range of CPMG π pulse spacings was defined only in terms of minimizing the truncation of the echo signal decay. As shown by Hodgkinson and Emsley [58] in the analogous case of MAS sideband analysis, however, a more appropriate merit function is the uncertainty in the tensor parameters obtained from a least-squares analysis of the sideband (or “spikelet”) pattern. In this work, we have extended the approach of Hodgkinson and Emsley to the case of CPMG acquisition and found that there exists a range of optimum π pulse spacings in the CPMG experiment which yield a minimum uncertainty when extracting the NMR tensor parameters from an anisotropic lineshape. These uncertainties can be strongly dependent on the CPMG π pulse spacing, increasing steeply at short CPMG π pulse spacings and increasing at long spacings particularly when the pre-CPMG signal sensitivity is poor. We have found that the optimum π pulse spacing depends primarily on the span of the anisotropic lineshape, Ω , and generally occurs in a range of values asymmetrically spaced around $\Omega 2\tau \sim 11$, regardless of the interactions contributing to the lineshape. We have also found that as the pre-CPMG sensitivity decreases the most optimum π pulse spacing remains the same while the range of optimum $\Omega 2\tau$ values contracts towards the most optimum value.

Additionally, we demonstrate how TOP processing [3, 59, 60] can also be used to eliminate the sideband (or “spikelet”) pattern lineshape and recover a more familiar lineshape that is easily analyzed with conventional lineshape simulation algorithms.

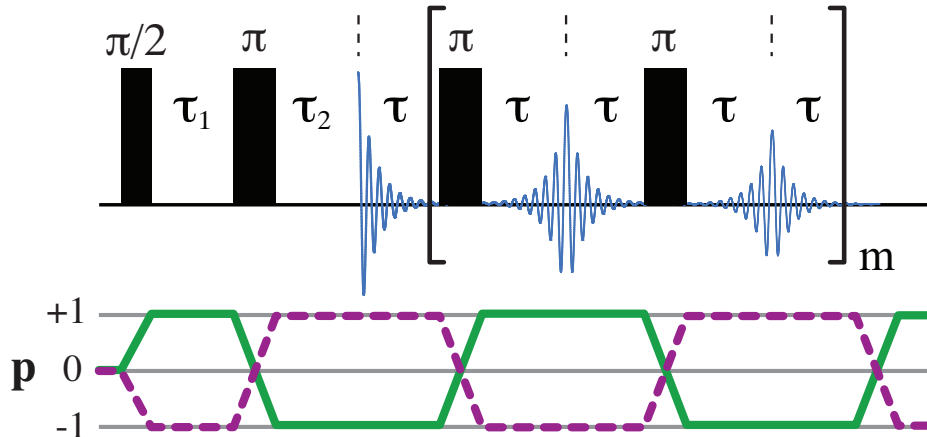


Figure 3.1: CPMG pulse sequence and coherence transfer pathway used in this study.

3.2 Experimental

All experiments were performed on a 9.4 Tesla Bruker DMX 400 spectrometer, using a 4mm MAS probe operating at a ^{207}Pb frequency of 83.51 MHz for polycrystalline $\text{Pb}(\text{NO}_3)_2$ and a ^{87}Rb frequency of 131.07 MHz for polycrystalline RbClO_4 . The CPMG pulse sequence employed is shown in Fig. 3.1. For CPMG-MAS experiments, the π pulses were separated in time by an integer multiple of the rotor period, which was $80 \mu\text{s}$ in all experiments employing sample rotation. Radio frequency power levels were calibrated on the solution of $\text{Pb}(\text{NO}_3)_2$ and RbCl powder for ^{207}Pb and ^{87}Rb , respectively. A 1M $\text{Pb}(\text{NO}_3)_2$ solution and 1M RbNO_3 solution were used for referencing ^{207}Pb and ^{87}Rb resonances, respectively.

In the discussion that follows we employ IUPAC definitions for the nuclear shielding or chemical shift interaction [14]. The isotropic nuclear shielding is defined as the trace of the shielding tensor

$$\sigma_{\text{iso}} = \frac{1}{3}(\sigma_{xx} + \sigma_{yy} + \sigma_{zz}), \quad (3.2.1)$$

where σ_{xx} , σ_{yy} , and σ_{zz} are the components of the nuclear shielding tensor in its principal axis system. The isotropic chemical shift, δ_{iso} , is defined

$$\delta_{\text{iso}} = (\sigma_{\text{ref}} - \sigma_{\text{iso}})/(1 - \sigma_{\text{ref}}), \quad (3.2.2)$$

where σ_{ref} is the isotropic nuclear shielding of a reference compound. We adopt the Haeberlen convention [14], where

$$|\sigma_{zz} - \sigma_{\text{iso}}| > |\sigma_{yy} - \sigma_{\text{iso}}| > |\sigma_{xx} - \sigma_{\text{iso}}|, \quad (3.2.3)$$

the shielding anisotropy, ζ_s , is defined as

$$\zeta_s = \sigma_{zz} - \sigma_{\text{iso}}, \quad (3.2.4)$$

and the shielding asymmetry parameter is defined as

$$\eta_s = \frac{\sigma_{yy} - \sigma_{xx}}{\zeta_s}. \quad (3.2.5)$$

The components of the chemical shift tensor, δ_{ij} , are related to the components of the nuclear shielding according to

$$\delta_{ij} = (\sigma_{\text{ref}} - \sigma_{ij})/(1 - \sigma_{\text{ref}}), \quad (3.2.6)$$

with δ_{33} associated with the lineshape singularity furthest from δ_{iso} , and the principal component δ_{11} associated with the singularity furthest from δ_{33} , and the principal component δ_{22} associated with the singularity in between δ_{33} and δ_{11} .

3.2.1 Span

We find it convenient to define the optimum CPMG π pulse spacing in terms of the span of the anisotropic lineshape, which is defined as the difference between the maximum and minimum frequencies in the lineshape. For a nuclear shielding or chemical shift anisotropic lineshape the span, Ω_s , is defined as

$$\Omega_s = \delta_{33} - \delta_{11} = -\zeta_s (\eta_s + 3)/2. \quad (3.2.7)$$

The central transition MAS spectrum of a half-integer quadrupole nucleus with an anisotropic second-order lineshape will have a span [61] of

$$\Omega_{q,\text{MAS}} = \frac{\nu_q^2}{168\nu_0} \left[I(I+1) - \frac{3}{4} \right] \left(12 + 4\eta_q + \frac{\eta_q^2}{3} \right). \quad (3.2.8)$$

The central transition static spectrum of a half-integer quadrupole nucleus will have an anisotropic second-order lineshape with a span [61] of

$$\Omega_{q,\text{Static}} = \frac{\nu_q^2}{16\nu_0} \left[I(I+1) - \frac{3}{4} \right] \left(\frac{25}{9} + \frac{22\eta_q}{9} + \frac{\eta_q^2}{9} \right). \quad (3.2.9)$$

3.3 TOP processing for CPMG data

As shown by Larsen et al. [2], the Fourier transform of the CPMG echo train yields a sideband or “spikelet” pattern. The information about unrefocused interactions is present in the individual sideband lineshape while information about all interactions resides in the sideband envelope pattern. A problem with the sideband pattern is that any truncation artefacts in the spectrum are not easily discernable. Here we show that a TOP-like approach [3] applied to CPMG data can eliminate the sideband pattern and recover a more familiar lineshape that is easily analyzed with conventional lineshape simulation algorithms.

The decay of a CPMG echo train will arise from homogeneous interactions in addition to any motional processes which interfere with the echo refocusing. Thus, we can write the CPMG time domain signal of a single site as

$$S(t) = s^e(t) \sum_{N=-\infty}^{\infty} A(N) e^{i2\pi Nt/2\tau}, \quad (3.3.1)$$

where 2τ is the distance between the center of the two π pulses, $s^e(t)$ represents the envelope function due to the unrefocused spin interactions and is responsible for the

individual sideband lineshape, and $A(N)$ is the amplitude of its N th sideband given by

$$A(N) = \int_0^{2\tau} e^{-iW(\alpha,\beta,\gamma)(\tau-|t-\tau|)} e^{-i2\pi Nt/2\tau} dt, \quad (3.3.2)$$

where $W(\alpha, \beta, \gamma)$ is the frequency of a crystallite at an Euler angle α , β , and γ between the interaction tensor and the crystal coordinate frame.

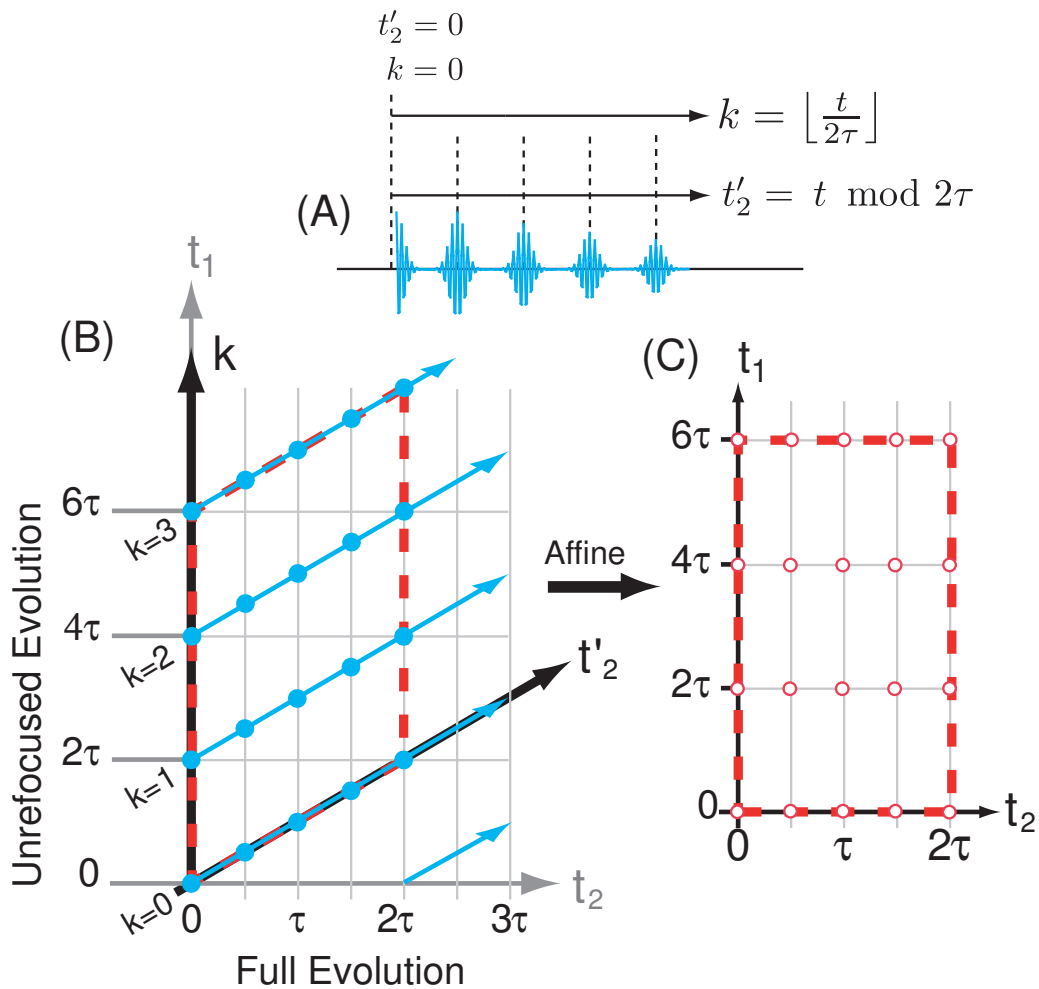


Figure 3.2: (A) CPMG echoes with coordinate definitions and timings. (B) Sampling trajectory (blue lines) of the CPMG data in the 2D $t_1 - t_2$ and $k - t'_2$ coordinate systems. Identical data sets run parallel in the 2D plane and are separated by 2τ in $t_1 - t_2$ coordinate system. (C) Affine transformed 2D data set that correlates t_1 and t_2 .

Following the approach outlined for rotary echoes [3], the 1D time domain signal can be mapped into an intermediate 2D coordinate system with variables k and t'_2 , as shown in Fig. 3.2, by defining

$$t = t'_2 + k 2\tau, \quad (3.3.3)$$

where

$$t'_2 = t \bmod 2\tau, \quad (3.3.4)$$

and k is an integer given by

$$k = \left\lfloor \frac{t}{2\tau} \right\rfloor. \quad (3.3.5)$$

Here $\lfloor x \rfloor$ represents the floor function of x . Using these definitions the 1D CPMG signal can be mapped into the 2D signal in the k - t'_2 coordinate system obtaining

$$S(k, t'_2) = s^e(k, t'_2) \sum_{N=-\infty}^{\infty} A(N) e^{i2\pi N t'_2 / 2\tau}.$$

To this signal we apply the affine transformation

$$\begin{pmatrix} t_1 \\ t_2 \end{pmatrix} = \begin{pmatrix} 2\tau & 1 \\ 0 & 1 \end{pmatrix} \begin{pmatrix} k \\ t'_2 \end{pmatrix}, \quad (3.3.6)$$

and obtain the 2D signal

$$S(t_1, t_2) = s^e(t_1, t_2) \sum_{N=-\infty}^{\infty} A(N) e^{i2\pi N t_2 / 2\tau}. \quad (3.3.7)$$

A 2D Fourier transform of this signal yields a TOP-CPMG 2D spectrum, as shown in Fig. 3.3, which correlates interactions unrefocused by the π pulse train to all interactions. The $\omega_1 = 0$ cross section of the the TOP-CPMG spectrum yields the TOP-CPMG-enhanced 1D spectrum.

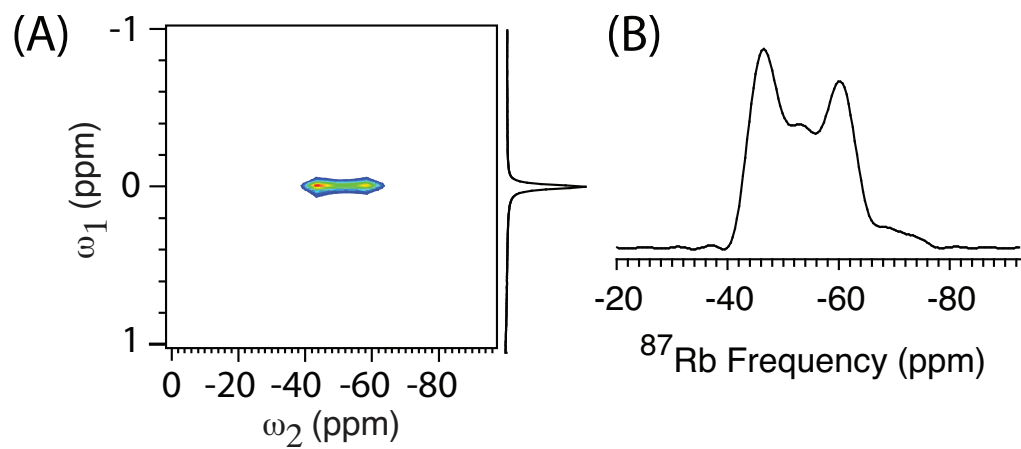


Figure 3.3: (A) ^{87}Rb TOP-CPMG MAS spectrum of RbClO_4 . The ω_1 dimension contains all the unrefocused frequencies and the ω_2 dimension contains all frequencies. The contour level for the 2D contour plot is 20% to 100% with a linear increment of 4.2%, of the the maximum amplitude. (B) The CPMG-enhanced 1D spectrum obtained from the $\omega_1 = 0$ cross-section.

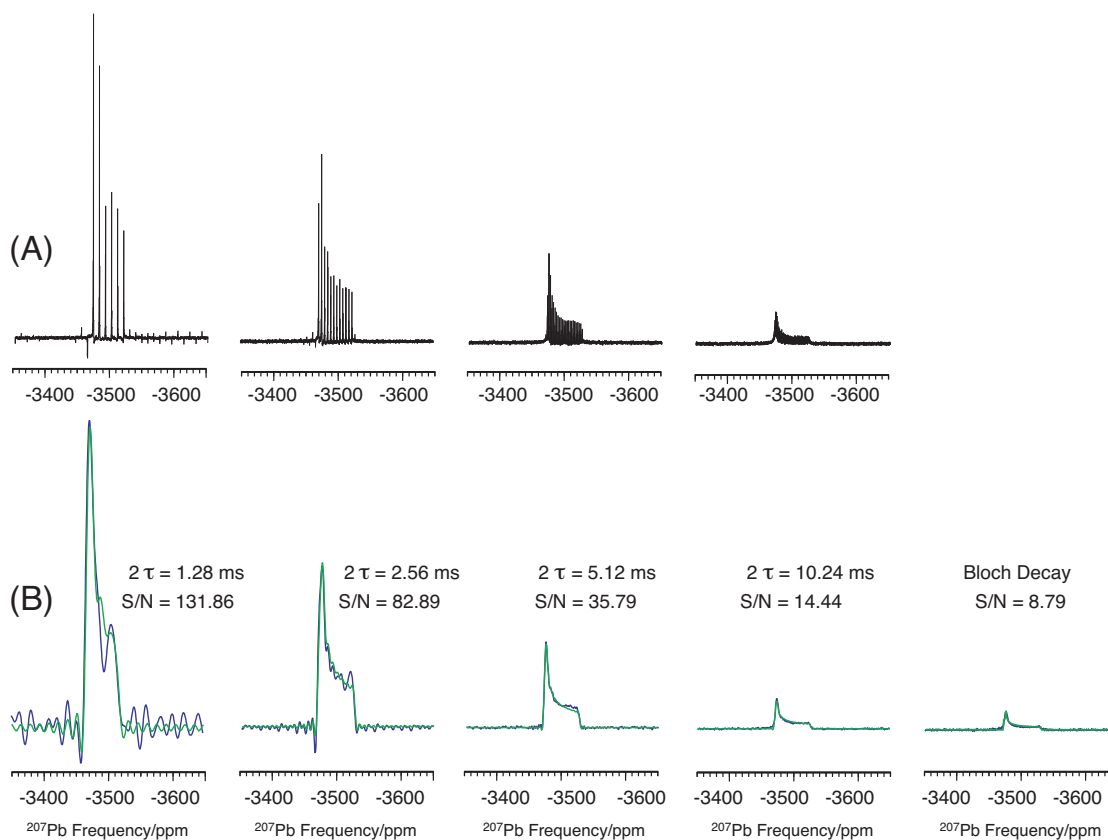


Figure 3.4: The static CPMG experimental spectra of ^{207}Pb resonance in $\text{Pb}(\text{NO}_3)_2$ powder sample as function of π pulse spacing. (A) Processed using "spikelet" approach of Larsen et.al [2]. (B) Processed using modified TOP [3] data processing method. Also shown are the "best-fit" model lineshapes which take signal truncation inside 2τ acquisition window into account.

It is well known that the sensitivity of a spectrum will decrease with increasing acquisition time, unless a proper time-domain matched filter is applied prior to Fourier transform. Similarly, if no apodization is applied to the CPMG data before processing the sensitivity of the sideband or TOP-CPMG spectrum will become dependent on the total CPMG acquisition time. For a CPMG signal the appropriate matched filter is one that matches the envelope function [62], $s^e(t)$, due to the unrefocused spin interactions. The parameters for this envelope function are easily obtained from the lineshape of an individual sideband, or alternatively, the lineshape in the ω_1 projection of the TOP-CPMG 2D spectrum.

3.4 Results and Discussion

3.4.1 First-order Chemical Shift

Using TOP processed CPMG spectra, we have explored the relationship between the CPMG π pulse spacing and the tensor parameter uncertainties extracted from the CPMG-enhanced anisotropic lineshape. This idea is similar to that of Hodgkinson and Emsley [58], who investigated the optimum spinning speed for extracting nuclear shielding anisotropy parameters in a spinning sideband analysis. They found that the minimum uncertainty in extracting the shielding anisotropy, ζ_s occurred when $|\zeta_s|\tau_R \approx 9$, where τ_R is the rotor period. For the shielding asymmetry parameter, η_s , they state “that static spectra always provide a more reliable determination.” We believe, however, that this conclusion may have been incorrectly biased by examining reliability instead of standard deviation, since reliability in the case of η_s becomes ill-defined as η_s goes to zero.

A notable difference between CPMG and MAS is that CPMG refocuses both

isotropic and anisotropic frequencies, whereas MAS refocuses only anisotropic frequencies. Thus, with increasing MAS speed or decreasing CPMG π pulse spacing the uncertainty in nuclear shielding anisotropy parameters, ζ_s and η_s , increases in both methods. In contrast, the uncertainty in the isotropic chemical shift decreases in MAS with decreasing rotor period, but increases in CPMG with decreasing π pulse spacing. Thus, the optimum echo cycle time for extracting the nuclear shielding tensor from a sideband analysis of MAS may not necessarily be the same for CPMG.

The tradeoff between spectral sensitivity and spectral content is well illustrated in Fig. 3.4 with a series of TOP-CPMG spectra of a ^{207}Pb anisotropic nuclear shielding lineshape in static $\text{Pb}(\text{NO}_3)_2$ measured as a function of CPMG π pulse spacing. As expected, with decreasing CPMG π pulse spacing the sensitivity of the spectrum increases by over an order of magnitude compared to the Bloch decay spectrum. For comparison, we also show the sideband (or “spikelet”) spectra obtained with a simple Fourier transform of the CPMG echo train. Note that the distortions due to signal truncation are more easily discernable in the TOP-CPMG spectra than the sideband spectra. As the CPMG π pulse spacing decreases the spectrum becomes a convolution with a sinc function of increasing linewidth. When extracting the nuclear shielding tensor parameters we can include the effect of this signal truncation in the shielding anisotropy lineshape model to improve the least-squares fit. Even with this improvement, however, the information about the shielding tensor is eventually lost as the π pulse spacing decreases and the sinc function lineshape dominates the spectrum. This loss of information about the shielding tensor is best reflected in the changing standard deviation of the principal components of the shielding tensor obtained as a function of CPMG π pulse spacing and shown in Table 3.4. Compared to the Bloch decay the uncertainty of extracted principal components decreases using CPMG with the minimum uncertainty obtained in the least-squares fit of the TOP-CPMG

spectrum with $2\tau = 5.12$ ms. More importantly, note that the principal component uncertainty gets progressively larger with further decrease in π pulse spacing, even though the sensitivity of the TOP-CPMG continues to increase with decreasing π pulse spacing. The values of δ_{11} , δ_{22} , and δ_{33} obtained from the lowest standard deviation fit correspond to $\zeta_s = -36.58$ ppm and $\eta_s = 0.02$, which are in close agreement with values of $\zeta_s = -36$ ppm and $\eta_s = 0$ reported by Neue *et. al* [63]. Small differences in ζ_s and η_s may be attributed to the high sensitivity of the ^{207}Pb shielding tensor to temperature [64].

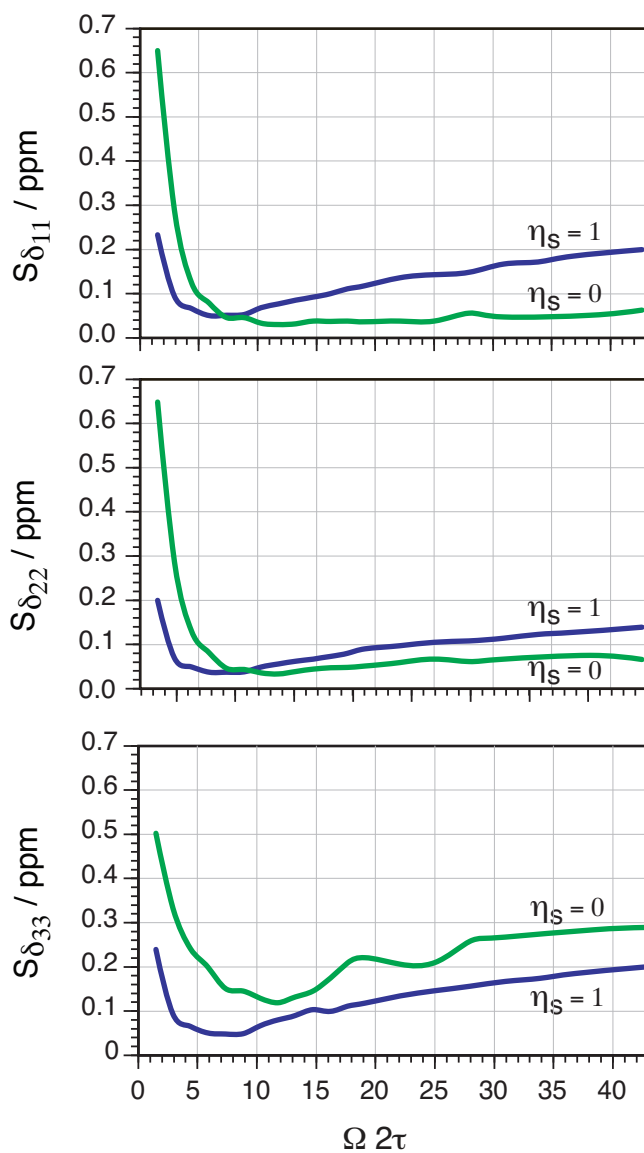


Figure 3.5: Standard deviation of ^{207}Pb chemical shift tensor principal components (δ_{11} , δ_{22} , δ_{33}) extracted from simulated ^{207}Pb resonance CPMG spectra as a function of $\Omega 2\tau$ for different η while keeping span ($\Omega = 4.58$ kHz) and pre-CPMG signal to noise ratio ($S/N=2.30$) constant.

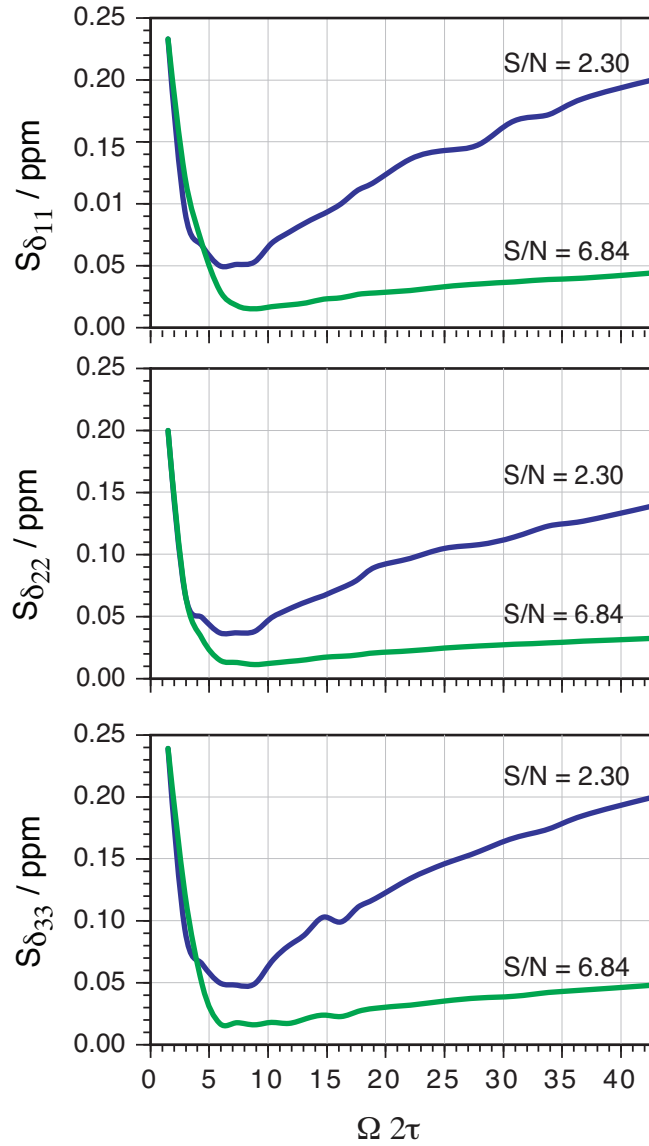


Figure 3.6: Standard deviation of ^{207}Pb chemical shift tensor principal components (δ_{11} , δ_{22} , δ_{33}) extracted from simulated ^{207}Pb resonance CPMG spectra as a function of $\Omega 2\tau$ for different pre-CPMG signal to noise ratios while keeping span ($\Omega = 4.58$ kHz) and asymmetry parameter ($\eta = 1$) constant.

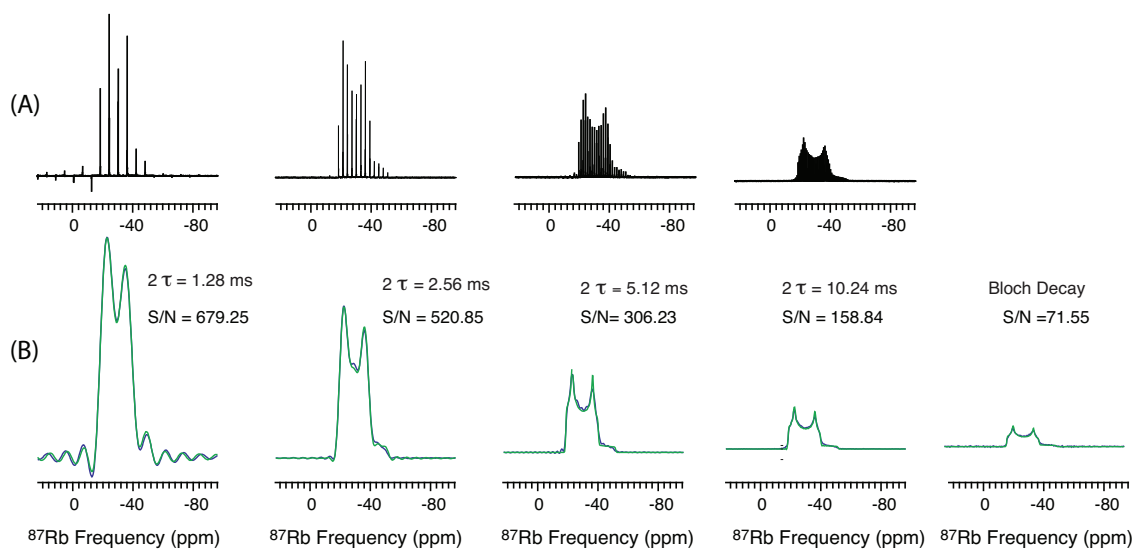


Figure 3.7: The CPMG-MAS experimental spectra of ^{87}Rb resonance in RbClO_4 powder sample as a function of π pulse spacing, which was synchronized to the rotor period of $80 \mu\text{s}$ ($\nu_R = 12.5 \text{ kHz}$). (A) CPMG data processed by "spikelet" approach of Larsen et.al [2]. (B) CPMG data processed by TOP [3] approach. Also shown are the "best-fit" model lineshapes which take signal truncation inside 2τ acquisition window into account.

For a more detailed understanding of how the shielding tensor parameter uncertainties depend on the CPMG π pulse spacing we have simulated TOP-CPMG spectra using different π pulse spacing with constant total acquisition time, constant added noise (pre-CPMG S/N is 2.3), and a constant span of $\Omega = 4.58$ kHz. Least-squares analyses of simulated TOP-CPMG spectra were performed using a shielding lineshape model that takes the 2τ acquisition truncation in account. The standard deviations for the three principal components obtained in this analysis are plotted as a function of $\Omega 2\tau$ in Fig. 3.5 for $\eta_s = 0$ and $\eta_s = 1$ case. The rise in uncertainty of the tensor parameters on the left side of the plots in Fig. 3.5 comes from the signal truncation inside the 2τ acquisition window while the rise in uncertainty on the right side depends on the pre-CPMG signal-to-noise ratio (*vide infra*).

It is not surprising in the $\eta_s \approx 0$ case that the component δ_{33} is more susceptible to noise than δ_{11} and δ_{22} since it is associated with the lowest intensity singularity. For similar reasons both δ_{11} and δ_{33} in the $\eta = 1$ case are more susceptible to noise than δ_{22} , as observed by their higher uncertainties in the high $\Omega 2\tau$ region. The minimum uncertainty occurs at different $\Omega 2\tau$ values for different η_s values, but appear to occur at the same $\Omega 2\tau$ for all three components of shielding tensor with a given η_s . All the standard deviation curves have a relatively shallow minimum, particularly for the δ_{22} component, which is always associated with the singularity of strongest intensity. When reporting the range of optimum $\Omega 2\tau$ values for a given lineshape we report the $\Omega 2\tau$ value with minimum standard deviation and set the left and rightmost limits as the $\Omega 2\tau$ value where the standard deviation reaches a value 50% higher than the minimum. Because of the asymmetry in the standard deviation curves the range limits are not equidistant from the minimum $\Omega 2\tau$ value. Only the smallest range of the three tensor components will be reported. The minimum uncertainties in the

$\eta = 0$ case occur inside a range of $\Omega 2\tau \approx 12_{-1}^{+6}$ and in the case of $\eta = 1$ inside a range of $\Omega 2\tau \approx 9_{-3}^{+3}$.

As noted, the lower bound of the optimum $\Omega 2\tau$ value arises from signal truncation and is fixed for a particular lineshape, independent of the pre-CPMG signal-to-noise ratio. Since the upper bound depends on the pre-CPMG signal-to-noise ratio we have further investigated this dependence by simulating TOP-CPMG spectra with $\eta_s = 1$ and $\Omega = 4.58$ kHz for two different pre-CPMG signal-to-noise ratios as shown in Fig. 3.6. As the pre-CPMG signal-to-noise ratio increases the minima of the standard deviation curves become shallower, causing the upper bound for optimum range of $\Omega 2\tau$ values to increase. As seen in Fig. 3.6, increasing the pre-CPMG signal-to-noise ratio from 2.30 to 6.84 expands the range from $\Omega 2\tau \approx 9_{-3}^{+3}$ to $\Omega 2\tau \approx 9_{-3}^{+7}$. Clearly, further increases in the pre-CPMG sensitivity essentially eliminate the need for CPMG acquisition in reducing uncertainty in tensor parameter determinations. This is consistent with conventional wisdom that the biggest gains with CPMG acquisition come when the pre-CPMG signal suffers from poor sensitivity. Conversely, as the sensitivity decreases the minima of the standard deviation curves become deeper and the range of optimum $\Omega 2\tau$ values decrease. In the light of this insight, it may be worthwhile to extend the work of Hodgkinson and Emsley [58] to consider the effects of static sample signal sensitivity in determining the optimum range of MAS sidebands for extracting CSA tensor parameters.

3.4.2 Second-Order Quadrupolar Coupling

The central transition (CT) of half-integer spin nuclei is unaffected to first-order by the quadrupole coupling and for sizable quadrupole coupling constants experiences a second-order anisotropic frequency contribution that is not completely removed by MAS. The sensitivity of the CT spectrum of half-integer quadrupole nuclei under both

static and MAS can be significantly enhanced with CPMG, so we have examined the optimum CPMG π pulse spacing for measuring both nuclear shielding and quadrupole coupling tensor parameters.

Since the nuclear shielding anisotropy is completely removed by fast MAS the quadrupole coupling constant C_q and asymmetry parameter, η_q , can be readily determined from a least-squares analysis of the high speed CT MAS spectrum. These parameters, in turn, can be used as constraints in a least-squares analysis of the static sample CT spectrum to obtain the shielding tensor parameters and the relative orientation between the quadrupole and shielding tensors. In the case of RbClO_4 , however, the ^{87}Rb quadrupole coupling constant is temperature dependent [65, 66], and frictional heating from the sample spinning is known [66] to reduce the value of ^{87}Rb quadrupole coupling constant in RbClO_4 . Thus, without careful temperature control during MAS, systematic errors in the nuclear shielding tensor parameters could be introduced if the C_q and η_q values obtained from MAS fit were used to constrain the fit of the CT spectrum of a static RbClO_4 sample at room temperature.

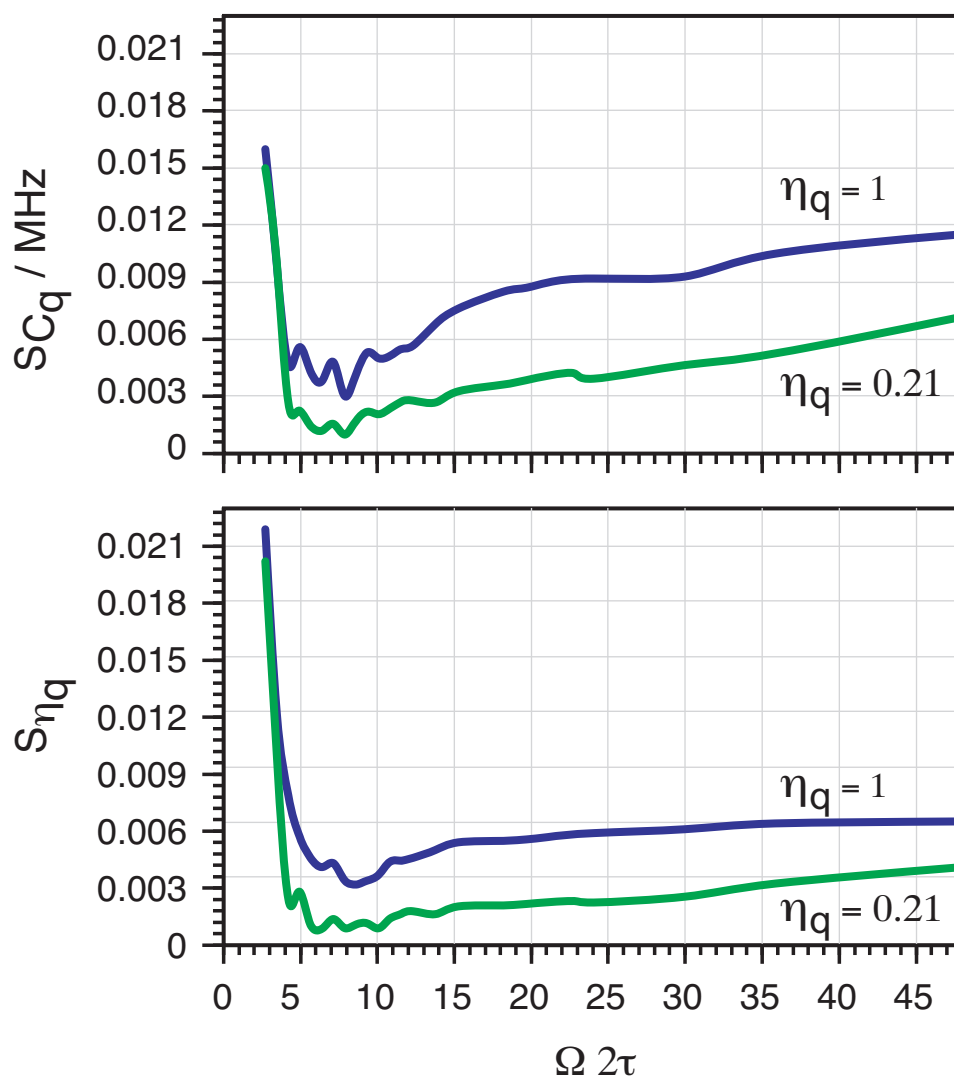


Figure 3.8: The standard deviation of the ^{87}Rb quadrupolar coupling constant and asymmetry parameter extracted from simulated ^{207}Pb resonance CPMG-MAS spectra as a function of $\Omega 2\tau$ for $\eta_q = 0.21$ and $\eta_q = 1$, while keeping span ($\Omega_{q,MAS} = 4.48$ kHz) and pre-CPMG signal-to-noise ratio ($S/N = 6.93$) constant. A spinning speed of 12.5 kHz was used for simulation.

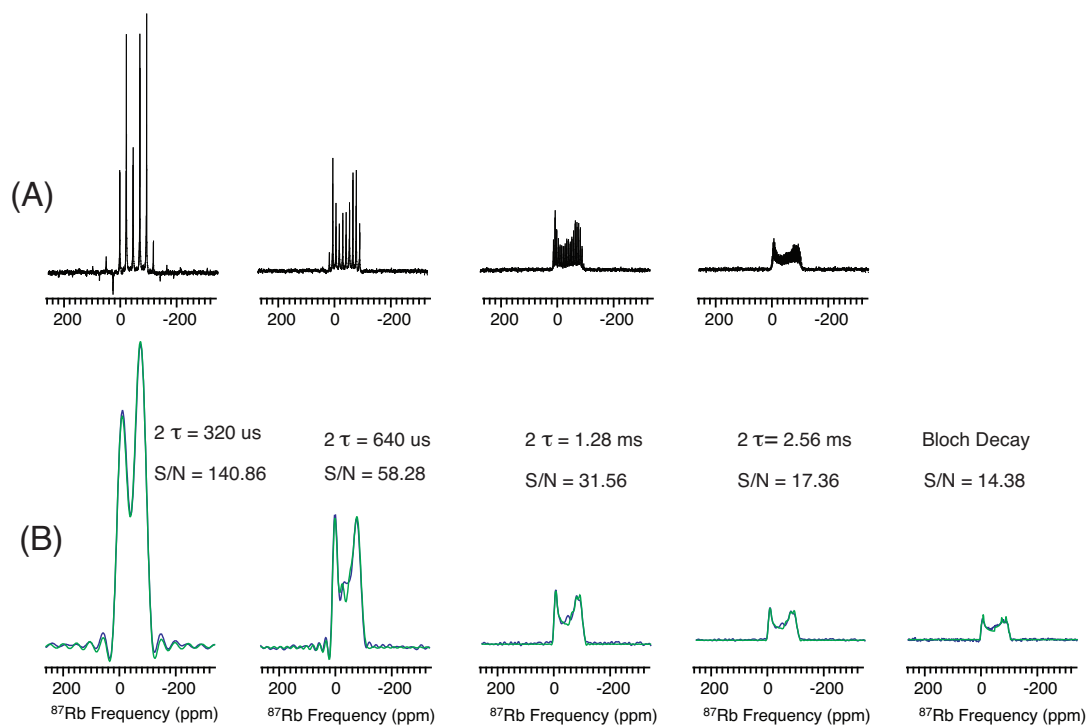


Figure 3.9: The static CPMG experimental spectra of ^{87}Rb resonance in RbClO_4 powder sample as function of π pulse spacing. Top row is processed using “spikelet” approach of Larsen et.al [2]. The bottom row is processed using our modified TOP [3] processing method. Also shown are the “best-fit” model lineshapes which take signal truncation inside 2τ acquisition window into account.

Experimental TOP-CPMG-MAS CT spectra of ^{87}Rb resonance from polycrystalline RbClO_4 as a function of π pulse spacing are shown in Fig. 3.7. To avoid interference with the MAS averaging of anisotropies it is important when combining CPMG with MAS that the π pulse spacing be synchronized to be an integer multiple of the rotor period. As expected, CPMG acquisition provides over an order of magnitude sensitivity enhancement compared to the Bloch decay experiment. Once again, notice that the lineshape distortions due to signal truncation are more easily discernible in the TOP-CPMG rather than the sideband spectrum. As before, we include the effect of this signal truncation in the second-order quadrupole MAS lineshape model to improve the least-squares fit. These “best fits” lineshapes are also shown in Fig. 3.7 for the TOP-CPMG spectra. The dependence of the uncertainty in C_q and η_q on the CPMG π pulse spacing is observed in their standard deviations shown in Table 3.5. The CPMG π pulse spacing that gives the minimum uncertainty for C_q and η_q values is $2\tau = 2.56$ ms, with values of 3.17 MHz and 0.20, respectively. These values differ slightly from the values of $C_q = 3.3$ MHz and $\eta_q = 0.21$ obtained by Vosegaard *et. al* [67] in their single crystal study. Given the previously mentioned temperature dependence of C_q in RbClO_4 this is not surprising. The ^{87}Rb MAS CT spectrum has a span of $\Omega_{q,\text{MAS}} = 4,399$ Hz, so the minimum uncertainty is obtained at $\Omega_{q,\text{MAS}} 2\tau \approx 11$ in this set of experiments.

To better understand how CPMG acquisition affects the uncertainty in C_q and η_q , we have simulated ^{87}Rb TOP-CPMG-MAS spectra as a function of CPMG π pulse spacing for two different asymmetry parameters, $\eta_q = 0.21$ and $\eta_q = 1$, while holding the span ($\Omega = 4.48$ kHz), pre-CPMG signal-to-noise ratio, and the total acquisition time constant. Plots of the standard deviations for C_q and η_q as a function of $\Omega 2\tau$ are shown in Fig. 3.8. The minimum uncertainty in both C_q and η_q occur in the range $\Omega 2\tau \approx 9_{-2}^{+3}$. There is a general increase in uncertainty for both C_q and η_q when

$\eta_q=1$, which could be simply explained by the decrease in the number and intensity of discontinuities in the CT MAS lineshape when $\eta_q = 1$.

Finally, we examined the CPMG acquisition for the ^{87}Rb CT spectra of a static polycrystalline sample of RbClO_4 . The TOP-CPMG CT spectra as a function of 2τ are shown in Fig. 3.9. As before, lineshape distortions due to signal truncation are more easily discernible in the TOP-CPMG spectrum than the sideband spectrum. Using constraints of $C_q=3.3$ MHz and $\eta_q=0.21$ obtained from the single crystal study [67], and including the effects of signal truncation from the 2τ acquisition window, we performed a least-squares analysis of each lineshape and obtained the nuclear shielding tensor parameters, ζ_s , η_s , and their relative orientation, α , β , and γ , to the quadrupole tensor as a function of CPMG π pulse spacing. These values are shown in Table 3.1. Although we have an expression in Eq. (3.2.9) for the span of a CT lineshape in a static sample due to second-order quadrupole interaction, we are not aware of an analytical expression that includes the effects of both quadrupole and nuclear shielding interactions. With the experimental span of $\Omega_{q,\text{Static}} = 18$ kHz and a minimum uncertainty found almost consistently at $2\tau = 640 \mu\text{s}$ for all parameters in the least-squares analysis of the static TOP-CPMG lineshapes we experimentally observe that $\Omega_{q,\text{Static}}2\tau = 11.5$. A value consistent with the optimum range of values observed for both the static nuclear shielding lineshape and the MAS CT second-order quadrupole lineshape.

Table 3.2 is a comparison between the parameters obtained from our least-squares analysis of the TOP-CPMG spectrum and single crystal study of Vosegaard et al. [67]. The value of ζ_s and η_s are very similar to the reported value from single crystal study, however the value of α , β and γ are not fully in agreement with the single crystal study. This difference is simply attributed to the general ill-posed problem of fitting a CT spectrum of a static polycrystalline sample for both nuclear shielding and

quadrupole coupling parameters and their relative tensor orientation. This challenge in analyzing CT anisotropic lineshapes in polycrystalline samples was the motivation behind the development of the two-dimensional COASTER [68] experiment which cleanly separates the nuclear shielding and second-order quadrupole anisotropic lineshapes, thereby eliminating the covariance between nuclear shielding and quadrupole tensor components, and significantly reducing model parameter uncertainties.

3.5 Summary

CPMG acquisition has become an increasingly popular approach for increasing sensitivity of solid-state NMR spectra that have significant inhomogeneous (*i.e.*, anisotropic) broadenings. While increasing sensitivity is important, in the case of CPMG it comes with a loss of information about the NMR spin interactions. We have attempted to quantify this information loss in terms of the uncertainty of the NMR interaction tensor parameters extracted in a least-squares analysis of the CPMG-enhanced spectrum obtained as a function of CPMG π pulse spacing. To aid in this analysis we introduce the use of TOP processing for the CPMG signal echo train to obtain a more conventional powder pattern lineshape, instead of using a direct Fourier transform of the echo train signal which yields a sideband (or “spikelet”) spectrum. The TOP processed CPMG spectrum also has the advantage that the effect of signal truncation inside the 2τ CPMG acquisition window is readily discerned.

From our investigations of TOP-CPMG spectra with extensive least squares analyses we found for an anisotropic nuclear shielding or chemical shift lineshape in a static sample that the range of optimum π pulse spacings which minimize NMR parameter uncertainty while maximizing enhancement occur when $\Omega 2\tau \approx 12_{-1}^{+6}$ for $\eta_s = 0$ and $\Omega 2\tau \approx 9_{-3}^{+3}$ for $\eta_s = 1$, where 2τ is the π pulse spacing, Ω is the span of

the anisotropic lineshape, and η_s is the asymmetry parameter for the nuclear shielding tensor. For an anisotropic second-order quadrupolar central transition lineshape under MAS a range of $\Omega 2\tau \approx 9_{-2}^{+3}$, regardless of η_q , minimized the uncertainty when determining the quadrupole tensor parameters.

Generally, the optimum π pulse spacing occurs in a range of values asymmetrically spaced around $\Omega 2\tau \sim 11$, regardless of the interactions contributing to the lineshape. The analyses and conclusions described here are applicable to any CPMG-enhanced solid-state NMR experiment and thus should serve to reduce significantly experimental setup and optimization times.

$2\tau/\text{ms}$	ζ_s/ppm	η_s	α	β	γ
∞	$10.85 \pm \mathbf{0.26}$	$0.41 \pm \mathbf{0.01}$	$154.11^\circ \pm \mathbf{4.01}^\circ$	$33.68^\circ \pm \mathbf{0.79}^\circ$	$107.70^\circ \pm \mathbf{2.91}^\circ$
2.56	$12.33 \pm \mathbf{0.17}$	$0.49 \pm \mathbf{0.03}$	$153.53^\circ \pm \mathbf{2.92}^\circ$	$21.31^\circ \pm \mathbf{0.59}^\circ$	$77.35^\circ \pm \mathbf{4.01}^\circ$
1.28	$12.35 \pm \mathbf{0.19}$	$0.60 \pm \mathbf{0.02}$	$150.67^\circ \pm \mathbf{2.86}^\circ$	$16.61^\circ \pm \mathbf{0.55}^\circ$	$66.97^\circ \pm \mathbf{3.95}^\circ$
0.640	$13.18 \pm \mathbf{0.11}$	$0.66 \pm \mathbf{0.04}$	$123.76^\circ \pm \mathbf{2.52}^\circ$	$15.86^\circ \pm \mathbf{0.51}^\circ$	$100.16^\circ \pm \mathbf{3.15}^\circ$
0.320	$16.11 \pm \mathbf{0.41}$	$0.92 \pm \mathbf{0.07}$	$107.13^\circ \pm \mathbf{5.15}^\circ$	$27.49^\circ \pm \mathbf{1.25}^\circ$	$151.09^\circ \pm \mathbf{4.79}^\circ$

Table 3.1: Values of ζ_s , η_s , α , β , and γ obtained for ^{87}Rb resonance in RbClO_4 powder using static CPMG experiment

Crystal	ζ_s /ppm	η_s	α	β	γ	Reference
Static	$13.18 \pm \mathbf{0.11}$	$0.66 \pm \mathbf{0.04}$	$123.76^\circ \pm \mathbf{2.52}^\circ$	$15.86^\circ \pm \mathbf{0.51}^\circ$	$100.16^\circ \pm \mathbf{3.15}^\circ$	This work
Single-Crystal	$13.80 \pm \mathbf{1.50}$	$0.61 \pm \mathbf{0.24}$	$94.00^\circ \pm \mathbf{14.0}^\circ$	$28.00^\circ \pm \mathbf{4.00}^\circ$	$87.00^\circ \pm \mathbf{5.00}^\circ$	[67]
Static	$14 \pm \mathbf{2}$	$0.5 \pm \mathbf{0.3}$	$112.00^\circ \pm \mathbf{6.0}^\circ$	$28.80^\circ \pm \mathbf{1.5}^\circ$	$16.00^\circ \pm \mathbf{4.00}^\circ$	[67]

Table 3.2: Chemical shift anisotropy (ζ_s, η_s) and relative orientations (α, β, γ) of the chemical shift anisotropy tensor and quadrupole tensor. These values obtained for ^{87}Rb resonance in RbClO_4 powder by fitting static CPMG spectra keeping $C_q=3.3$ MHz and $\eta_q=0.21$ as a constrain. The definition of (α, β, γ) is in accord with the definition used in Ref. [69].

$2\tau/\text{ms}$	C_q/MHz	η_q	δ_{iso}/ppm
∞	$3.1542 \pm \mathbf{0.0022}$	$0.2086 \pm \mathbf{0.0013}$	$-12.802 \pm \mathbf{0.020}$
10.24	$3.1651 \pm \mathbf{0.0012}$	$0.2076 \pm \mathbf{0.0006}$	$-12.813 \pm \mathbf{0.010}$
5.12	$3.1694 \pm \mathbf{0.0009}$	$0.2065 \pm \mathbf{0.0006}$	$-12.809 \pm \mathbf{0.009}$
2.56	$3.1681 \pm \mathbf{0.0009}$	$0.2037 \pm \mathbf{0.0005}$	$-12.959 \pm \mathbf{0.008}$
1.28	$3.2075 \pm \mathbf{0.0026}$	$0.2816 \pm \mathbf{0.0016}$	$-11.553 \pm \mathbf{0.022}$

Table 3.3: C_q and η_q obtained for different values of 2τ for ^{87}Rb resonance in RbClO_4 powder using MAS CPMG experiment.

$2\tau/\text{ms}$	δ_{11}/ppm	δ_{22}/ppm	δ_{33}/ppm
∞	$-3473.3 \pm \mathbf{0.05}$	$-3476.0 \pm \mathbf{0.05}$	$-3531.1 \pm \mathbf{0.17}$
10.24	$-3471.8 \pm \mathbf{0.05}$	$-3473.7 \pm \mathbf{0.04}$	$-3527.4 \pm \mathbf{0.16}$
5.12	$-3472.2 \pm \mathbf{0.02}$	$-3473.3 \pm \mathbf{0.02}$	$-3527.6 \pm \mathbf{0.07}$
2.56	$-3470.0 \pm \mathbf{0.04}$	$-3476.7 \pm \mathbf{0.04}$	$-3527.5 \pm \mathbf{0.10}$
1.28	$-3467.5 \pm \mathbf{0.17}$	$-3473.6 \pm \mathbf{0.17}$	$-3518.1 \pm \mathbf{0.21}$

Table 3.4: The principal components, δ_{11} , δ_{22} , and δ_{33} of the chemical shift tensor and their associated errors obtained from a least-squares analysis of the spectra in Fig. 3.3 as a function of the CPMG π pulse spacing in the case of the ^{207}Pb resonance in $\text{Pb}(\text{NO}_3)_2$ powder.

CHAPTER 4

ENHANCING SENSITIVITY IN 2D PASS NMR WITH CPMG ACQUISITION

4.1 Introduction

The full nuclear shielding tensor contains important information related to structural details concerning the local bonding environment of a nuclei of interest. While the full tensor components can be obtained through acquisition of a static powder pattern, this approach suffers from low sensitivity since the integrated area of the lineshape is spread over a large frequency region. Sensitivity is somewhat improved in spinning samples because the intensity of the resulting spinning sideband pattern is related to the magnitude of the nuclear shielding anisotropy [70]. While the area of the sidebands for a given site is quantitative, differentiating between sidebands for multiple sites in a 1D NMR spectrum can be complicated. Therefore, to properly determine the nuclear shielding anisotropy for a system composed of multiple nonequivalent sites it is beneficial to use techniques such as Magic Angle Flipping (MAF) [71, 72], Magic Angle Hopping (MAH) [73], Magic Angle Turning (MAT) [74], or 2D Phase Adjusted Spinning Sidebands (2D PASS) [4, 75] that correlate a high resolution isotropic dimension to an anisotropic dimension to improve resolution. While effective, MAF suffers from low sensitivity since magnetization is lost during the long hop delay during which time the magnetization is stored to Zeeman order, limiting its overall

applicability to ^{29}Si enriched samples and laboratories capable of performing variable angle experiments. For this reason it is preferable to utilize a technique (MAT or 2D PASS) that provides complimentary information to MAF while improving sensitivity and can be implemented on a commercially available MAS probe.

A common method for improving sensitivity is to utilize Carr-Purcell-Meiboom-Gill (CPMG) [52, 53] detection where, for NMR lineshapes broadened by inhomogeneous interactions, an echo-train is acquired in the time domain by consistently refocussing the magnetization through the application of a series of π -pulses. Due to its relatively easy application, CPMG acquisition has been used for sensitivity enhancement in MRI [76] and for solid-state NMR experiments of low gamma nuclei and quadrupolar nuclei [77, 78]. In the case of solid state NMR of spin-1/2 nuclei, CPMG has also received considerable attention in analyzing both static and spinning samples because the acquisition of multiple echoes in the time domain can reduce experimental time for samples with long T_1 [79–82]. Previous studies [83, 84] have already demonstrated that the acquisition dimension of MAT can be successfully replaced by CPMG acquisition to enhance sensitivity. However, to avoid truncation multiple rotor periods are needed during data acquisition, which seriously affects the signal enhancement for samples with small T_2 . Also, since the decay in indirect dimension (t_1) is related to the isotropic shift components, the acquisition requires more 2D data points to obtain a non truncated isotropic dimension. This increases the required experimental time and limits the overall applicability of MAT. In contrast, the 2D PASS experiment acquires signal in t_1 as a function of the rotor pitch where the signal is solely governed by anisotropic interactions. This limits the number of acquired data points in t_1 to the number of sidebands needed to resolve the full spinning sideband pattern, providing a significant time savings over MAT. Recently Hung and Gan [85] have combined MAT and PASS into a single experiment (MAT-PASS)

that combines the benefits of both techniques, but its applications has been limited to a qualitative analysis of model compounds.

The coordination of silicon is commonly studied by ^{29}Si MAS NMR since silicon in a tetrahedral coordination with varying numbers of bridging oxygens ($\text{Q}^{(n)}$ with n ranging from 0-4) can be separated on the basis of resonance shift, making it a powerful probe of atomic structure [86]. However, in disordered materials where a distribution of isotropic chemical shifts exists, lineshapes are complex due to large spectral overlap. NMR spectroscopists have generally avoided analyzing such data by unconstrained curve fitting because of the large uncertainties involved and doubts about the validity of Gaussian peak components. The concentration of $\text{Q}^{(n)}$ -species can also be calculated by fitting the static NMR spectrum since the CSA parameters (ζ and η) for each $\text{Q}^{(n)}$ -species varies significantly allowing multiple sites to be distinguished [87]. In this study we have applied ^{29}Si 2D PASS NMR (Figure 4.1) to quantify $\text{Q}^{(n)}$ -species distributions in potassium disilicate glass ($\text{K}_2\text{O} \cdot 2\text{SiO}_2$). While 2D PASS has been utilized to determine chemical shift parameters [88–92] and bonding environments [93], studies using 2D PASS NMR to quantify the relative concentration of different sites are limited [94]. To further improve sensitivity CPMG [52, 53] detection has been added to the 2D PASS pulse sequence proposed by Antzutkin et al. [4] utilizing a Cogwheel phase cycle, and a data processing scheme presented that treats the 2D PASS CPMG spectrum as a pseudo-3D dataset. To validate that a similar quantitative analysis can be obtained from 2D PASS, 2D PASS CPMG, and MAF, studies of two potassium disilicate glasses (one with ^{29}Si in natural abundance (4.6 %) and one that had been fully enriched) are compared to previously reported concentrations [95]. To reduce experiment time by minimizing the required number of steps in the phase cycle, effects of pulse imperfections, and eliminate contributions

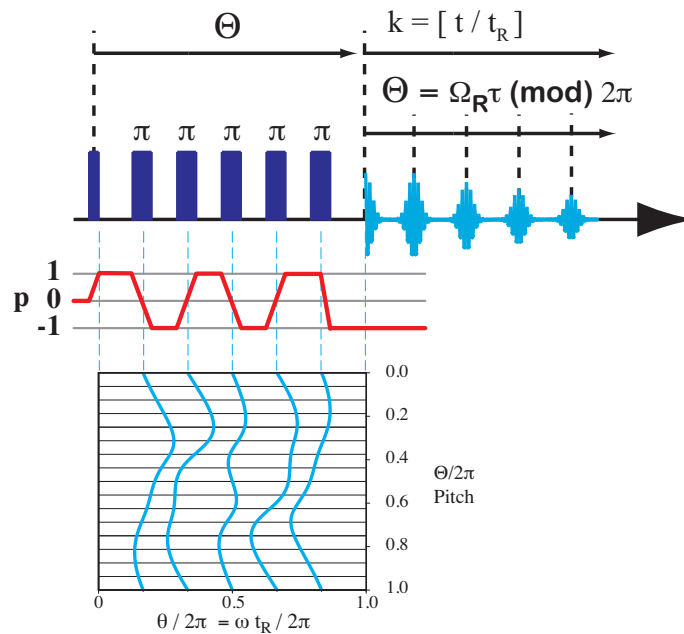


Figure 4.1: 2D PASS pulse sequence from Antzutkin et al. [4] where Θ represents the rotor pitch and Ω_R is the rotor spinning frequency.

from unwanted coherence pathways a Cogwheel phase cycle has also been utilized that expands on previous work by Ivchenko et al. [96].

4.2 Experimental

4.2.1 Sample Preparation

Natural abundance $\text{K}_2\text{O} \cdot 2\text{SiO}_2$ was synthesized by adding the appropriate molar ratios of potassium carbonate and fumed silica. The sample was heated at 700°C for 12 hours to decarbonate after which it was melted at 1550°C for 3 hours and rapidly quenched in water. A 0.02 wt. % of gadolinium oxide was also added after decarbonation and prior to melting to aide in relaxation. Each sample was then crushed under nitrogen with a mortar and pestle and rapidly packed in a 4 mm rotor

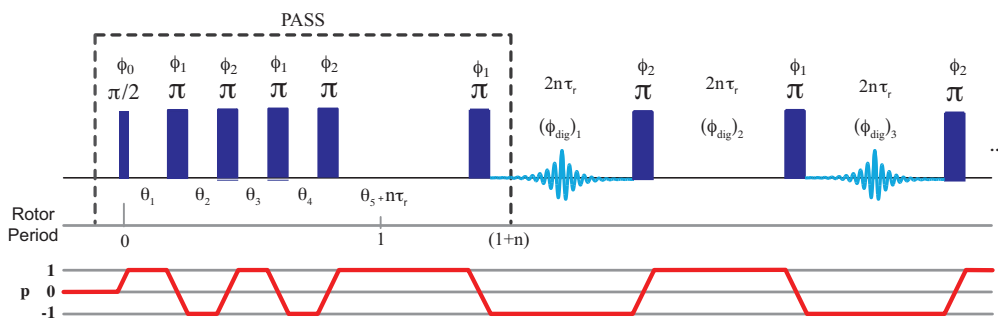


Figure 4.2: 2D PASS-CPMG pulse sequence where τ_r is the rotor period, n is an integer corresponding to the number of rotor periods, $\phi_o = \phi_2 = 0$, ϕ_1 is given in equation 4.3.20, and ϕ_{dig} is given in equation 4.3.21.

to avoid exposure to air. Synthesis of the enriched sample has been discussed in a previous work [95].

4.2.2 Nuclear Magnetic Resonance Spectroscopy

All NMR experiments were conducted on a Bruker DMX Spectrometer, interfaced to a 4 mm MAS probe operating at a field strength of 9.4 T (corresponding to a ^{29}Si frequency of 79.576102 MHz). The entire experiment was rotor synchronized to a sustained rotor frequency of $1 \text{ kHz} \pm 2 \text{ Hz}$. A shifted echo version of 2D PASS is utilized, where a delay of one rotor period (τ_r) is used prior to the fifth π pulse, which gives a full echo at $3\tau_r$ for zero rotor pitch. Fixed CPMG π pulses are placed at integral multiples of the rotor period to avoid interference with rotational echoes. The pulse sequence and coherence transfer diagram for the 2D PASS experiment proposed by Antzutkin et al. [4] is given in Figure 4.1. Each π pulse leads to an alternating coherence order between +1 and -1, where the timings between each pulse determines the phase of the acquired echo. While coherence transfer is 100% efficient

for a perfect π pulses, pulse imperfections lead to finite coherence transfer between any of the three possible coherence pathways (+1, 0, -1) in an isolated spin-1/2 system. For an experiment involving five imperfect π pulses, the minimum number of required steps using a traditional nested phase cycle is 243, which leads to a very long experimental time particularly for samples with long T_1 . For this reason all 2D PASS experiments on the ^{29}Si -enriched potassium disilicate were carried out using an 11 step cogwheel phase cycle [96] to reduce experiment time. A processing approach is utilized that treats the 2D PASS CPMG (Figure 4.2) experiment as a pseudo three dimensional experiment with separate dimensions corresponding to acquisition time, rotor pitch, and CPMG echoes. The TOP approach to CPMG processing [97] is utilized to prevent complex spikelet analysis.

4.3 Results and Discussion

4.3.1 2D PASS

For the 2D PASS experiment proposed by Antzutkin et al. [4] the frequency domain signal can be represented as

$$\Omega(t, \phi_o) = \sum_{l=0}^{\infty} \omega_{l,0}(\Omega_{PR}) + \sum_{l=0}^{\infty} \sum_{m \neq 0} \omega_{l,m}(\Omega_{PR}) e^{im(\Omega_r t + \phi_0)} \quad (4.3.1)$$

where ϕ_0 is the initial rotor phase, Ω_R is the rotor spinning frequency, $\omega_{l,0}(\Omega_{PR})$ are the isotropic components of the frequency, and $\omega_{l,m}(\Omega_{PR})$ are the complex Fourier components depending upon the orientation $\Omega_R = (\alpha_{PR}, \beta_{PR}, \gamma_{PR})$ of the principle axis system (PAS) of the CSA tensor with respect to a rotor system (R), where the z axis of R is fixed along the rotation axis. The phase at any time t can then be

written as

$$\Phi(t, \phi_0) = \int_0^t \Omega(s) ds = W_{l,0}t + \sum_{m \neq 0} W_{l,m} [e^{im(\Omega_R t + \phi_0)} - e^{im\phi_0}] \quad (4.3.2)$$

where

$$W_{l,0} = \sum_{l=0}^{\infty} \omega_{l,0}(\Omega_{PR}) \quad (4.3.3)$$

and

$$W_{l,m} = \sum_{l=1}^{\infty} \frac{\omega_{l,m}(\Omega_{PR})}{im\Omega_R}. \quad (4.3.4)$$

Following the approach first used by Dixon [75] and expanded by Antzutkin et al. [4], the phase can be manipulated using a series of π pulses at time τ_j from the initial excitation pulse. In 2D PASS the signal must evolve in t_1 as a function of rotor pitch so the signal phase is manipulated to have the form

$$\Phi_{PASS} = - \sum_{l,m \neq 0} iW_{l,m} e^{im\phi_0} [e^{im(\Omega_R t + \Theta)} - 1] \quad (4.3.5)$$

where Θ is the applied rotor pitch. Since chemical shift anisotropy is a second rank tensor with $l = 2$, there are $2l + 1$ possible values of m requiring at least five evolution periods separated by five π pulses. Writing the π pulse spacing in terms of pitch defined by $\theta_j = \tau_j \Omega_R$, and $\theta_T = \Omega_R T$, where T is the total PASS period, we can write the condition for PASS containing n π pulses as

$$-(-1)^n e^{im(\Theta + \theta_T)} + 1 + 2 \sum_{j=1}^n (-1)^j e^{im\theta_j} = 0 \quad (4.3.6)$$

and

$$\theta_T + 2 \sum_{j=1}^n (-1)^{j+n} \theta_j = 0. \quad (4.3.7)$$

The real and imaginary part of the equation (4.3.6) and (4.3.7) contain a set of five nonlinear equations with $n + 1$ unknowns ($\theta_1, \dots, \theta_n,$) and θ_T . Setting $n = 5$ the above equations can be solved numerically.

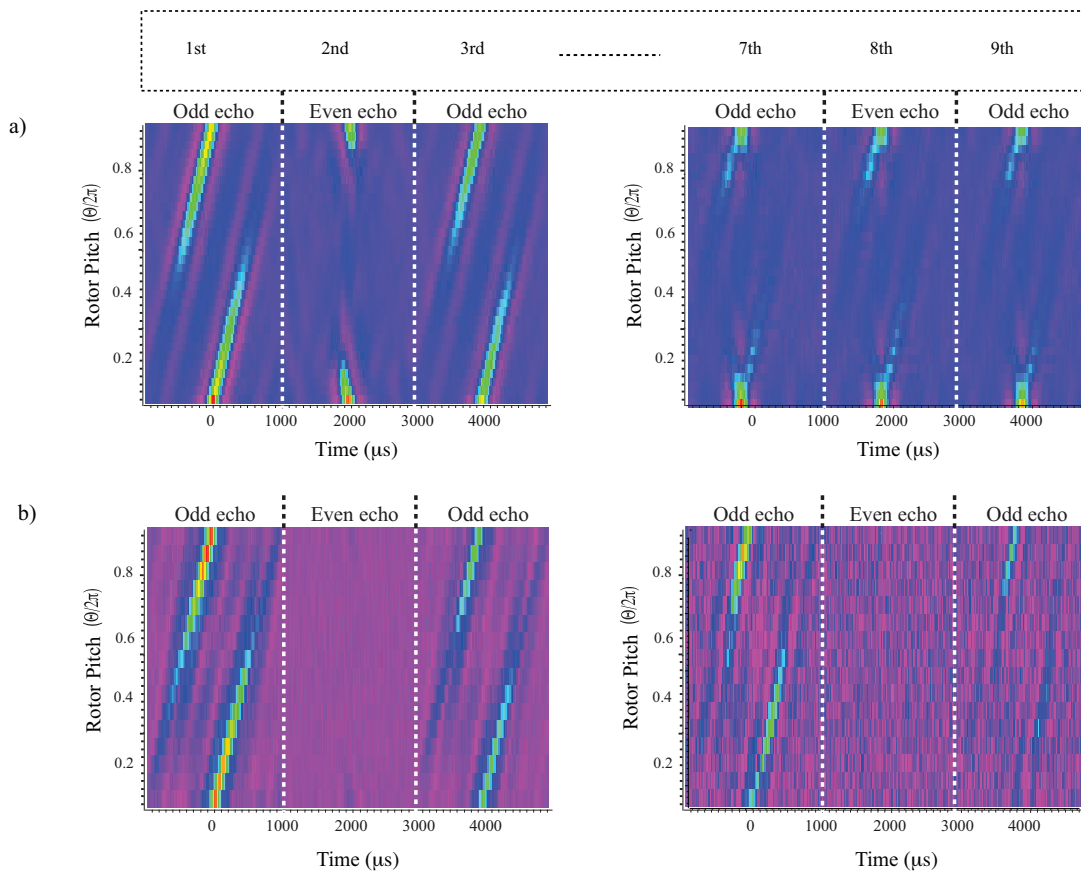


Figure 4.3: ^{29}Si 2D PASS CPMG NMR time domain data for a sequence a) where the CPMG pulses are not phase cycled, demonstrating that even echoes do not evolve in the rotor pitch dimension and b) where a Cogwheel phase cycle is used for all CPMG pulses, demonstrating that even echoes are removed. Also, for a) the 7th, 8th and 9th echoes have contributions from unwanted coherence pathways while those in b) are unaffected.

4.3.2 2D PASS CPMG

In 2D PASS NMR the interpulse spacing of the first five π pulses are determined by the solution of five pulse PASS equations described by Antzutkin et al. [4] given in Equations 4.3.6 and 4.3.7. For full echo acquisition, an integer multiple of the rotor period is added just before the fifth π pulse to make a shifted echo 2D PASS experiment. For CPMG acquisition acquisition the π pulse spacings are rotor synchronized to one rotor period. In this context of 2D PASS CPMG, the PASS equations can be written as

$$-(-1)^5 e^{im(\Theta+\theta_T)} + 1 + 2 \sum_{j=1}^5 (-1)^j e^{im\theta_j} + 2 \sum_{j=6}^n (-1)^j e^{im\theta_j} = 0 \quad (4.3.8)$$

and

$$2\pi + 2 \sum_{j=1}^5 (-1)^{j+5} \theta_j + \theta_T + 2 \sum_{j=6}^n (-1)^{j+n} \theta_j = 0 \quad (4.3.9)$$

where the CPMG part of the PASS equation is written as

$$2 \sum_{j=6}^n (-1)^j e^{im\theta_j} \quad (4.3.10)$$

and

$$\theta_T + 2 \sum_{j=6}^n (-1)^{j+n} \theta_j. \quad (4.3.11)$$

In this context a 2D PASS experiment with CPMG acquisition can be modeled as traditional 2D PASS experiment with a total number (PASS and CPMG) of n π pulses (Figure 4.2). Using equations (4.3.8) and (4.3.9) it can be shown that for experiments where n is an odd number, the conditions in equations (4.3.8) and (4.3.9) are satisfied while experiments where n is an even number do not (i.e. equations (4.3.8) and (4.3.9) $\neq 0$), which has been observed in the time domain data for a ^{29}Si 2D PASS CPMG experiment conducted on a ^{29}Si -enriched $\text{K}_2\text{O} \cdot 2\text{SiO}_2$ (Figure 5.5a).

One possible alternative for making each echo satisfy the solutions to the PASS equations is adding a z-filter following the PASS block and prior to the start of the CPMG acquisition. However, by using z-filter the expected signal loss while the magnetization is stored to Zeeman order is a $\sqrt{2}$, which is equal to the sensitivity gained from acquiring twice as many transients. Therefore, there would be no additional time savings.

4.3.3 2D PASS CPMG Phase Cycling

In typical CPMG pulse sequence the π -pulses in the CPMG pulse train are not phase cycled and it is assumed that mixing of different coherence pathways due to imperfect pulse lengths is not problematic since each pathway is equivalent. However, a recent study by Goswami et al. [98] observed that when CPMG is added to double quantum experiments, contributions from unwanted coherence pathways begin to affect the acquired signal as more echoes in the CPMG train are acquired. Similar observations were made in this study when CPMG was added to 2D PASS (Figure 5.5a). However, if a traditional nested phase cycle [99, 100] were used for Q π -pulses in the CPMG train, the minimum number of required steps in the phase cycle would be 3^Q (i.e., for $Q = 13$ the required phase cycle will be 1594323 steps).

A convenient alternative is to employ Cogwheel phase cycling originally proposed by Levitt et al. [101]. Here, we have expanded on the treatment of Ivchenko et al. [96] for a 2D PASS sequence with Q π pulses to derive a comprehensive phase cycle for 2D PASS with CPMG acquisition.

4.3.3.1 Cogwheel Phase Cycling for CPMG pulses

For a 2D PASS CPMG experiment with a total Q number of π pulses (including the 5 π pulses in PASS block), following the initial excitation from a $\pi/2$ pulse each pulse

can be cycled as

$$\phi_q^{(m)} = \frac{2\pi\nu_q m}{N} \quad (4.3.12)$$

$$\phi_{rec}^{(m)} = \frac{2\pi\nu_{rec} m}{N} \quad (4.3.13)$$

$$\phi_{dig}^{(m)} = \frac{2\pi\nu_{dig} m}{N} \quad (4.3.14)$$

where ν_q , ν_{rec} , and ν_{dig} are different integers, called winding number for each element q , the receiver, and the digitizer for a phase cycle with a total number of steps N .

The phase for each transient m ($m \in N$) can be written

$$\begin{aligned} \Phi^{(m)}(\mathbf{P}) &= \phi_0^{(m)} \Delta P_0 + \phi_1^{(m)} \Delta P_1 + \dots \\ &\quad \phi_Q^{(m)} \Delta P_Q + \phi_{dig} + \phi_{rec} \end{aligned} \quad (4.3.15)$$

$$\begin{aligned} &= \frac{2\pi m}{N} [\nu_1 \Delta P_0 + \nu_2 \Delta P_1 + \dots \\ &\quad \nu_Q \Delta P_Q + \nu_{dig} + \nu_{rec}] \end{aligned} \quad (4.3.16)$$

where ΔP_q is the change in coherence order ($P_q - P_{q-1}$) and P_q is the absolute coherence order between two pulses. In the 2D PASS CPMG experiment the desired pathway has absolute coherence order $P_q = \{0, +1, -1, +1, -1, +1, -1, \dots -1\}$. Equation (16) can then be reorganized in terms of the absolute coherence order and the difference in winding number between the two adjacent pulses ($\Delta\nu_{q,q+1} = \nu_{q+1} - \nu_q$) as

$$\begin{aligned} \Phi^{(m)}(\mathbf{P}) &= \frac{2\pi m}{N} [-\Delta\nu_{12} P_1 - \Delta\nu_{23} P_2 - \dots \\ &\quad -\Delta\nu_{Q-1,Q} P_{Q-1} + \Delta\nu_{det}], \end{aligned} \quad (4.3.17)$$

where $\Delta\nu_{det} = -\nu_Q + \nu_{rec} + \nu_{dig}$. To ensure constructive interference of the desired pathway (q) and destructive interference of all undesired pathways (q'), the following condition need to be satisfied

$$\sum_{q=0}^Q \Delta\nu_{q,q+1} P_q \neq \sum_{q'=0}^Q \Delta\nu_{q',q'+1} P_{q'} + N \times integer. \quad (4.3.18)$$

Additionally, the winding numbers must be chosen in such a way that $\sum_{q=0}^Q \Delta\nu_{q,q+1}P_q$ is unique.

For a isolated spin-1/2 system and Q number of π pulses, the desired coherent pathway is $P = \{0, +1, -1, +1, -1, +1, -1, \dots -1\}$. To keep $\sum_{q=0}^Q \Delta\nu_{q,q+1}P_q$ unique, $\nu_{q,q+1}$ should be chosen with the same sign of P_q . The simplest solution is to choose $\Delta\nu_{q,q+1} = \{0, +1, -1, +1, -1, +1, -1, \dots \cdot 0\}$. Now with these values, the desirable pathway has $\sum_{q=0}^Q \Delta\nu_{q,q+1}P_q = +Q$ and all of the undesirable pathways have a value less than $+Q$ and a minimum value of $-Q$. The condition for equation (19) is then satisfied when $N > 2Q$ making the smallest value of $N = 2Q + 1$. One possible cogwheel phase-cycle solution for Q number of π pulses is

$$N = 2Q + 1$$

$$\nu_0 = 0, \nu_1 = +1$$

$$\nu_2 = 0, \nu_3 = +1$$

$$\nu_4 = 0, \nu_5 = +1$$

$$\nu_{Q-1} = 0, \nu_Q = +1$$

$$\nu_{rec} = 0$$

Setting

$$(\nu_0, \nu_1, \nu_2, \nu_3, \nu_4, \nu_5, \dots) = (0, +1, 0, +1, 0, +1, \dots)$$

and

$$(\Delta P_0, \Delta P_1, \Delta P_2, \Delta P_3, \dots) = (+1, -2, +2, -2, \dots)$$

the digitizer phase can be cycled for each pulse individually to ensure that the detected signal phase is zero

$$\sum_{q=0}^Q \nu_q \Delta P_q + \nu_{rec} + \nu_{dig} = 0. \quad (4.3.19)$$

The explicit phase cycle for 2D PASS CPMG is then

$$\phi_0 = \phi_2 = \phi_4 \cdots \phi_q = 0,$$

when q is even ($q \in Q$) and

$$\phi_1 = \phi_3 = \phi_5 = \cdots \phi_{q'} = \frac{2\pi m}{2Q + 1}, \quad (4.3.20)$$

when q' is odd ($q' \in Q$). The digitizer phase after k number of π pulse is given by

$$\phi_{dig}^k = -\frac{2\pi m}{2Q + 1} \sum_{q=0}^k \nu_q \Delta P_q, \quad (4.3.21)$$

where $k \leq Q$ ($k \in Q$). Therefore, for a thirty six step phase cycle ($N = 36$) with a total number of seventeen π -pulses ($Q = 17$), the even π -pulses will have a phase set to $\phi = 0$, the odd π -pulses will be incremented by 10° , and the digitizer phase is calculated individually for each acquired echo. In this way a time domain dataset is obtained where only even echoes are acquired.

4.3.4 2D PASS CPMG Processing

Typically CPMG spectra are processed using the "spikelet" approach where the time domain data is directly Fourier transformed to yield a 1D frequency domain spectrum with a series of spikelets that map the envelope of the lineshape. While this method is direct, deconstructing the complex "spikelet" pattern for each component is difficult. This problem is alleviated using the TOP processing approach as described by Dey et al. [97] where the CPMG spectrum is plotted as a 2D dataset and a frequency domain spectrum obtained which resembles a traditional 1D lineshape. Each 2D

slice of the PASS spectrum can be processed with this approach and reassembled into a 2D PASS spectrum (Figure 4.4). Once assembled the 2D time domain PASS signal can be expressed as

$$S(\Theta, t_2) = \sum_{k=-\infty}^{k=\infty} a^k \cdot a^{*k} e^{-ik\Theta} e^{i(\omega_{iso} + k\omega_r)t_2} e^{-\lambda(T+t_2)}, \quad (4.3.22)$$

where Θ is the rotor pitch, a^k is the complex sideband amplitude, and λ is a constant. After applying a shearing transform of $e^{-ik\omega_r t_2}$, we can separate rotor pitch and isotropic evolution in two orthogonal dimensions. The sheared signal can be written as

$$S(\Theta, t'_2) = \sum_{k=-\infty}^{k=\infty} a^k \cdot a^{*k} e^{-ik\Theta} e^{i\omega_{iso}t_2} e^{-\lambda(T+t_2)}. \quad (4.3.23)$$

Fourier transform of the 2D PASS signal gives

$$S(N, \omega'_2) = I_N L(\omega_2 - \omega_{iso}), \quad (4.3.24)$$

where $L(\omega_2 - \omega_{iso})$ is a Lorentzian line-shape positioned at isotropic frequency and I_N represents sideband order.

The acquisition of multiple echoes is beneficial through the multiplex advantage while processing using the TOP approach reduces the effects of acquired noise. In this manner a further sensitivity gain of 1.9x PASS was observed via CPMG acquisition (Figure 4.5). However, this enhancement factor is determined by the T_2 of the sample and the required acquisition time (dependent on T_2^*) in the CPMG pulse train. For samples with long T_2 or where the required acquisition time for each echo is small, this enhancement factor will be increased.

4.3.5 Application of 2D ^{29}Si PASS and PASS CPMG NMR to Silicate Glasses

Measurement of the relative abundance of anionic species in silicate glasses is essential for any structure-based model of thermodynamic or transport properties of silicate

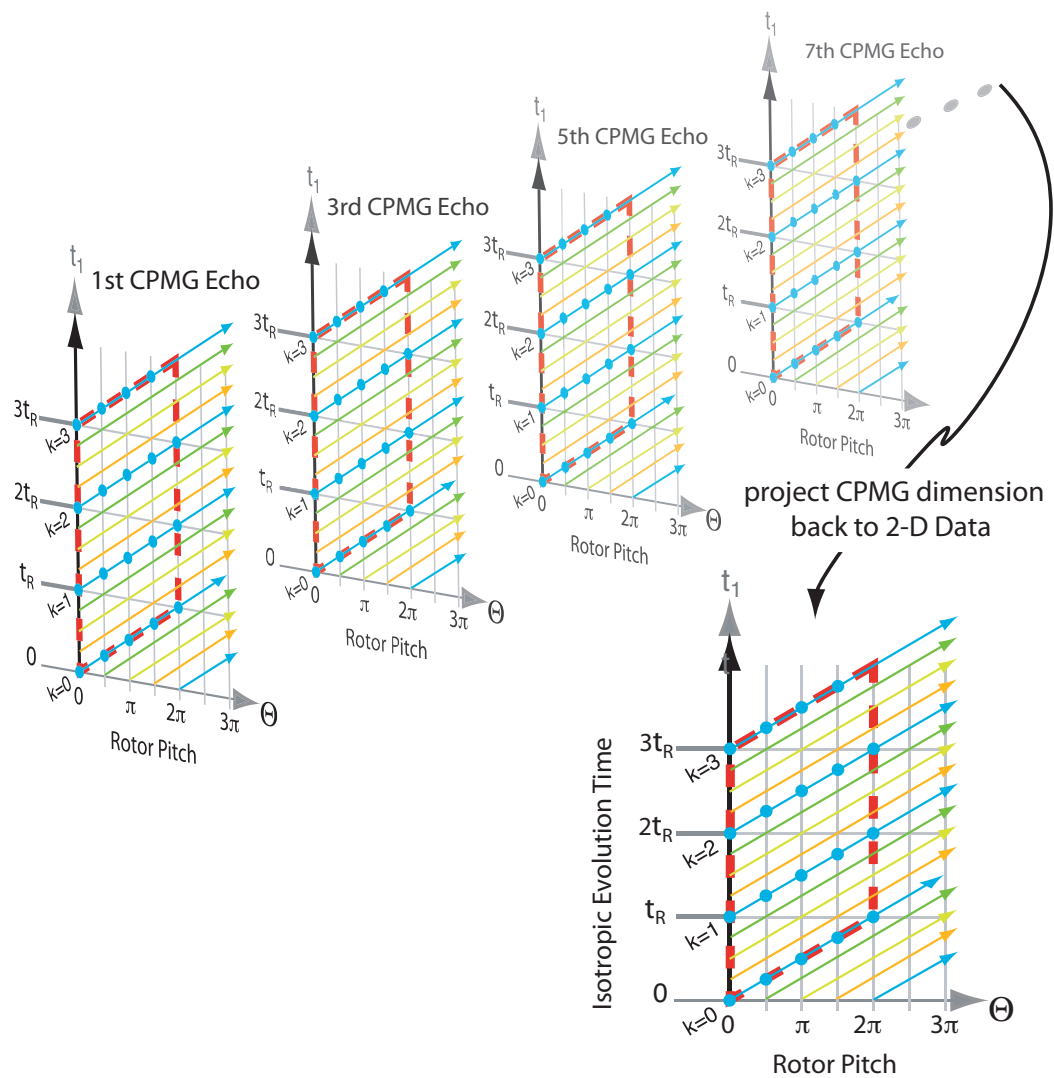


Figure 4.4: Schematic of the TOP approach to CPMG processing and subsequent reorganization into a 2D PASS dataset.

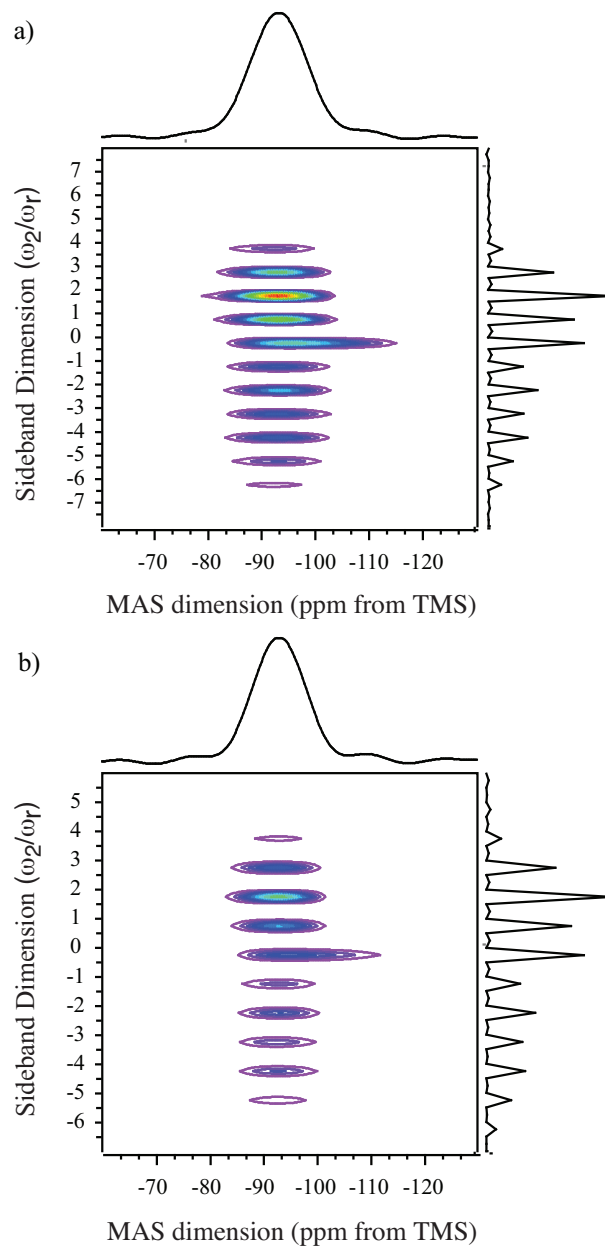
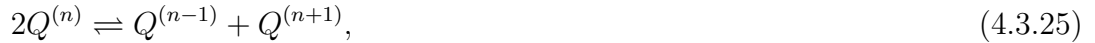


Figure 4.5: Comparison between the a) ^{29}Si 2D PASS CPMG NMR spectrum ($S/N = 137$) and the b) ^{29}Si 2D PASS NMR spectrum ($S/N = 72$) of a $\text{K}_2\text{O} \cdot 2.2\text{SiO}_2$ glass.

liquids and magmas. Being more quantitative than Raman spectroscopy, ^{29}Si NMR has provided the most convincing evidence that the $Q^{(n)}$ species distribution in silicate glasses and melts is not random but closer to binary (i.e., contains a maximum of two $Q^{(n)}$ species, with a sequential appearance of $Q^{(n-1)}$ species as the alkali content increases). This information has been valuable in testing thermodynamic models of alkali silicate glasses. A popular model, used in understanding the energetics and thermodynamic mixing properties of silicate melts and suggested as part of a mechanism for alkali ion transport in alkali silicate glasses [102, 103], involves the disproportionation equilibria between $Q^{(n)}$ species,



with corresponding disproportionation constant

$$k_n = [Q^{(n+1)}][Q^{(n-1)}]/[Q^{(n)}]^2. \quad (4.3.26)$$

The equilibrium constant for this disproportionation reaction ranges from $k_n=0$ to $k_3=0.375$, $k_2=0.439$, and $k_1=0.311$ [104, 105]. For an equilibrium constant closer to zero the distribution of $Q^{(n)}$ is considered binary while higher values indicate a more random distribution.

Although ^{29}Si MAS NMR and this thermodynamic model have been used to predict reasonable activation energies for ionic transport, the ^{29}Si MAS derived k_n values are obtained by fitting heavily overlapping lines whose detailed shapes are unknown, and could be severely biased by the commonly made assumption that the MAS NMR lineshapes are Gaussian. While the ^{29}Si MAS NMR spectra are partially resolved in the case of alkali silicate glasses, the situation is much worse for binary alkaline earth silicates where the ^{29}Si MAS spectra are often completely unresolved, presumably because of greater disorder. Previous studies conducted in this group have focused on better resolving multiple sites using MAF. We first demonstrated its accuracy and

precision in a well-understood sodium silicate binary composition obtaining a value of $k_3 = 0.0129 \pm 0.0001$ [106]. Similar values have also been obtained for a potassium disilicate glass, which indicate a binary distribution for alkali silicate glasses ($k_3 = 0.0103 \pm 0.0008$) [95], which is consistent with previous studies [107–109]. Other studies utilizing this approach on CaSiO_3 glass, which has a completely unresolved ^{29}Si MAS spectrum, we obtained for the first time the equilibrium constants $k_1 = 0.105 \pm 0.019$, $k_2 = 0.156 \pm 0.005$, and $k_3 = 0.106 \pm 0.022$ for the disproportionation reactions in CaSiO_3 [110]. These results clearly indicate a significantly greater deviation from a binary model of $\text{Q}^{(n)}$ species disproportionation in alkaline earth silicate melts when compared to alkali silicate melts and thus suggest a relatively more disordered structure.

While previous studies have utilized 2D PASS spectra to qualitatively analyze crystalline and disordered materials for different $\text{Q}^{(n)}$ a full quantitative analysis has been lacking. To determine if 2D PASS can be used to quantify $\text{Q}^{(n)}$ in an amorphous glass whose 1D NMR spectrum is completely unresolved we compare relative concentrations of $\text{Q}^{(n)}$ -species in a ^{29}Si -enriched potassium disilicate glass reported in a previous work [95] to those obtained by fitting a ^{29}Si 2D PASS NMR spectrum of the same material. A 3 ppm difference in ζ ($\sigma_{33} - \sigma_{iso}$) was observed for $\text{Q}^{(3)}$ (-77.8 ppm) and $\text{Q}^{(2)}$ (-88.9 ppm) between 2D PASS experiments presented in this work and previous MAF studies [95] attributed to differences in experimental conditions (spinning speed, angular dependencies, etc.), while η values were consistent ($\eta = 0.08$ and 0.46 for $\text{Q}^{(3)}$ and $\text{Q}^{(2)}$ respectively). For $\text{Q}^{(4)}$ ζ and η were set to zero. Spectra were fit using a 2D fitting routine utilizing the NMR simulation package SIMPSON [111] and the Levenberg-Marquardt algorithm built into the Optimization toolbox of Matlab. In this way, the full 2D spectrum could be fit and relative concentrations of each $\text{Q}^{(n)}$ -species obtained. This procedure was employed to fit the ^{29}Si 2D PASS (Figure 4.6a)

and 2D PASS CPMG (Figure 4.6b) spectra of the ^{29}Si -enriched potassium disilicate glass and the relative areas used to reconstruct a 1D lineshape to easily visualize the relative contributions of each $\text{Q}^{(n)}$ -species to the full 2D spectrum (Figure 4.7a and b, Table 4.1).

The measured concentrations from 2D PASS and 2D PASS CPMG are within 2 % of the previously reported k_3 from MAF (Table 4.1), indicating that 2D PASS can be utilized similar to MAF to quantify $\text{Q}^{(n)}$ -species in silicate glasses. Since the 2D PASS technique can be performed on a standard MAS probe by spinning at a fixed angle this should offer a significant time savings over variable angle experiments allowing these experiments to be more readily performed in most NMR labs.

Having determined that 2D PASS can provide complimentary information to MAF and that similar concentrations for each $\text{Q}^{(n)}$ -species can be obtained using both techniques, 2D PASS CPMG was then used to analyze $\text{K}_2\text{O} \cdot 2.2\text{SiO}_2$ with ^{29}Si in natural abundance. Utilizing the ^{29}Si 2D PASS CPMG sequence and the previously described 2D data fitting routine the total 2D spectrum was fit (Figure 4.6 and the relative concentrations of each $\text{Q}^{(n)}$ site obtained (Figure 4.7c, Table 4.2). The measured concentrations for each $\text{Q}^{(n)}$ were within 2 % of the concentrations from the enriched glass (Table 4.2). However, there was a distinguishable difference in peak position and width. This difference is attributed to the difference in composition between the two sample. For the enriched sample, the ratio of $\text{SiO}_2:\text{K}_2\text{O} = 2$ while for the natural abundance sample $\text{SiO}_2:\text{K}_2 = 2.2$. The samples also had different thermal histories (quenched rate, melt temperature, etc.) leading to different structure in the quenched glass.

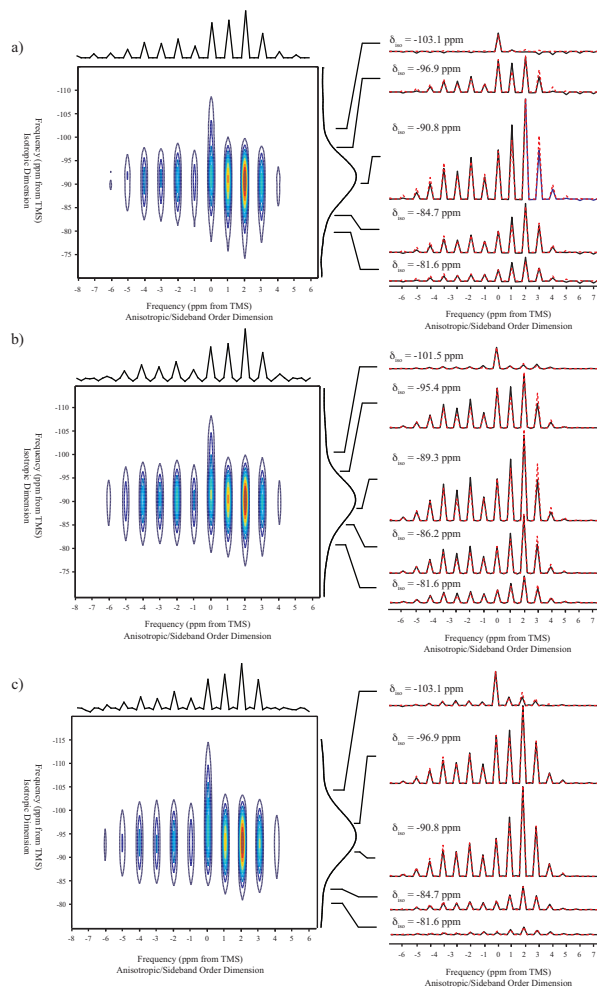


Figure 4.6: The ^{29}Si a) 2D PASS NMR spectrum of the ^{29}Si -enriched potassium disilicate glass, b) 2D PASS CPMG NMR spectrum of the ^{29}Si -enriched potassium disilicate glass, and c) 2D PASS CPMG NMR spectrum of the potassium disilicate glass with silicon in natural abundance. Representative cross sections along the sideband dimension are provided where solid lines represent experimental spectra and dashed lines represent the least-squares fit simulation.

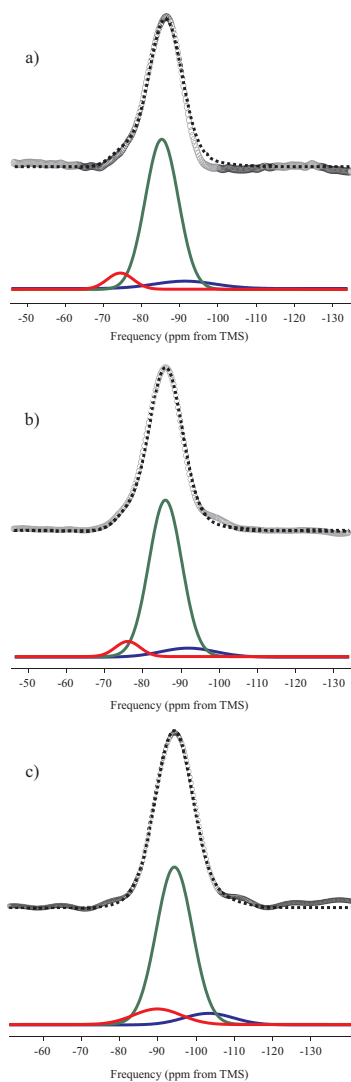


Figure 4.7: Reconstructed 1D lineshape from the deconstruction of the a) 2D PASS NMR spectrum of the ^{29}Si -enriched potassium disilicate glass, b) 2D PASS CPMG NMR spectrum of the ^{29}Si -enriched potassium disilicate glass, and c) 2D PASS CPMG NMR spectrum of the potassium disilicate glass with silicon in natural abundance. Each of the three Gaussians represent the relative contributions from $\text{Q}^{(2)}$, $\text{Q}^{(3)}$, and $\text{Q}^{(4)}$, circles represent the 1D projection along the MAS dimension, and dashed lines are the total least squares best fit.

Site	Relative Area	Mean Position/ppm	Standard Deviation/ppm
MAS [†]			
$Q^{(2)}$	$41.6 \pm 3.3\%$	-87.55 ± 0.11	5.15 ± 0.03
$Q^{(3)}$	$57.7 \pm 2.7\%$	-92.24 ± 0.02	3.88 ± 0.01
$Q^{(4)}$	$0.7 \pm 4.7\%$	-104.83 ± 0.10	1.92 ± 0.08
MAF [†]			
$Q^{(2)}$	$9.8 \pm 0.7\%$	-82.74 ± 0.03	3.27 ± 0.03
$Q^{(3)}$	$83.0 \pm 0.1\%$	-91.32 ± 0.01	4.19 ± 0.01
$Q^{(4)}$	$7.2 \pm 0.3\%$	-101.67 ± 0.02	5.09 ± 0.03
2D PASS			
$Q^{(2)}$	$8.7 \pm 0.2\%$	-79.7 ± 0.2	3.89 ± 0.09
$Q^{(3)}$	$84.5 \pm 0.2\%$	-90.6 ± 0.2	4.43 ± 0.02
$Q^{(4)}$	$6.6 \pm 0.1\%$	-98.0 ± 0.1	7.73 ± 0.09
2D PASS CPMG			
$Q^{(2)}$	$10.03 \pm 0.3\%$	-82.1 ± 0.1	4.23 ± 0.09
$Q^{(3)}$	$82.65 \pm 0.3\%$	-90.9 ± 0.1	4.35 ± 0.03
$Q^{(4)}$	$7.32 \pm 0.1\%$	-98.1 ± 0.1	7.11 ± 0.09

Table 4.1: Gaussian distribution parameters of isotropic chemical shifts of $Q^{(n)}$ -species in ^{29}Si -enriched $\text{K}_2\text{O} \cdot 2\text{SiO}_2$ derived from analysis of ^{29}Si MAS[†], ^{29}Si MAF[†], ^{29}Si 2D PASS, and ^{29}Si 2D PASS CPMG spectra, where [†] indicates experimental results reported in a previous work [95].

Site	Relative Area	Mean Position /ppm	Standard Deviation /ppm
2D PASS CPMG			
$Q^{(2)}$	$10.69 \pm 0.26\%$	-88.9 ± 0.16	6.31 ± 0.14
$Q^{(3)}$	$81.04 \pm 0.21\%$	-93.4 ± 0.1	4.75 ± 0.01
$Q^{(4)}$	$8.28 \pm 0.03\%$	-102.5 ± 0.1	6.61 ± 0.03

Table 4.2: Gaussian distribution parameters of isotropic chemical shifts from ^{29}Si 2D PASS CPMG NMR for $Q^{(n)}$ -species in natural abundance $\text{K}_2\text{O} \cdot 2.2\text{SiO}_2$.

4.4 Summary

We have demonstrated that a rotor synchronized CPMG acquisition can be successfully added to the 2D PASS NMR experiment to obtain significant sensitivity enhancement (1.9x) over the 2D PASS experiment proposed by Antzutkin et al. [4]. While only even acquired echoes were observed to appropriately satisfy the PASS equations, a Cogwheel phase cycle has been developed to selectively acquire even echoes while eliminating the effects of unwanted frequency components from spurious coherence pathways. Additionally, for the first time, we have successfully used 2D PASS with and without CPMG acquisition to quantify $Q^{(n)}$ -species in a silicate glass. Having demonstrated that 2D PASS CPMG will provide sufficient sensitivity enhancement to analyze modified silicate glasses in natural abundance, $Q^{(n)}$ -species distributions were determined for an unenriched glass of similar composition. The overall sensitivity enhancement from this experiment is dependent upon the relaxation time T_2 , which determines the number of possible echoes. From samples reported in this work the highest sensitivity enhancement obtained from 2D PASS CPMG is 1.9x compared to the traditional 2D PASS experiment.

CHAPTER 5

CORRELATION OF ANISOTROPIC INTERACTIONS FOR INTEGER SPIN NUCLEI

5.1 Introduction

Solid state nuclear magnetic resonance (NMR) lineshapes of integer spin nuclei are complicated because of the anisotropic components of chemical shift / paramagnetic shift, dipolar, and quadrupolar interactions. In the principal axis system three parameters, isotropic chemical shift (δ_{iso}), the anisotropic chemical shift (ζ), and asymmetry parameter (η), are sufficient to fully characterize the chemical shift tensor. Since the quadrupolar tensor is traceless, two parameters, the quadrupolar coupling constant (C_q), and quadrupolar asymmetry parameter (η_q) are sufficient to fully describe the quadrupolar tensor. When both interactions are simultaneously present, relative orientations of the two principle axis system are needed to completely characterize the local atomic environment. Accurate determination of quadrupolar interactions, chemical shift interactions, and their relative orientation from fitting a 1D NMR spectrum of a polycrystalline spin-1 sample is an ill-posed problem and can lead to inaccurate values with large associated errors. Recent 2D NMR studies have been able to separate quadrupolar and chemical shift dimensions along two orthogonal axis in both integer spin [1] and half integer nuclei [68].

Typically, the first order correction to the anisotropic components of the NMR

frequencies are averaged by magic angle spinning (MAS) but the second order correction does not. For integer spin nuclei with small quadrupolar couplings constants, the situation is simplified since a first order approximation of the quadrupolar Hamiltonian is sufficient to describe the observed lineshape. Since the quadrupolar coupling of integer spin nuclei determined from static solid-state NMR spectra is a sensitive probe of local environment, it is commonly studied to understand binding and mobility [112–114].

While the quadrupolar interaction is dominant in diamagnetic materials, in paramagnetic solids the magnitude of the chemical shift interaction becomes significant. Initial studies to selectively observe chemical shift components while eliminating quadrupolar contributions by Vega et al. [115] and Muller [116] used a double quantum excitation of the $m = 1$ to $m = -1$ transition. Due to symmetric nature of double quantum transition, the double quantum coherence does not evolve under the influence of first order quadrupolar coupling and is only influenced by chemical shift/paramagnetic shift interactions. This concept has been further developed into a series of experiments that correlate quadrupolar and chemical shift interactions using either a double quantum evolution or exploiting the spatial dependence of NMR interaction Hamiltonian [117–119]. Interestingly, in all the recent publications the correlation of quadrupolar and chemical shift interaction by double quantum excitation is achieved through a series of 90° pulses, which seriously impair the excitation efficiency leading to distorted spectra [1].

Most recently, Antonijevic and Wimperis [1] have introduced a single quantum three pulse echo sequence that separates chemical/paramagnetic and quadrupolar interactions along two orthogonal dimensions in static samples. The sequence proposed by Antonijevic and Wimperis [1] utilizes selective phase cycling to manipulate the phase evolution of the spin system to selectively refocus the quadrupolar and chemical

shift components at different times during the experiment. Applying the appropriate shearing transform will yield a two dimension spectrum with a pure quadrupolar and pure chemical shift dimension.

In this study we present an alternative pulse sequence to that proposed by Antonijevic and Wimperis [1]. Utilizing selective phase cycling in a shifted echo **d**-echo sequence, the quadrupolar and chemical shift interactions are refocused at different times during the experiment. A two times sensitivity gain is observed over the Antonijevic and Wimperis [1] sequence. A formalism is also discussed to predict how different interactions are refocused during the experiment [1].

5.2 Experimental

5.2.1 ^2H NMR

NMR experiments were performed using a 2 mm Bruker static probe interfaced to a Bruker Avance spectrometer operating at a field strength of 9.4 T (corresponding to a resonance frequency of 61.491912 MHz for ^2H). Following the treatment by Vega et al. [115] the two pulse double quantum experiment (Figure 5.1a) utilized an initial soft pulse to excite the double quantum transition and a hard second pulse for conversion of the multiple quantum coherence to single quantum. For single quantum experiments (Figure 5.1b and c) a radio frequency field strength of 140 kHz was used and pulse lengths were calibrated on the solid sample to minimize pulse imperfections. A sweep width of 500 kHz and 250 kHz was used in the direct and indirect dimension, respectively.

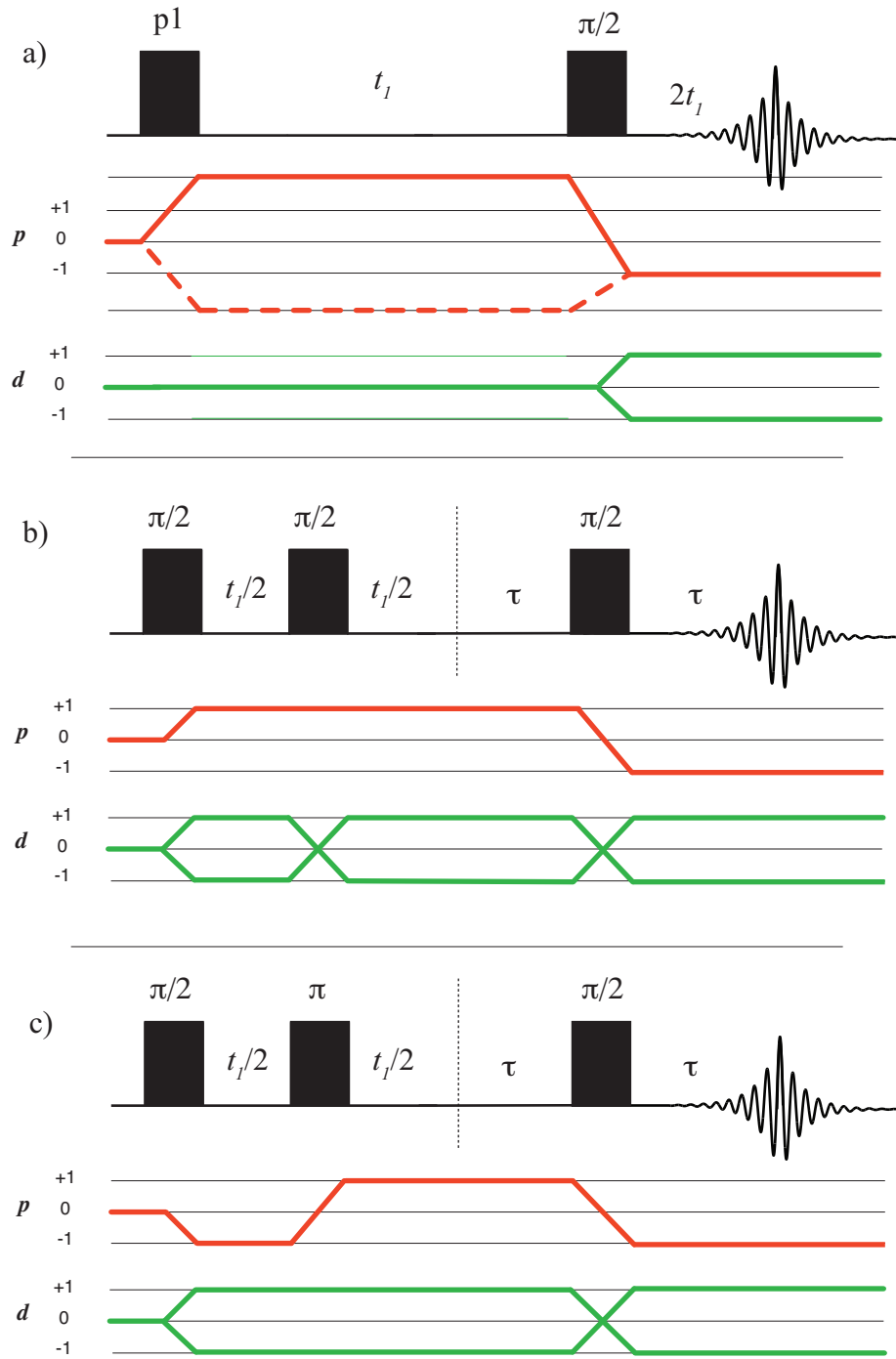


Figure 5.1: a) Double quantum pulse sequence. (b) d -echo experiment proposed by Wimperis. (c) p -echo experiment proposed in this study. (Here, we define $\mathbf{p} = m_j - m_i$ and $\mathbf{d} = m_j^2 - m_i^2$)

5.2.2 Sample Preparation

A sample of deuterated copper chloride ($\text{CuCl}_2 \cdot 2\text{D}_2\text{O}$) was prepared using the method outlined in Antonijevic and Wimperis [1] by dissolving 5 g CuCl_2 in 5 mL of D_2O . The CuCl_2 was dried at 120 °C for two hours. The sample was allowed to dry and carefully monitored to ensure that the sample did not have prolonged exposure to the atmosphere. Blue-green crystals were observed to form after several hours. The recovered sample was then packed in a nitrogen glove box and stored in a desiccator to prevent exposure to moisture. Deuterated hexamethyl bromide (DHMB) was obtained commercially (Sigma Aldrich) and used without further purification.

5.3 Results and Discussion

Contributions to the NMR lineshape can be separated by manipulating either the spin or spatial degrees of freedom. Using a condensed formalism, the frequency domain signal is represented as the sum of its individual components

$$\Omega_k(i, j) = \omega_k \cdot \Xi(\Omega) \cdot \xi_k(i, j). \quad (5.3.1)$$

where ω is a scaling factor that represents the strength of component k , Ξ contains the spatial component, ξ contains the spin component, and i and j are the eigenstates of the stationary state Hamiltonian that govern a given transition. Total Hamiltonian for a $I = 1$ system can be written as,

$$\hat{H} = \hat{H}_{cs} + \hat{H}_q, \quad (5.3.2)$$

where \hat{H}_q is the quadrupolar Hamiltonian, and \hat{H}_{cs} is the chemical shielding Hamiltonian. Using the first order perturbation correction of the nuclear shielding Hamiltonian, we can write the first-order nuclear shielding contribution to the $|i\rangle \rightarrow |j\rangle$ transition frequency as

$$\boxed{\Omega_\sigma^{(1)} = -\omega_0 \sigma_{iso} [\mathbf{S}^{\{\sigma\}} \cdot \mathbb{P}_I] - \omega_0 \zeta_\sigma [\mathbf{D}^{\{\sigma\}} \cdot \mathbb{P}_I].} \quad (5.3.3)$$

where

$$\mathbf{S}^{\{\sigma\}} = -\frac{1}{\sigma_{iso}} \sqrt{\frac{1}{3}} R_{0,0}^{\{\sigma\}}, \quad \mathbf{D}^{\{\sigma\}} = \frac{1}{\zeta_\sigma} \sqrt{\frac{2}{3}} R_{2,0}^{\{\sigma\}}, \quad (5.3.4)$$

and

$$\mathbb{P}_I = \langle I, m_j | \hat{T}_{1,0}^\circ(\mathbf{I}) | I, m_j \rangle - \langle I, m_i | \hat{T}_{1,0}^\circ(\mathbf{I}) | I, m_i \rangle = m_j - m_i. \quad (5.3.5)$$

The first-order quadrupolar contribution to the transition frequency between levels i and j is given by

$$\boxed{\Omega_q^{(1)} = \omega_q [\mathbf{D}^{\{q\}} \cdot \mathbb{d}_I],} \quad (5.3.6)$$

where

$$\mathbf{D}^{\{q\}} = \frac{1}{3\zeta_q} R_{2,0}^{\{q\}}, \quad (5.3.7)$$

and

$$\mathbb{d}_I = \langle I, m_j | \hat{T}_{2,0}^\circ(\mathbf{I}) | I, m_j \rangle - \langle I, m_i | \hat{T}_{2,0}^\circ(\mathbf{I}) | I, m_i \rangle = \sqrt{\frac{2}{3}} (m_j^2 - m_i^2). \quad (5.3.8)$$

Hence, the total transition frequency between energy level i and j (considering only first order correction) can be written as

$$\Omega^1 = -\omega_0 \sigma_{iso} [\mathbf{S}^{\{\sigma\}} \cdot \mathbb{P}_I] - \omega_0 \zeta_\sigma [\mathbf{D}^{\{\sigma\}} \cdot \mathbb{P}_I] + \omega_q [\mathbf{D}^{\{q\}} \cdot \mathbb{d}_I]. \quad (5.3.9)$$

To separate contributions from chemical shift and quadrupolar coupling either the spin or the spatial components must be manipulated to selectively refocus either

quadrupole or chemical shift interactions. Equation 5.3.9 indicates that for nuclei where $I = 1$ both the quadrupolar and chemical shift have identical spatial components but have different spin components. Therefore, quadrupole and chemical shift interactions cannot be separated by manipulating the spatial components (\mathbf{D}) of equation 5.3.9 (i.e. changing rotor orientation or spinning speed) but can only be separated by manipulating the spin degrees of freedom (contributions from \mathbf{p} and \mathbf{d}). Commonly, when describing the coherence transfer pathway for a pulse sequence only the \mathbf{p} pathway is reported. However, as indicated by Antonijevic and Bodenhausen [120] when the frequency has a significant contribution from the quadrupolar components of equation 5.3.6, following the \mathbf{p} pathway alone is not satisfactory and other terms must be considered. For instance, when examining a typical two pulse \mathbf{d} echo sequence of $90^\circ\text{-}\tau\text{-}90^\circ\text{-}\tau\text{-}\text{acquire}$, examination of the \mathbf{p} pathway alone indicates that an echo will not form since the sign of \mathbf{p} does not change over the course of the experiment. However, since signal is observed another contribution from a second pathway must exist. This was explained by Antonijevic and Bodenhausen [120] by following the \mathbf{q} pathway and observing that \mathbf{q} changes sign from +1 to -1 after the application of the second pulse leading to an echo at time 2τ .

5.3.1 Double Quantum

Chemical shift interactions and quadrupolar interactions can also be separated using a double quantum (DQ) as opposed to a single quantum evolution period. Vega et al. [115] observed that the perturbation to the overall Zeeman Hamiltonian because of the first order quadrupolar interaction symmetrically shifts the $m = 1$ and $m = -1$ substates. Therefore, by exciting from $m = -1$ to $m = +1$ and allowing the double quantum coherence to evolve during t_1 before detection, a spectrum devoid of first order quadrupolar broadening is obtained along t_1 dimension. For maximum

efficiency in a two-pulse DQ experiment, an initial soft pulse is applied to excite the DQ transition along the \mathbf{p} pathway and following an evolution time t_1 , a hard 90° pulse is applied for conversion (Figure 5.1a). Since the \mathbf{p} pathway evolves during t_1 , a \mathbf{p} echo should be observed at time $2t_1$ in the FID (Figure 5.2a). The \mathbf{d} pathway is also present during the experiment but is not excited by the initial soft pulse and remains zero during the evolution period (ie. during t_1 there is only evolution under chemical shift). The hard 90° pulse does excite the \mathbf{d} pathway but since \mathbf{d} does not change sign but goes from 0 to ± 1 an echo will not be observed. Instead the \mathbf{d} pathway will be detected directly in the time domain (Figure 5.2a). To obtain purely absorptive lineshapes the 2 pulse double quantum sequence can be combined with hypercomplex data acquisition. After the 2D dataset is properly sheared (Figure 5.2b), a 2D FT of dataset will have two orthogonal dimensions corresponding to quadrupolar components only along the direct and CSA components along the indirect dimensions (Figure 5.2). While effective for nuclei with moderate ω_q , the two pulse double quantum pulse sequence is limited by the high rf fields ($\omega_1 \gg \omega_q$) required for proper conversion of $\mathbf{p} = +2$ to $\mathbf{p} = -1$. Therefore, for nuclei with small ω_q , the power levels needed for conversion of the full lineshape (150 kHz) are fully met by conventional NMR hardware but are inadequate for nuclei with significantly broad lineshapes, which will appear distorted along both dimensions (Figure 5.3). Taking the projection of each along the direct and indirect dimensions indicates that for DHMB a well defined quadrupolar lineshape is observed along the direct dimension and a CSA powder pattern along the indirect dimension while the projections for the $\text{CuCl}_2 \cdot \text{D}_2\text{O}$ are not well resolved.

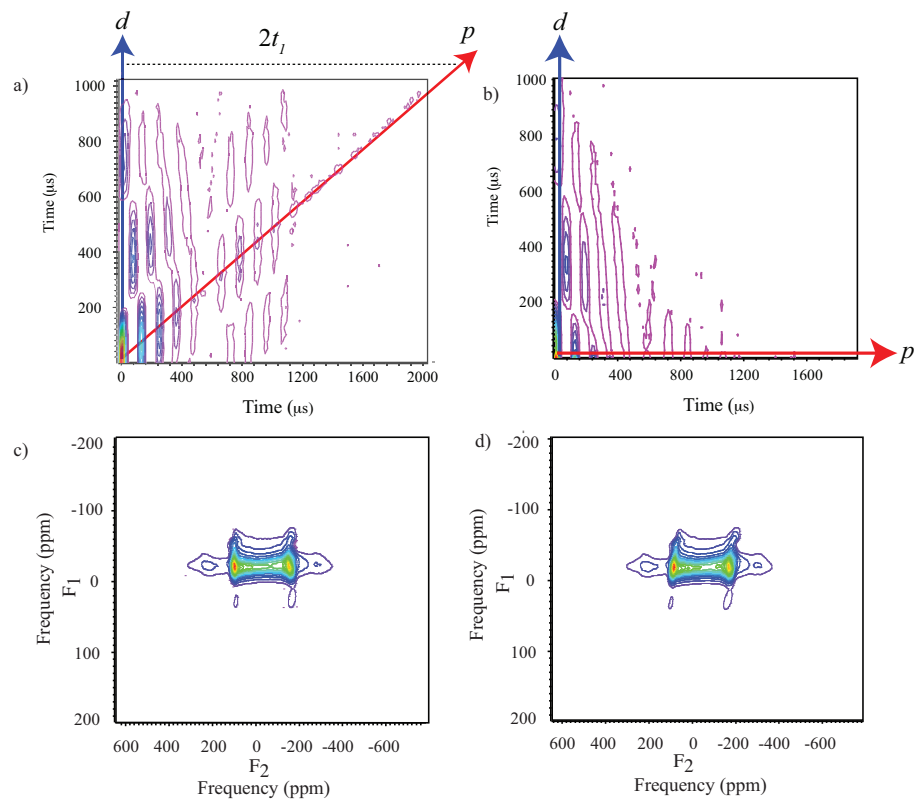


Figure 5.2: (a) Unsheared time domain ^2H DQ signal of DHMB. (b) Sheared time domain data (c) 2DFT of (a). (d) 2DFT of (b).

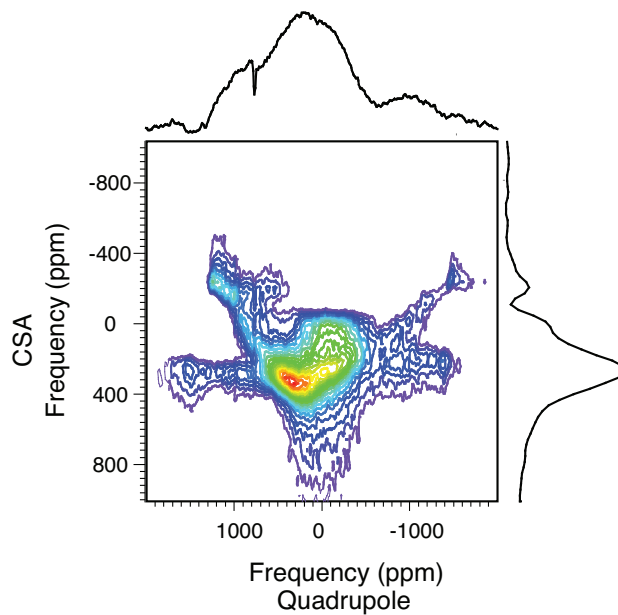


Figure 5.3: 2D Double quantum experimental spectrum of ^2D in $\text{CuCl}_2 \cdot 2\text{D}_2\text{O}$.

5.3.2 3-pulse **d** Echo Experiment

In the **d**-echo experiment proposed by Antonijevic and Wimperis [1] (Figure 5.1b) the application of a series of 90° pulses successfully refocuses the **d** pathway while selective phase cycling ensures the **p** pathway remains invariant after the application of the second 90° pulse during the evolution time t_1 . Application of the third 90° pulse then refocuses the **p** pathway into an observable echo.

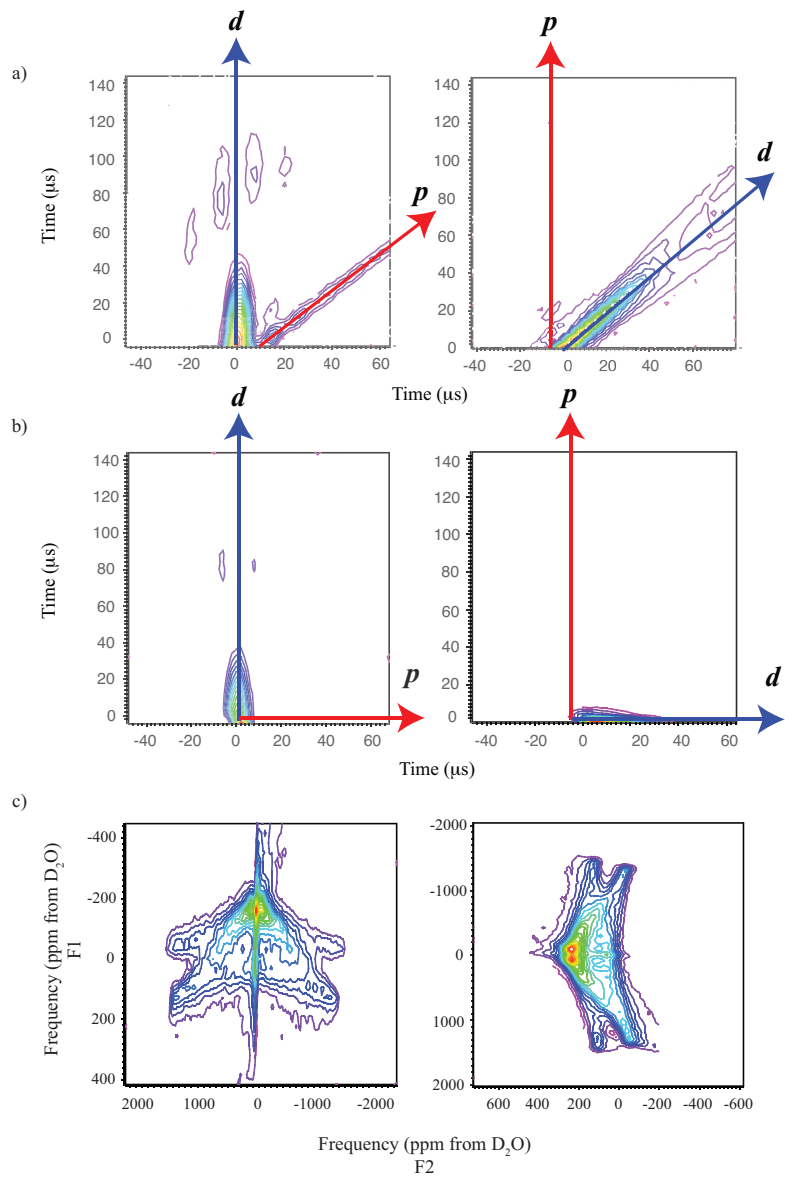


Figure 5.4: ^2H NMR time domain spectrum from the experiment proposed in a) Antonijevic and Wimperis [1] (left) and the sequence from this study (right), b) the sheared time domain data, and c) the 2D frequency domain spectrum.

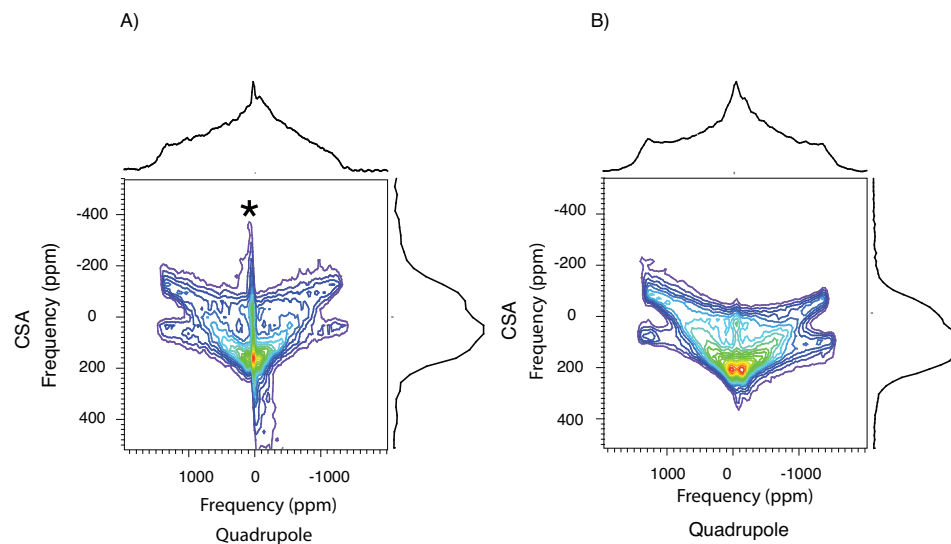


Figure 5.5: A) Two dimensional sheared spectrum of ^2D NMR from three pulse **d**-echo experiment with separated quadrupolar and CSA dimensions. The pulse imperfection causes unwanted line in 2D spectrum marked by *. B) Two dimensional sheared spectrum of ^2D NMR using three pulse **p**-echo experiment with separated quadrupolar and CSA dimensions. Both spectra are taken under using same number of scan and same pulse calibrations.

In this study we use an alternative formalism to that used by Antonijevic and Bodenhausen [120] based on symmetry and similarly follows the evolution of multiple coherence pathways (Figure 5.1). The initial 90° pulse excites the **p** pathway to $+1$ and the **d** pathway to ± 1 . After the second 90° pulse the **p** pathway remains invariant and evolves during time t_1 . In contrast, the **d** pathway is refocused after the application of the second pulse to ∓ 1 and by using a split- t_1 evolution time, **d** evolution is cancelled. After a time $t_1/2$ a **d** echo is formed, which is refocused after time τ and then detected. Since the spin evolution for **p** and **d** pathways differ during t_1 , the two pathways can be separated from each other. This effect is observed in the acquired FID since the **d** pathway, which is not evolving in t_1 will be shifted to a fixed time τ and the echo appears static in t_1 (Figure 5.4). In contrast, the **p** pathway does evolve and is observed in the FID at t_1 plus τ . Therefore, in the time domain data from the pulse sequence proposed by Antonijevic and Wimperis [1] two echoes are observable, one assigned to **p** and the other assigned to **d** (Figure 5.4). Since contributions from **p** and **d** are present, a 2D Fourier transform and proper shearing of the 2D data set will yield a frequency domain spectrum that contains a pure quadrupolar dimension along F_2 and a pure chemical shift dimension along F_1 (Figure 5.6).

5.3.3 3-pulse **p** echo sequence

An alternative sequence to **d**-echo sequence proposed by Wimperis et.al [1] is presented by replacing the second 90° with a 180° pulse to refocus the **p** pathway while leaving the **d** pathway invariant (Figure 5.1c). The **d** pathway is invariant under the application of a 180° pulse while the **p** pathway is refocused. Opposite to the sequence proposed by Antonijevic and Wimperis [1], in the 3-pulse **d** echo sequence the **p** pathway evolves during t_1 while the **d** pathway is invariant. The **d** echo should then shift

out in time as a function of t_1 along the indirect dimension while the \mathbf{p} pathway is shifted to a constant time τ (Figure 5.4). Upon Fourier transform a mixed dimension is observed in both dimensions that is influenced by both quadrupolar and chemical shift contributions. After proper shearing and Fourier transformation a 2D dataset with a pure quadrupolar dimension along F1 and a pure chemical shift dimension along F2 is observed (Figure 5.6). A 2 times signal enhancement was observed over the 3-pulse \mathbf{d} -echo experiment attributed to the improved ability of the 180° pulse to refocus the magnetization after time t_1 . This can be explained using spherical tensor operator formalism in Antonijevic and Bodenhausen [120] by expanding the density operator as

$$\sigma(t) = \sum_{l=0}^{2l} \sum_{p=-l}^l b_{l,p}(t) T_{l,p} \quad (5.3.10)$$

where $T_{l,p}$ is the irreducible spherical tensor operator of rank l and coherence order \mathbf{p} . Under the influence of a hard radiofrequency pulse with flip angle β and phase ϕ , the irreducible spherical tensor operator transforms so that

$$T_{l,p} \xrightarrow{\beta\phi} \sum_{p'=-l}^l T_{l,p'} d_{p',p}^l(\beta) \exp(-i\Delta p\phi) \quad (5.3.11)$$

where p' is the new coherence order, Δp is the change in coherence order. Following an initial hard 90_x° pulse, the density operator can be written

$$\sigma(0) = -i[T_{1,-1} + T_{1,+1}] = -I_y. \quad (5.3.12)$$

The density matrix then evolves for a variable time τ in the rotating frame under the offset Hamiltonian

$$\mathcal{H}_{off} = \Omega I_z$$

and the first order quadrupolar Hamiltonian

$$\mathcal{H}_{quad} = \omega_q \left(I_z^2 - \frac{I(I+1)}{3} \right)$$

such that

$$\begin{aligned}
\sigma(0) &= -I_y = -i[T_{1,-1} + T_{1,+1}] \\
&\xrightarrow{\Omega\tau} -i[T_{1,-1} \exp(i\Omega\tau) + T_{1,+1} \exp(-i\Omega\tau)] \\
&\xrightarrow{\omega_q\tau} -i[T_{1,-1} \cos \omega_q\tau + iT_{2,-1} \sin \omega_q\tau] \exp(i\Omega\tau) \\
&\quad + [T_{1,+1} \cos \omega_q\tau - iT_{2,+1} \sin \omega_q\tau] \exp(-i\Omega\tau)
\end{aligned}$$

For the three pulse **d**-echo experiment

$$\begin{aligned}
&\xrightarrow{90_x} -i\left[\left(\frac{1}{2}T_{1,+1} \cos \omega_q\tau - \frac{i}{2}T_{2,+1} \sin \omega_q\tau\right) \exp(i\Omega\tau)\right. \\
&\quad \left. + \left(\frac{1}{2}T_{1,+1} \cos \omega_q\tau - \frac{i}{2}T_{2,+1} \sin \omega_q\tau\right) \exp(-i\Omega\tau)\right] \\
&\xrightarrow{\Omega\tau} -\frac{i}{2}\left[(T_{1,+1} \cos \omega_q\tau - iT_{2,+1} \sin \omega_q\tau) \exp(i2\Omega\tau)\right. \\
&\quad \left. \xrightarrow{\omega_q\tau} -\frac{i}{2}(T_{1,-1} \cos^2 \omega_q\tau + iT_{2,-1} \sin \omega_q\tau \cos \omega_q\right. \\
&\quad \left. \tau - iT_{2,-1} \sin \omega_q\tau - q\tau \cos \omega_q\tau + T_{1,-1} \sin^2 \omega_q\tau) \exp(i2\Omega\tau)\right]
\end{aligned}$$

which reduces to

$$\sigma(2\tau) = -\frac{i}{2}T_{1,-1} \exp(i2\Omega\tau) \quad (5.3.13)$$

After a second evolution time τ a 90° pulse is applied and the density matrix becomes

$$\xrightarrow{\Omega\tau} -\frac{i}{2}\left[(T_{1,+1} \cos \omega_q\tau - iT_{2,+1} \sin \omega_q\tau) \exp(i2\Omega\tau)\right] \quad (5.3.14)$$

Similar values are calculated for the **d** echo experiment. Since the only differences between the **d**-echo and **p**-echo experiments are the phase cycle and the length of the

second pulse the results can be modeled around a two pulse experiment. Following from Equation 5.3.14

$$\begin{aligned}
& \xrightarrow{180_x} -i[-T_{1,+1} \cos \omega_q \tau + iT_{2,+1} \sin \omega_q \tau] \exp(i\Omega\tau) \\
& + i[-T_{1,-1} \cos \omega_q \tau - iT_{2,-1} \sin \omega_q \tau] \exp(-i\Omega\tau) \\
& \xrightarrow{\Omega\tau} -i[-T_{1,+1} \cos \omega_q \tau + iT_{2,+1} \sin \omega_q \tau] \\
& + i[-T_{1,-1} \cos \omega_q \tau - iT_{2,-1} \sin \omega_q \tau] \\
& \xrightarrow{\omega_q \tau} -i[(-T_{1,+1} \cos^2 \omega_q \tau + 2iT_{2,+1} \sin \omega_q \tau \cos \omega_q \tau \\
& + T_{1,+1} \sin^2 \omega_q \tau) \\
& + (-T_{1,-1} \cos^2 \omega_q \tau - 2iT_{2,-1} \sin \omega_q \tau \cos \omega_q \tau + T_{1,-1}
\end{aligned}$$

Keeping only detectable term

$$\sigma(2\tau) = i[T_{1,-1} \cos 2\omega_q \tau - T_{2,-1} \sin 2\omega_q \tau] \quad (5.3.15)$$

From Equations 5.3.13 and 5.3.15, it is observed that when τ is close to zero, the second term in Equation 5.3.15 will be zero and the sensitivity enhancement will be equal to twice that observed in the **d**-echo experiment.

Figure 5.5 shows the sensitivity gain of our **p** echo approach compared to the **d** echo approach. As **p** pathways can be phase cycled, so we have more control over the **p** echo experiment compared to the **d** echo experiment. Using same pulse length, pulse imperfection is observed in the **d** echo experiment (Figure 5.5), but no pulse imperfection is observed in our **p** echo experiment.

5.4 Conclusion

A 3-pulse **p**-echo sequence is presented. Similar to the Antonijevic [1] experiment, selective phase cycling is used to refocus quadrupolar and chemical shift components

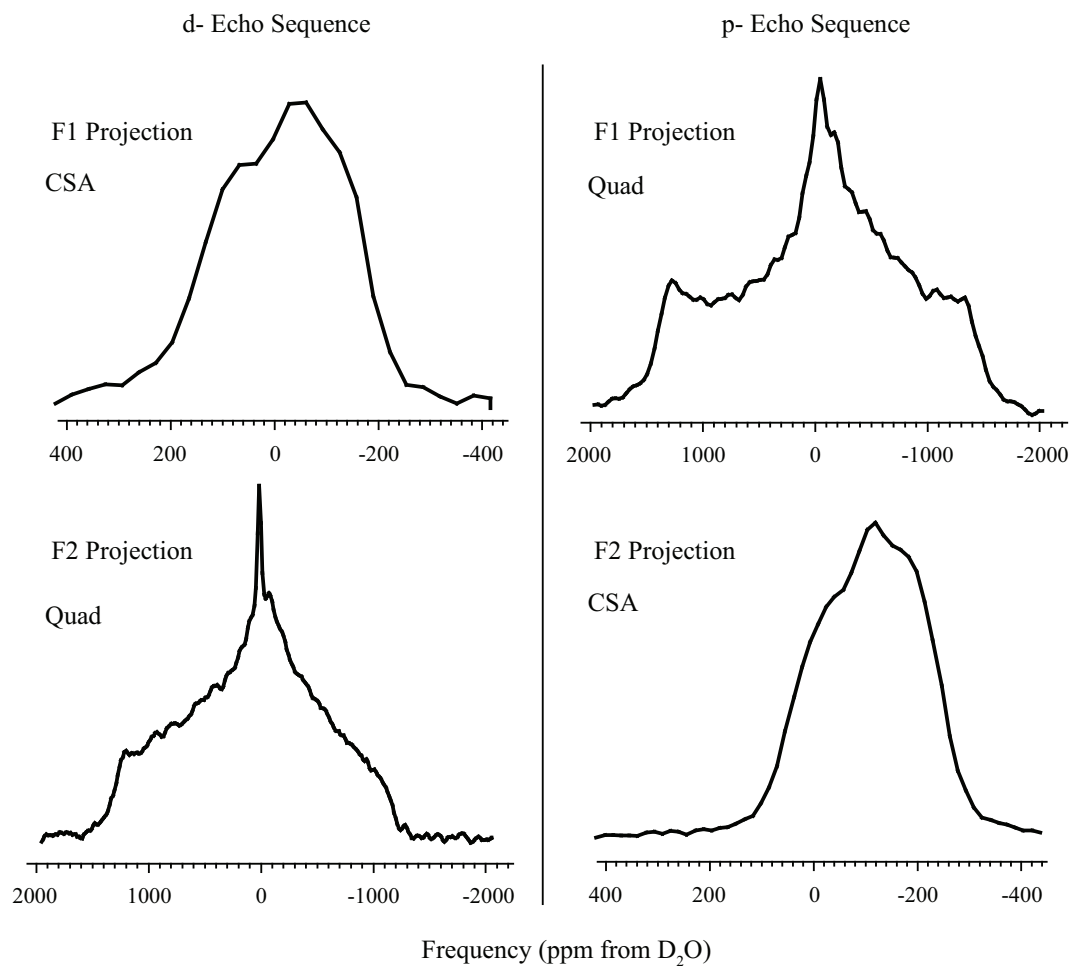


Figure 5.6: Projections taken along the F1 and F2 axis illustrating the opposite re-focusing of the *d*-echo and *p*-echo sequences.

at different times in the free induction decay. After the appropriate Affine transformation a 2D spectrum is obtained with quadrupolar and chemical shift components along two orthogonal dimensions. A two times improvement in sensitivity was observed that was corroborated by calculation. Three pulse **d**-echo experiment [1] is more vulnerable to the pulse imperfection than the proposed three pulse **p**-echo experiment. Using same pulse length, the pulse imperfections are visible in *d*-echo experiment, but not observed in our **p**-echo experiment. Additionally, a formalism is discussed that explains the reversal of the 3-pulse **p**-echo experiment presented in this work and the 3-pulse **d**-echo experiment.

Appendix A

A.1 Chapter 3

A.1.1 Periodic Signals and Sidebands

In this section we will consider the relationship between a periodic signal and the sideband pattern in its Fourier transform. First, we write a Fourier series expansion of the periodic signal according to

$$S_T(t) = \sum_{N=-\infty}^{\infty} A(N)e^{i2\pi Nt/T}, \quad (\text{A.1.1})$$

whose Fourier transform is

$$S_T(\omega) = \int_{-\infty}^{\infty} S_T(t)e^{-i\omega t} dt = \sum_{N=-\infty}^{\infty} A(N) \delta(2\pi N/T - \omega), \quad (\text{A.1.2})$$

where T is the signal period and $A(N)$ is the N th sideband in $S_T(\omega)$.

Next, we define $S_T(t)$ as a periodic extension of a signal, $S(t)$, defined only inside a period from $t = 0$ to T , according to

$$S_T(t) = \sum_{n=-\infty}^{\infty} S(t + nT), \quad (\text{A.1.3})$$

whose Fourier transform is

$$S_T(\omega) = \int_{-\infty}^{\infty} \left[\sum_{n=-\infty}^{\infty} S(t + nT) \right] e^{-i\omega t} dt. \quad (\text{A.1.4})$$

Performing a change in variables, defining $s = t + nT$ and $ds = dt$, we obtain

$$S_T(\omega) = \sum_{n=-\infty}^{\infty} \int_{-\infty}^{\infty} S(s)e^{-i\omega(s-nT)} ds. \quad (\text{A.1.5})$$

Since $S(t)$ is defined only inside a period from $t = 0$ to T we can redefine the integral limits, obtaining

$$S_T(\omega) = \sum_{n=-\infty}^{\infty} \left[\int_0^T S(s) e^{-i\omega s} ds \right] e^{in\omega T}. \quad (\text{A.1.6})$$

Equating the two expressions for the Fourier transform of $S_T(t)$:

$$A(N) \delta(2\pi N/T - \omega) = \left[\int_0^T S(s) e^{-i\omega s} ds \right] e^{in\omega T}, \quad (\text{A.1.7})$$

we obtain

$$A(N) = \int_0^T S(s) e^{-i2\pi Ns/T} ds, \quad (\text{A.1.8})$$

as the relationship between the N th sideband in $S_T(\omega)$ and the signal, $S(t)$, defined inside the period from $t = 0$ to T .

A.1.2 CPMG Signal

The CPMG signal arises from the two coherence transfer pathways shown in Fig. 3.1. Signal from a given pathway is detected only while its coherence level is $p = -1$.

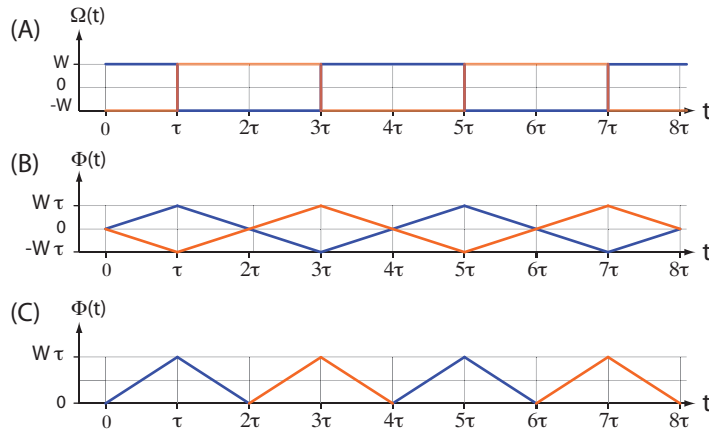


Figure A.1: (A) Time dependent frequency and (B) time dependent phase for the two pathway signals in the CPMG experiment. (C) The time dependent phase of the detected CPMG signal.

Both pathway signals experience a time dependent frequency with a period of 4τ , where 2τ is the CPMG π pulse spacing. As shown in Fig. A.1A, we can describe the time dependent frequencies for the two pathway signals as

$$\Omega_{\pm}(t) = \pm W(\alpha, \beta, \gamma) \text{Sq}(2\pi t/4\tau), \quad (\text{A.1.9})$$

where $\text{Sq}(x)$ is a square wave function, and 4τ is the cycle time of the frequency for the two pathway signals. As the integral of a square wave is a triangular wave, the signal phases for the two pathways, shown in Fig. A.1B, are given by

$$\Phi_{\pm}(t) = \pm W(\alpha, \beta, \gamma)\tau \text{Tg}(2\pi t/4\tau), \quad (\text{A.1.10})$$

where $\text{Tg}(x)$ is a triangle wave function. A CPMG echo occurs whenever the signal phase returns to zero. Since the signal from the two pathways are detected alternatively, the detected signal phase, shown in Fig. A.1C, is given by

$$\Phi(t) = W(\alpha, \beta, \gamma)\tau \left[\text{Tg}\left(\frac{2\pi t}{2\tau} - \pi\right) + 1 \right], \quad (\text{A.1.11})$$

which has a period of $T = 2\tau$. Thus, the detected CPMG signal inside the 0 to 2τ period is given by

$$S(t) = e^{-iW(\alpha, \beta, \gamma)(\tau - |t - \tau|)}. \quad (\text{A.1.12})$$

A.2 Chapter 4

A.2.1 Mapping and Coordination (Affine) Transformation

A multipole expansion of the NMR frequency written as a function of time can be separated into non-rotor and rotor modulated components:

$$\Omega(t, \phi_0) = \sum_{l=0}^{\infty} \omega_{l,0} + \sum_{l=1}^{\infty} \sum_{m \neq 0} \omega_{l,m} e^{im(\Omega_R t + \phi_0)},$$

where ϕ_0 is the initial rotor phase, and Ω_R is the rotor speed. In a one pulse NMR experiment the signal phase as function of t and ϕ_0 is

$$\begin{aligned}\Phi(t, \phi_0) &= \int_0^t \Omega(s) ds \\ &= W_0 t + \sum_{m \neq 0} W_m [e^{im(\Omega_R t + \phi_0)} - e^{im\phi_0}]\end{aligned}$$

where we have defined

$$W_0 = \sum_{l=0}^{\infty} \omega_{l,0} \quad \text{and} \quad W_m = \sum_{l=1}^{\infty} \frac{\omega_{l,m}}{im\Omega_R}.$$

From the signal phase the signal is derived (see derivation)

$$S(t, \phi_0) = e^{iW_0 t} \sum_{N_1, N_2} A_{N_1} A_{N_2}^* e^{-iN_1 \Omega_R t} e^{i(N_2 - N_1) \phi_0}.$$

This one-dimensional time domain signal can be mapped into a two-dimensional signal of rotor pitch and time by defining

$$\Theta' = \Omega_R t \quad \text{and} \quad t' = t - \Theta' / \Omega_R, \quad (\text{A.2.1})$$

to obtain

$$\begin{aligned}S(t', \Theta', \phi_0) &= e^{iW_0(t' + \Theta' / \Omega_R)} \\ &\times \sum_{N_1, N_2} A_{N_1} A_{N_2}^* e^{-iN_1 \Theta'} e^{i(N_2 - N_1) \phi_0}.\end{aligned}$$

If we then apply an affine transformation where

$$\begin{pmatrix} t \\ \Theta \end{pmatrix} = \begin{pmatrix} 1 & 1/\Omega_R \\ 0 & 1 \end{pmatrix} \begin{pmatrix} t' \\ \Theta' \end{pmatrix}, \quad (\text{A.2.2})$$

then the signal is transformed into

$$S(t, \Theta, \phi_0) = \sum_{N_1, N_2} A_{N_1} A_{N_2}^* e^{iW_0 t} e^{-iN_1 \Theta} e^{i(N_2 - N_1) \phi_0}. \quad (\text{A.2.3})$$

This is our starting equation for studies of single crystals, oriented samples or magnetic resonance imaging in rotating solids.

In solid-state NMR of polycrystalline solids, one can similarly show that the signal will depend on the powder average euler angle γ according to

$$S(t, \Theta, \phi_0) = e^{iW_0t} \sum_{N_1, N_2} A_{N_1} A_{N_2}^* e^{-iN_1\Theta} e^{i(N_2-N_1)(\phi_0+\gamma)},$$

and an integral over this angle removes the dependance on the initial rotor phase, giving the condition $N_1 = N_2$, and so the signal further simplifies to

$$S(t, \Theta) = e^{iW_0t} \sum_N A_N A_N^* e^{-iN\Theta}. \quad (\text{A.2.4})$$

A.3 Derivations

A.3.1 Time Domain Signal

From the signal phase we calculate the signal

$$S(t, \phi_0) = e^{iW_0t} \exp \left\{ i \sum_{m \neq 0} W_m e^{im(\Omega_R t + \phi_0)} \right\} \exp \left\{ -i \sum_{m \neq 0} W_m e^{im\phi_0} \right\}.$$

Using the property of delta functions this can be rewritten

$$\begin{aligned} S(t, \phi_0) &= e^{iW_0t} \\ &\times \frac{1}{2\pi} \int_0^{2\pi} d\Theta_1 \delta(\Theta_1 - \Omega_R t - \phi_0) \exp \left\{ i \sum_{m \neq 0} W_m e^{im\Theta_1} \right\} \\ &\times \frac{1}{2\pi} \int_0^{2\pi} d\Theta_2 \delta(\Theta_2 - \phi_0) \exp \left\{ -i \sum_{m \neq 0} W_m e^{im\Theta_2} \right\}. \end{aligned}$$

The delta functions can then be expanded as sums

$$\begin{aligned} S(t, \phi_0) &= e^{iW_0t} \\ &\times \sum_{N_1} \frac{1}{2\pi} \int_0^{2\pi} d\Theta_1 \exp \{ iN_1(\Theta_1 - \Omega_R t - \phi_0) \} \exp \left\{ i \sum_{m \neq 0} W_m e^{im\Theta_1} \right\} \\ &\times \sum_{N_2} \frac{1}{2\pi} \int_0^{2\pi} d\Theta_2 \exp \{ iN_2(\Theta_2 - \phi_0) \} \exp \left\{ -i \sum_{m \neq 0} W_m e^{im\Theta_2} \right\}, \end{aligned}$$

and after regrouping the signal becomes

$$\begin{aligned}
S(t, \phi_0) &= e^{iW_0 t} \\
&\times \sum_{N_1} \left[\frac{1}{2\pi} \int_0^{2\pi} d\Theta_1 \exp \left\{ iN_1\Theta_1 + i \sum_{m \neq 0} W_m e^{im\Theta_1} \right\} \right] \exp \{-iN_1(\Omega_R t + \phi_0)\} \\
&\times \sum_{N_2} \left[\frac{1}{2\pi} \int_0^{2\pi} d\Theta_2 \exp \left\{ iN_2\Theta_2 - i \sum_{m \neq 0} W_m e^{im\Theta_2} \right\} \right] \exp \{-iN_2\phi_0\}.
\end{aligned}$$

Now we reverse the summation over N_2 , (i.e. $N_2 \rightarrow -N_2$) and obtain

$$\begin{aligned}
S(t, \phi_0) &= e^{iW_0 t} \\
&\times \sum_{N_1} \left[\frac{1}{2\pi} \int_0^{2\pi} d\Theta_1 \exp \left\{ iN_1\Theta_1 + i \sum_{m \neq 0} W_m e^{im\Theta_1} \right\} \right] \exp \{-iN_1(\Omega_R t + \phi_0)\} \\
&\times \sum_{N_2} \left[\frac{1}{2\pi} \int_0^{2\pi} d\Theta_2 \exp \left\{ -iN_2\Theta_2 + i \sum_{m \neq 0} W_m e^{im\Theta_2} \right\} \right] \exp \{iN_2\phi_0\}.
\end{aligned}$$

If we define

$$A(N) = \frac{1}{2\pi} \int_0^{2\pi} \exp \left\{ i \sum_{m \neq 0} W_m e^{im\Theta} \right\} e^{iN\Theta} d\Theta, \quad (\text{A.3.1})$$

then we write the signal as

$$S(t, \phi_0) = e^{iW_0 t} \sum_{N_1, N_2} A(N_1) A^*(N_2) e^{-iN_1 \Omega_R t} e^{i(N_2 - N_1) \phi_0}. \quad (\text{A.3.2})$$

A.3.2 Sideband Amplitudes in Polycrystalline Samples

$$\Omega(t, \gamma) = W_0(\alpha, \beta) + \sum_{l=1}^{\infty} \sum_{m \neq 0} \omega_{l,m}(\alpha, \beta) e^{im(\Omega_R t + \gamma)},$$

where Ω_R is the rotor speed. The signal is

$$S(t, \gamma) = e^{iW_0 t} \exp \left[i \sum_{m \neq 0} W_m e^{im\gamma} \{ e^{im\Omega_R t} - 1 \} \right]$$

where $W_m = \sum_{l=1}^{\infty} \frac{\omega_{l,m}(\alpha, \beta)}{im\Omega_R}$. Dropping the time independent frequency component and substituting $\Theta = \Omega_R t$ we obtain the sideband signal as a function of rotor pitch

$$A(\Theta, \gamma) = \exp \left[i \sum_{m \neq 0} W_m e^{im\gamma} \{ e^{im\Theta} - 1 \} \right].$$

Substituting this expression into the Fourier relationship between rotor pitch and sideband order,

$$A(N, \gamma) = \frac{1}{2\pi} \int_0^{2\pi} d\Theta e^{-iN\Theta} A(\Theta, \gamma). \quad (\text{A.3.3})$$

As shown by Levitt, the sideband intensities as a function of γ are related according to

$$A(N, \gamma) = \sum_{N_1, N_2} A(N_1, 0) A^*(N_2, 0) e^{-iN_1 \Omega_R t} e^{i(N_2 - N_1) \gamma}, \quad (\text{A.3.4})$$

and integrating both sides over γ yields

$$\langle A(N) \rangle_\gamma = |A(N, 0)|^2 \quad (\text{A.3.5})$$

Thus, the numerical calculation of the polycrystalline spectrum only needs to average over the angles α and β .

We can use the identity

$$W_m + W_{-m} = 2X_m$$

and

$$W_m e^{im\theta} + W_{-m} e^{-im\theta} = 2X_m \cos m\theta - 2Y_m \sin m\theta,$$

to obtain

$$A(\Theta, 0) = \exp \left[i \sum_{m>0} \{ 2X_m (\cos m\Theta - 1) - 2Y_m \sin m\Theta \} \right].$$

To avoid aliasing of signals in the sideband order dimension the $\Delta\Theta$ increment must be smaller than π/N_{\max} , where N_{\max} is the highest order sideband present in the sideband pattern. We may additionally be required to choose $\Delta\Theta$ and $2\pi/\Delta\Theta$ to be compatible with the radix of the Fourier transform algorithm.

A.4 Phase Adjusted Spinning Sideband Experiment (PASS)

After a single pulse, the phase of the MAS signal has the form

$$\Phi = W_0 t - \sum_{l,m \neq 0} iW_{l,m} e^{im\phi_0} [e^{im\Omega_R t} - 1]. \quad (\text{A.4.1})$$

In a multipulse experiment the phase of the MAS signal can be manipulated into one of several desirable forms. These forms include PASS, IRS, and TOSS, as well as other possibilities. One approach for manipulating the phase, first demonstrated by Dixon, is to use a series of π pulses placed at times τ_j after the excitation pulse. The signal phase at τ_{n+1} after the n th π pulse is

$$\begin{aligned} \Phi_n &= (-1)^n \sum_{j=0}^n (-1)^j \int_{\tau_j}^{\tau_{j+1}} \Omega(s) ds. \\ &= W_0 \left[\sum_{j=0}^n (-1)^{j+n} (\tau_{j+1} - \tau_j) \right] \\ &\quad - \sum_{l,m \neq 0} iW_{l,m} e^{im\phi_0} \left[- \sum_{j=0}^n (-1)^{j+n} [e^{im\theta_{j+1}} - e^{im\theta_j}] \right], \end{aligned} \quad (\text{A.4.2})$$

where $\tau_0 = 0$ and $\theta_j = \Omega_R \tau_j$. This expression can be rearranged to

$$\begin{aligned} \Phi_n &= W_0 \left[\tau_{n+1} - 2(-1)^n \sum_{j=1}^n (-1)^j \tau_j \right] \\ &\quad - \sum_{l,m \neq 0} iW_{l,m} e^{im\phi_0} \left[1 - (-1)^n e^{im\theta_{n+1}} + 2(-1)^n \sum_{j=1}^n (-1)^j e^{im\theta_j} \right], \end{aligned} \quad (\text{A.4.3})$$

In PASS the signal phase is manipulated to have the form

$$\Phi_{PASS} = - \sum_{l,m \neq 0} iW_{l,m} e^{im\phi_0} [e^{im(\Omega_R t + \Theta_0)} - 1], \quad (\text{A.4.4})$$

where Θ_0 can be varied independent of t . Such a phase leads to the signal

$$S_{PASS}(t, \phi_0) = \sum_{N_1, N_2} A_{N_1} A_{N_2}^* e^{-iN_1(\Omega_R t + \Theta_0)} e^{i(N_2 - N_1)\phi_0}. \quad (\text{A.4.5})$$

Equating Eq. (A.4.3) and (A.4.4), we obtain

$$t = \tau_{n+1} - 2(-1)^n \sum_{j=1}^n (-1)^j \tau_j = 0 \quad (\text{A.4.6})$$

$$\left[e^{im(\theta_t + \Theta_0)} - 1 \right] = 1 - (-1)^n e^{im\theta_{n+1}} + 2(-1)^n \sum_{j=1}^n (-1)^j e^{im\theta_j} \quad (\text{A.4.7})$$

where $\theta_t = \Omega_R t$. Further substitution yields the first equation

$$\theta_t = \theta_{n+1} - 2(-1)^n \sum_{j=1}^n (-1)^j \theta_j = 0, \quad (\text{A.4.8})$$

and finally we obtain the remaining equations

$$e^{im\Theta_0} = 2 - (-1)^n e^{im\theta_{n+1}} + 2(-1)^n \sum_{j=1}^n (-1)^j e^{im\theta_j} \quad (\text{A.4.9})$$

From this set of simultaneous equations we can solve for the necessary π pulse spacings, τ_j , for the PASS solutions. Make a table of Θ_0 values from 0 to 2π and for each Θ_0 solve for the θ_j values.

To obtain the five π pulse-2D-PASS sequence of Levitt and coworkers, we set $n = 5$ and $\theta_6 = 2\pi$, and simplify our expressions to

$$e^{im\Theta_0} + 1 + 2 \sum_{j=1}^5 (-1)^j e^{im\theta_j} = 0 \quad (\text{A.4.10})$$

$$2\pi + 2 \sum_{j=1}^5 (-1)^j \theta_j = 0, \quad (\text{A.4.11})$$

solve for the remaining τ_j .

BIBLIOGRAPHY

- [1] S. Antonijevic and S. Wimperis. Separation of quadrupolar and chemical/paramagnetic shift interactions in two-dimensional 2h ($I = 1$ nuclear magnetic resonance spectroscopy. *Journal of Chemical Physics*, 122:297–304, 2006.
- [2] F. H. Larsen, H. J. Jakobsen, P. D. Ellis, and N. C. Nielsen. Sensitivity-enhanced quadrupolar-echo NMR of half-integer quadrupolar nuclei. magnitudes and relative orientation of chemical shielding and quadrupolar coupling tensors. *J. Phys. Chem. A*, 101:8597–8606, 1997.
- [3] D. Massiot, J. Hiet, N. Pellerin, F. Fayon, M. Deschamps, S. Steuernagel, and P. J. Grandinetti. Two dimensional one pulse mas of half-integer quadrupolar nuclei. *J. Magn. Reson.*, 181:310–315, 2006.
- [4] O. N. Antzutkin, S. C. Shekar, and M. H. Levitt. Two-dimensional sideband separation in magic-angle spinning NMR. *J. Magn. Reson. A*, 115:7–19, 1995.
- [5] G. A. Williams and H. S. Gutowsky. Sample spinning and field modulation effects in nuclear magnetic resonance. *Phys. Rev.*, 104:278, 1956.
- [6] E. R. Andrew, A. Bradbury, and R. G. Eades. Removal of dipolar broadening of nuclear magnetic resonance spectra of solids by specimen rotation. *Nature*, 183:1802–1803, 1958.
- [7] I. J. Lowe. Free induction decays of rotating solids. *Phys. Rev. Lett.*, 2:285–287, 1959.
- [8] A. Pines, M. G. Gibby, and J. S. Waugh. Proton-enhanced nuclear induction spectroscopy. ^{13}C chemical shielding anisotropy in some organic solids. *Chem. Phys. Lett.*, 15:373, 1972.
- [9] E. O. Stejskal, J. Schaefer, and J. S. Waugh. Magic-angle spinning and polarization transfer in proton-enhanced NMR. *J. Magn. Reson.*, 28:105–112, 1977.
- [10] M. Mehring. *High Resolution NMR Spectroscopy in Solids*, volume 11. Springer-Verlag, Berlin, 1983.

- [11] A. Abragam. *Principles of Nuclear Magnetism*. Oxford University Press, Walton Street, Oxford OX2 6DP, 1961.
- [12] R. R. Ernst, G. Bodenhausen, and A. Wokaun. *Principles of Nuclear Magnetic Resonance in One and Two Dimensions*. Oxford, Walton Street, Oxford OX2 6DP, 1987.
- [13] E. O. Stejskal and J. D. Memory. *High Resolution NMR in the Solid State*. Oxford University Press, New York, 1994.
- [14] R. K. Harris, E. D. Becker, S. M. Cabral De Menezes, Pierre Grangerd, R. E. Hoffman, and K. W. Zilm. Further conventions for NMR shielding and chemical shifts, IUPAC recommendations 2008. *Inorg. Chem.*, 3:41–56, 2008.
- [15] R. L. Cook and F. C. Delucia. Application of the theory of irreducible tensor operators to molecular hyperfine structure. *Am. J. Phys.*, 39:1433–1454, 1971.
- [16] E. M. Landau and J. P. Rosenbusch. Lipid cubic phases: A novel concept for the crystallization of membrane proteins. *Proc. Natl. Acad. Sci., USA*, 93:14532–14535, 1996.
- [17] M. Caffrey. Membrane protein crystallization. *J. Struct. Biol.*, 142(1):108–132, 2003.
- [18] J. Clogston, G. Craciun, D. J. Hart, and M. Caffrey. Controlling release from the lipidic cubic phase by selective alkylation. *J. Cont. Rel.*, 102(2):441–461, 2005.
- [19] J. Clogston and M. Caffrey. Controlling release from the lipidic cubic phase. amino acids, peptides, proteins and nucleic acids. *J. Cont. Rel.*, 107:97–111, 2005.
- [20] J. S. Patton and M. C. Carey. Watching fat digestion. *Science*, 204:145–148, 1979.
- [21] D. M. Anderson, S. M. Gruner, and S. Leibler. Geometrical aspects of the frustration in the cubic phases of lyotropic liquid crystals. *Proc. Natl. Acad. Sci., USA*, 85:5364–5368, 1988.
- [22] S. Hyde, S. Andersson, K. Larsson, Z. Blum, T. Landh, S. Lidin, and B.W. Ninham. *The Language of Shape*. Elsevier Science, 1996.
- [23] A. Samoson, B. Q. Sun, and A. Pines. New angles in motional averaging. In *Pulsed Magnetic Resonance: NMR, ESR, and Optics - A reconognition of E. L. Hahn*. Clarendon Press, Oxford, 1992.

- [24] G. Lindblom and L. Rilfors. Cubic phases and isotropic structures formed by membrane lipids-possible biological relevance. *Biochim. Biophys. Acta*, 988:221–256, 1989.
- [25] P. R. Cullis and B. de Kruijff. Polymorphic phase behaviour of lipid mixtures as directed by ^{31}P NMR. *Biochimica et Biophysica Acta*, 507:207–218, 1978.
- [26] P. R. Cullis and M. J. Hope. Effects of fusogenic agents on membrane structure of erythrocyte ghosts and the mechanism of membrane fusion. *Nature*, 271:672–674, 1978.
- [27] A. Pampel, E. Strandberg, G. Lindblom, and F. Volke. High-resolution NMR on cubic lyotropic liquid crystalline phases. *Chem. Phys. Lett.*, 287:468–474, 1998.
- [28] C. Glaubitz and A. Watts. Magic angle-oriented sample spinning (maoss): A new approach toward biomembrane studies. *J. Magn. Reson.*, 130:305–316, 1998.
- [29] A. Pampel, K. Zick, H. Glauner, and F. Engelke. Studying lateral diffusion in lipid bilayers by combining a magic angle spinning NMR probe with a microimaging gradient system. *J. Am. Chem. Soc.*, 126:9534–9535, 2004.
- [30] A. Pampel, D. Michel, and R. Reszka. Pulsed field gradient MAS-NMR studies of the mobility of carboplatin in cubic liquid-crystalline phases. *Chem. Phys. Lett.*, 357:131–136, 2002.
- [31] A. Cheng, B. Hummel, H. Qui, and M. Caffrey. A simple mechanical mixer for small viscous lipid-containing samples. *Chem. Phys. Lett.*, 95:11–21, 1998.
- [32] H. Qiu and M. Caffrey. The phase diagram of the monoolein/water system: metastability and equilibrium aspects. *Biomaterials*, 21:223–234, 2000.
- [33] M. Piotto, V. Saudek, and V. Sklenar. Gradient-tailored excitation for single-quantum nmr spectroscopy of aqueous solutions. *J. Biomol. NMR*, 2(6):661–665, 1992.
- [34] T.-L. Hwang and A. J. Shaka. Water suppression that works. excitation sculpting using arbitrary waveforms and pulsed field gradients. *J. Magn. Reson. A*, 112:275–279, 1995.
- [35] D. Neuhaus and M. P. Williamson. *The Nuclear Overhauser Effect in Structural and Conformational Analysis*. New York, Weinheim, 1989.
- [36] K. Wüthrich. *NMR of Proteins and Nucleic Acids*. Wiley, 1986.

- [37] H. Ljusberg-Wahren, M. Herslöf, and K. Larsson. A comparison of the phase behaviour of the monoolein isomers in excess water. *Chem. Phys. Lipids*, 33:211–214, 1983.
- [38] T.-L. Hwang and A. J. Shaka. Cross relaxation with TOCSY: Transverse rotating-frame overhauser effect spectroscopy. *J. Am. Chem. Soc.*, 114:3157–3159, 1992.
- [39] J. A. Hamilton and D. M. Small. Solubilization and localization of triolein in phosphatidylcholine bilayers: A ^{13}C NMR study. *Proc. Natl. Acad. Sci., USA*, 78(11):6878–6882, 1981.
- [40] U. R. K. Rao, C. Manohar, B. S. Valaulikar, and R. M. Iyer. Micellar chain model for the origin of the viscoelasticity in dilute surfactant solutions. *J. Phys. Chem.*, 91(12):3286 – 3291, 1987.
- [41] A. Carrington and A. D. McLachlan. *Introduction to Magnetic Resonance*. Chapman and Hall, Methuen, Inc., 1967.
- [42] J. Kim, W. Lu, W. Qiu, L. Wang, M. Caffrey, and D. Zhong. Ultrafast hydration dynamics in the lipidic cubic phase: Discrete water structures in nanochannels. *J. Phys. Chem. B.*, 110:21994–22000, 2006.
- [43] W. Liu and M. Caffrey. Interactions of tryptophan, tryptophan peptides and tryptophan alkyl esters at curved membrane interfaces. *Biochemistry*, 45:11713–11726, 2006.
- [44] S. Persson, J. A. Killian, and G. Lindblom. Molecular ordering of interfacially localized tryptophan analogs in ester- and ether-lipid bilayers studied by H-2-NMR. *Biophys. J.*, 75(3):1365–1371, 1998.
- [45] W.-M. Yau, W. C. Wimley, K. Gawrisch, and S. H. White. The preference of tryptophan for membrane interfaces. *Biochemistry*, 37(42):14713–14718, 1998.
- [46] R. R. Ketchum, W. Hu, and T. A. Cross. High-resolution conformation of gramicidin a in a lipid bilayer by solid-state NMR. *Science*, 261:1457–1460, 1993.
- [47] S. J. Opella and F. M. Marassi. Structure determination of membrane proteins by NMR spectroscopy. *Chem. Rev.*, 104:3587–3606, 2004.
- [48] F. Caboi, J. Borne, T. Nylander, A. Khan, A. Svendsen, and S. Patkar. Lipase action on a monoolein/sodium oleate aqueous cubic liquid crystalline phase - a NMR and X-ray diffraction study. *Coll. Sur. B-Biointerfaces*, 26(1-2):159–171, 2002.
- [49] E. Oldfield, J. L. Bowers, and J. Forbes. High-resolution proton and carbon-13 NMR of membranes: Why sonicate? *Biochemistry*, 26:6919–6923, 1987.

- [50] E. G. Finer, A. G. Flook, and H. Hauser. The nature and origin of the NMR spectrum of unsonicated and sonicated aqueous egg yolk lecithin dispersions. *Biochim. Biophys. Acta*, 260(1):59–69, 1972.
- [51] R. R. Vold, R. S. Prosser, and A. J. Deese. Isotropic solutions of phospholipid bicelles: A new membrane mimetic for high-resolution NMR studies of polypeptides. *J. Biomol. NMR*, 9:329–335, 1997.
- [52] H. Y. Carr and E. M. Purcell. Effects of diffusion on free precession in nuclear magnetic resonance experiments. *Phys. Rev.*, 94:630–638, 1954.
- [53] S. Meiboom and D. Gill. Modified spin-echo method for measuring nuclear relaxation times. *Rev.Sci.Instrum*, 29:688, 1958.
- [54] E. L. Hahn. Spin echoes. *Physical Review*, 80(4):580–594, Nov 1950.
- [55] F. H. Larsen, H. J. Jakobsen, P. D. Ellis, and N. C. Nielsen. QCPMG-MAS of half-integer quadrupolar nuclei. *J.Magn. Reson.*, 131:144–147, 1998.
- [56] F. H. Larsen, J. Skibsted, H. J. Jakobsen, and N. C. Nielsen. Solid-state QCPMG NMR of low- γ quadrupolar metal nuclei in natural abundance. *J. Am. Chem. Soc.*, 122:7080–7086, 2000.
- [57] R. Lefort, J. W. Wiench, and M. Pruski ad J. P. Amoureux. Optimization of data acquisition and processing in carr-purcell-meiboom-gill multiple quantum magic angle spinning nuclear magnetic resonance. *J.Chem.Phys*, 116:2493–2501, 2002.
- [58] P. Hodgkinson and L. Emsley. The reliability of the determination of tensor parameters by solid-state nuclear magnetic resonance. *J. Chem. Phys*, 107:4808–4816, 1997.
- [59] P. Blumler, B. Blümich, and J. Jansen. Two-dimensional one-pulse rotational echo spectra. *Solid State NMR*, 3:237–240, 1994.
- [60] B. Blümich, P. Blumler, and J. Jansen. Presentation of sideband envelopes by two-dimensional one-pulse (TOP) spectroscopy. *Solid State NMR*, 1:111–113, 1992.
- [61] D. Freude and J. Haase. Quadrupole effects in solid-state nuclear magnetic resonance. *NMR Basic Principle and Progress*, 21:1–90, 1993.
- [62] R. R. Ernst, G. Bodenhausen, and A. Wokaun. *Principles of Nuclear Magnetic Resonance in One and Two Dimensions*. Oxford, Walton Street, Oxford OX2 6DP, 1987.

- [63] G. Neue, C. Dybowski, M. L. Smith, M. A. Hepp, and D. L. Perry. Determination of Pb^{2+} chemical shift tensors from precise powder line shape analysis. *Solid State NMR*, 6:241–250, 1996.
- [64] O. Dmitrenko, S. Bai, P. A. Beckmann, S. V. Bramer, A. J. Vega, and C. Dybowski. The relationship between ^{207}Pb NMR chemical shift and solid-state structure in Pb(II) . *J. Phys. Chem. A*, 112:3046–3052, 2008.
- [65] J. Skibsted and H. J. Jakobsen. Variable-temperature ^{87}Rb magic angle spinning NMR spectroscopy of inorganic rubidium salts. *J. Phys. Chem. A*, 103:7958–7971, 1999.
- [66] T. Vosegaard, J. Skibsted, H. Bildsoe, and H. J. Jacobsen. Combined effect of second-order quadrupole coupling and chemical shielding anisotropy on the central transition in MAS NMR of quadrupolar nuclei ^{87}Rb MAS NMR of RbClO_4 . *J. Phys. Chem.*, 99:10731–10735, 1995.
- [67] T. Vosegaard, J. Skibsted, H. Bildsoe, and H. J. Jacobsen. Quadrupole coupling and anisotropic shielding from single-crystal NMR of the central transition for quadrupolar nuclei. ^{87}Rb NMR of RbClO_4 and Rb_2SO_4 . *J. Magn. Reson. A*, 122:111–119, 1996.
- [68] J. T. Ash, N. T. Trease, and P. J. Grandinetti. Separating chemical shift and quadrupolar anisotropies via multiple-quantum nmr spectroscopy. *J. Am. Chem. Soc.*, 33:10858–10859, 2008.
- [69] J. M. Koons, E. Hughes, H. M. Cho, and P. D. Ellis. Extracting multitensor solid-state NMR parameter from lineshapes*. *J. Magn. Reson. A*, 114:12–23, 1995.
- [70] J. Herzfeld and A. E. Berger. Sideband intensities in NMR spectra of samples spinning at the magic angle. *J. Chem. Phys.*, 73:6021, 1980.
- [71] A. Bax, N. M. Szeverenyi, and G. E. Maciel. Correlation of isotropic shifts and chemical shift anisotropies by two-dimensional Fourier-transform magic-angle hopping NMR spectroscopy. *J. Magn. Reson.*, 52:147, 1983.
- [72] P. J. Grandinetti, J. H. Baltisberger, A. Llor, Y. K. Lee, U. Werner, M. A. Eastman, and A. Pines. Pure absorption-mode lineshapes and sensitivity in two-dimensional dynamic angle spinning NMR. *J. Magn. Reson. A*, 103:72–81, 1993.
- [73] J. Z. Hu, D. W. Alderman, C. H. Ye, R. J. Pugmire, and D. M. Grant. An isotropic chemical shift-chemical shift anisotropy magic-angle slow-spinning 2D NMR experiment. *J. Magn. Reson. A*, 105(1):82–87, 1993.

- [74] Z. H. Gan. High-resolution chemical-shift and chemical-shift anisotropy correlation in solids using slow magic-angle spinning. *J. Am. Chem. Soc.*, 114(21):8307–8309, 1992.
- [75] W. T. Dixon. Spinning-sideband-free and spinning-sideband-only NMR spectra in spinning samples. *J. Chem. Phys.*, 77:1800, 1982.
- [76] J. K. Hennig. Multi echo acquisition techniques using inverting radio frequency phase in MRI. *Methods in biomedical magnetic resonance imaging and spectroscopy*, Wiley, London:256–264, 2000.
- [77] F. H. Larsen, H. J. Jacobsen, P. D. Ellis, and N. C. Nielsen. Molecular dynamics from ^2H quadrupolar Carr-Purcell-Meiboom-Gill solid-state NMR spectroscopy. *Chemical Physics letter*, 292:467–473, 1998.
- [78] F. H. Larsen, H. J. Jacobsen, P. D. Ellis, and N. C. Nielsen. Sensitivity enhanced quadrupolar-echo NMR of half-integer quadrupolar nuclei. magnitude and relative orientation of chemical shielding and quadrupolar coupling tensors. *J. Phys. Chem. A*, 101:8597–8606, 1997.
- [79] R. Siegel, T. T. Nakashima, and R. E. Wasylshen. Application of multiple-pulse experiments to characterize broad nmr chemical-shift powder patterns from spin-1/2 nuclei in the solid state. *J. Phys. Chem. B*, 108:2218–2226, 2004.
- [80] J. W. Wiench, V. S. Y. Lin, and M. Pruski. ^{29}Si NMR in solid state with CPMG acquisition under MAS. *J. Mag. Res.*, 193:233–242, 2008.
- [81] I. Hung, A. J. Rossini, and R. W. Schurko. Application of carr-purcell-meiboom-gill pulse sequence for the acquisition of solid-state NMR spectra of spin-1/2 nuclei. *J. Phys. Chem. A*, 108:7112–7120, 2004.
- [82] F. H. Larsen and I. Farnan. ^{29}Si and ^{17}O (Q)CPMG-MAS solid-state NMR experiments as an optimum approach for half-integer nuclei having long t_1 relaxation times. *Chem. Phys. Lett.*, 357:403–408, 2002.
- [83] J. Z. Hu and R. A. Wind. Sensitivity-enhanced phase-corrected ultra-slow magic angle turning using multiple-echo data acquisition. *Journal of Magnetic Resonance*, 163:149–162, 2003.
- [84] D. Sakellariou, J.-F. Jacquinet, and T. Charpentier. 2D correlation spectra of isotropic and anisotropic ^{29}Si chemical shifts in crystalline and amorphous natural abundance materials under very slow sample rotation. *Chem. Phys. Lett.*, 411:171–174, 2005.
- [85] I. Hung and Z. Gan. On the magic-angle-turning and phase-adjusted spinning sidebands experiments. *Journal of Magnetic Resonance*, 204:150–154, 2010.

- [86] K. A. Smith, R. J. Kirkpatrick, E. Oldfield, and D. M. Henderson. High-resolution Si-29 nuclear-magnetic-resonance spectroscopic study of rock-forming silicates. *Chemical Physics letter*, 68:1206–1215, 1983.
- [87] J. F. Stebbins. Identification of multiple structural species in silicate glasses by ^{29}Si NMR. *Nature*, 330:465, 1987.
- [88] M. S. Ironside, R. S. Stein, and M. J. Duer. Using chemical shift anisotropy to resolve isotropic signals in solid-state NMR. *Journal of Magnetic Resonance*, 188:49–55, 2007.
- [89] M. S. Ironside, D. G. Reid, and M. J. Duer. Correlating sideband patterns with powder patterns for accurate determination of chemical shift parameters in solid-state NMR. *Magnetic Resonance in Chemistry*, 46:913–917, 2008.
- [90] F. G. Vogt, J. M. Gibson, D. J. Aurentz, K. T. Mueller, and A. J. Benesi. Multiple-rotor-cycle 2D PASS experiments with applications to ^{207}Pb spectroscopy. *Journal of Magnetic Resonance*, 143:153–160, 2000.
- [91] F. Song, O. N. Antzutkin, A. Rupprecht, and M. H. Levitt. Order-resolved sideband separation in magic-angle-spinning nmr. ^{31}P NMR of oriented DNA fibers. *Chemical Physics Letters*, 253:349–354, 1996.
- [92] Y. Wei, D. Lee, and A. Ramamoorthy. Solid-state ^{13}C NMR chemical shift anisotropy tensors of polypeptides. *Journal of the American Chemical Society*, 123:6118–6126, 2001.
- [93] F. Fayon, C. Bessada, A. Douy, and D. Massiot. Chemical bonding of lead in glasses through isotropic vs anisotropic correlation: Pass shifted echo. *J. Magn. Reson.*, 137:116–121, 1999.
- [94] B. Cherry, J. W. Zwanziger, and B. G. Aitken. The structure of $\text{GeS}_2\text{-P}_2\text{S}_5$ glasses. *Journal of Physical Chemistry B*, 106:11093–11101, 2002.
- [95] M.C. Davis, D. Kaseman, S. Parvani, K. Sanders, P.J. Grandinetti, P. Florian, and D. Massiot. $\text{Q}^{(n)}$ -species distribution in $\text{K}_2\text{O 2SiO}_2$ by ^{29}Si Magic Angle Flipping NMR. *J. Phys. Chem. A*, 114(17):5503–5508, 2010.
- [96] N. Ivchenko, C. E. Hughes, and M. H. Levitt. Application of cogwheel phase cycling to sideband manipulation experiments in solid-state nmr. *Journal of Magnetic Resonance*, 164:286–293, 2003.
- [97] K.K. Dey, J. Ash, N. Trease, and P.J. Grandinetti. Trading sensitivity for information: CPMG acquisition in solids. *J. Chem. Phys.*, Submitted, 2010.

- [98] M. Goswami, P. K. Madhu, J. Dittmer, N. C. Nielsen, and S. Ganapathy. Sensitivity enhancement of ^{29}Si double-quantum dipole recoupling spectroscopy by Carr-Purcell-Meiboom-Gill acquisition method. *Chemical Physics Letter*, 478:287–291, 2009.
- [99] G. Bodenhausen, H. Kogler, and R. R. Ernst. Selection of coherence-transfer pathways in NMR pulse experiments. *J. Magn. Reson.*, 58:370–388, 1984.
- [100] A. D. Bain. Coherence levels and coherence pathways in NMR. a simple way to design phase cycling procedures. *J. Magn. Reson.*, 56:418–427, 1984.
- [101] M. H. Levitt, P. K. Madhu, and C. E. Hughes. Cogwheel phase cycling. *Journal of Magnetic Resonance*, 155:300–306, 2002.
- [102] A. Navrotsky. Energetics of silicate melts. In J. F. Stebbins, P. F. McMillan, and D. B. Dingwell, editors, *Structure , Dynamics and Properties of Silicate Melts*, volume 32 of *Reviews in Mineralogy*, pages 121–143. Mineralogical Society of America, Washington, DC, 1995.
- [103] P. C. Hess. Thermodynamic mixing properties and the structure of silicate melts. In J. F. Stebbins, P. F. McMillan, and D. B. Dingwell, editors, *Structure , Dynamics and Properties of Silicate Melts*, volume 32 of *Reviews in Mineralogy*, pages 145–190. Mineralogical Society of America, Washington, DC, 1995.
- [104] E. D. Lacy. A statistical model of polymerisation/depolymerisation relationship in silicate melts and glasses. *Phys. Chem. Glasses*, 6(5):171–180, 1965.
- [105] B. Vessal, A. C. Wright, and A. C. Hannon. Alkali silicate glasses: Interpreting neutron diffraction results using the molecular dynamics simulation technique. *J. Non Cryst. Solids*, 196:233–238, 1996.
- [106] P. Zhang, C. Dunlap, P. Florian, P. J. Grandinetti, I. Farnan, and J. F. Stebbins. Silicon site distributions in an alkali silicate glass derived by two-dimensional ^{29}Si nuclear magnetic resonance. *J. Non. Cryst. Solids*, 204:294–300, 1996.
- [107] W. Malfait, W. Halter, and R. Verel. Si-29 NMR spectroscopy of silica glass: T-1 relaxation and constraints on the Si-O-Si bond angle distribution. *Chem. Geol.*, 256:269–277, 2008.
- [108] A.-R. Grimmer, E. F. Gechner, and G. Molgedey. High resolution ^{29}Si NMR in solid silicates. correlations between shielding tensor and Si-O bond length. *Chem. Phys. Lett.*, 77:331–335, 1981.
- [109] V. P. Zakaznova-Herzog, W. J. Malfait, F. Herzog, and W. E. Halter. Quantitative Raman spectroscopy: Principles and application to potassium silicate glasses. *Journal of Non-Crystalline Solids*, 353:4015–4028, 2007.

- [110] P. Zhang, P. J. Grandinetti, and J. F. Stebbins. Anionic species determination in CaSiO_3 glass using two-dimensional ^{29}Si NMR. *J. Phys. Chem. B*, 101(20):4004–4008, 1997.
- [111] M. Baks, J. T. Rasmussen, and N. Chr. Nielsen. SIMPSON: A general simulation program for solid-state NMR spectroscopy. *J. Magn. Reson.*, 147:296–330, 2000.
- [112] C. Muller, W. Schajor, H. Zimmerman, and U. Haeberien. *J. Magn. Reson.*, 56:235, 1984.
- [113] B. Blumich and H. W. Spiess. *Angew. Chem., Int. Ed. Engl.*, 27:1655, 1988.
- [114] H. W. Spiess. *Chem. Rev.*, 91:1321, 1991.
- [115] S. Vega, W. Shattuck, and A. Pines. Fourier-transform double-quantum NMR in solids. *Physical Review Letters*, 37:43–46, 1976.
- [116] L. Muller. Double-quantum deuterium echoes in magic-angle spinning polycrystalline solids. *Journal of Magnetic Resonance*, 42:324–329, 1981.
- [117] N. Chandrakumar, G. von Fircks, and H. Gunther. The 2D QUADSHIFT experiment: separation of deuterium chemical shifts and quadrupolar couplings by two-dimensional solid-state MAS NMR spectroscopy. *Magnetic Resonance in Chemistry*, 32:433–435, 1994.
- [118] J. H. Kristensen, H. Bildsoe, H. J. Jakobsen, and N. C. Nielsen. Separation of 2h MAS NMR spectra by two-dimensional spectroscopy. *Journal of Magnetic Resonance*, 139:314–333, 1999.
- [119] T. P. Spaniol, A. Kubo, and T. Terao. Two-dimensional deuterium magic-angle-spinning nuclear magnetic resonance of paramagnetic compounds: separation of paramagnetic and quadrupole interactions. *Journal of Chemical Physics*, 106:5393–5405, 1997.
- [120] S. Antonijevic and G. Bodenhausen. Quadrupolar transfer pathways. *Journal of Magnetic Resonance*, 180:297–304, 2006.